



A Fourth Planet in the Kepler-51 System Revealed by Transit Timing Variations

Kento Masuda^{1,†}, Jessica E. Libby-Roberts^{2,3,†}, John H. Livingston^{4,5,6}, Kevin B. Stevenson⁷, Peter Gao⁸, Shreyas Vissapragada⁹, Guangwei Fu¹⁰, Te Han¹¹, Michael Grekkek-McKeon¹², Suvrath Mahadevan^{3,2}, Eric Agol¹³, Aaron Bello-Arufe¹⁴, Zachory Berta-Thompson¹⁵, Caleb I. Cañas^{16,52}, Yayaati Chachan^{17,18,52}, Leslie Hebb^{19,20}, Renyu Hu^{12,14}, Yui Kawashima^{21,22,23}, Heather A. Knutson²⁵, Caroline V. Morley²⁴, Catriona A. Murray¹⁵, Kazumasa Ohno²⁵, Armen Tokadjian¹⁴, Xi Zhang²⁶, Luis Welbanks²⁷, Matthew C. Nixon²⁸, Richard Freedman²⁹, Norio Narita^{4,30,31}, Akihiko Fukui^{30,31}, Jerome P. de Leon³², Mayuko Mori³³, Enric Palle³⁴, Felipe Murgas^{34,35}, Hannu Parviainen^{34,35}, Emma Esparza-Borges^{34,35}, Daniel Jontof-Hutter³⁶, Karen A. Collins³⁷, Paul Benni³⁸, Khalid Barkaoui^{34,39,40}, Francisco J. Pozuelos⁴¹, Michaël Gillon³⁹, Emmanuël Jehin⁴², Zouhair Benkhaldoun⁴³, Suzanne Hawley⁴⁴, Andrea S. J. Lin^{3,2}, Guðmundur Stefánsson⁴⁵, Allyson Bieryla³⁷, Mesut Yilmaz^{46,47}, Hakan Volkan Senavci^{46,47}, Eric Girardin⁴⁸, Giuseppe Marino⁴⁹, and Gavin Wang⁵⁰

¹ Department of Earth and Space Science, Osaka University, Osaka 560-0043, Japan; kmasuda@ess.sci.osaka-u.ac.jp

² Department of Astronomy & Astrophysics, 525 Davey Laboratory, The Pennsylvania State University, University Park, PA 16802, USA

³ Center for Exoplanets and Habitable Worlds, 525 Davey Laboratory, The Pennsylvania State University, University Park, PA 16802, USA

⁴ Astrobiology Center, 2-21-1 Osawa, Mitaka, Tokyo 181-8588, Japan

⁵ National Astronomical Observatory of Japan, 2-21-1 Osawa, Mitaka, Tokyo 181-8588, Japan

⁶ Astronomical Science Program, Graduate University for Advanced Studies, SOKENDAI, 2-21-1, Osawa, Mitaka, Tokyo, 181-8588, Japan

⁷ JHU Applied Physics Laboratory, 11100 Johns Hopkins Road, Laurel, MD 20723, USA

⁸ Carnegie Science Earth and Planets Laboratory, 5241 Broad Branch Road, NW, Washington, DC 20015, USA

⁹ Carnegie Science Observatories, 813 Santa Barbara Street, Pasadena, CA 91101, USA

¹⁰ Department of Physics and Astronomy, Johns Hopkins University, Baltimore, MD, USA

¹¹ Department of Physics & Astronomy, The University of California, Irvine, Irvine, CA 92697, USA

¹² Division of Geological and Planetary Sciences, California Institute of Technology, Pasadena, CA 91125, USA

¹³ Department of Astronomy, University of Washington, Seattle, WA 98195, USA

¹⁴ Jet Propulsion Laboratory, California Institute of Technology, Pasadena, CA 91011, USA

¹⁵ Department of Astrophysical and Planetary Sciences, University of Colorado Boulder, Boulder, CO 80309, USA

¹⁶ NASA Goddard Space Flight Center, 8800 Greenbelt Road, Greenbelt, MD 20771, USA

¹⁷ Department of Physics and Trottier Space Institute, McGill University, 3600 rue University, H3A 2T8 Montréal, QC, Canada

¹⁸ Trottier Institute for Research on Exoplanets (iREX), Université de Montréal, QC, H3C 3J7, Canada

¹⁹ Hobart and William Smith Colleges, Geneva, NY 14456, USA

²⁰ Cornell University, Ithaca, NY 14853, USA

²¹ Frontier Research Institute for Interdisciplinary Sciences, Tohoku University, 6-3 Aramaki aza Aoba, Aoba-ku, Sendai, Miyagi 980-8578, Japan

²² Department of Geophysics, Graduate School of Science, Tohoku University, 6-3 Aramaki aza Aoba, Aoba-ku, Sendai, Miyagi 980-8578, Japan

²³ Cluster for Pioneering Research, RIKEN, 2-1 Hirosawa, Wako, Saitama 351-0198, Japan

²⁴ Department of Astronomy, University of Texas at Austin, Austin, TX 78722, USA

²⁵ Division of Science, National Astronomical Observatory of Japan, 2-21-1 Osawa, Mitaka-shi, Tokyo, Japan

²⁶ Department of Earth and Planetary Sciences, University of California Santa Cruz, Santa Cruz, CA, USA

²⁷ School of Earth and Space Exploration, Arizona State University, Tempe, AZ, USA

²⁸ Department of Astronomy, University of Maryland, College Park, MD, USA

²⁹ SETI Institute, NASA Ames Research Center, Mountain View, CA 94043, USA

³⁰ Komaba Institute for Science, The University of Tokyo, 3-8-1 Komaba, Meguro, Tokyo 153-8902, Japan

³¹ Instituto de Astrofísica de Canarias (IAC), 38205 La Laguna, Tenerife, Spain

³² Department of Multi-Disciplinary Sciences, Graduate School of Arts and Sciences, The University of Tokyo, 3-8-1 Komaba, Meguro, Tokyo 153-8902, Japan

³³ Astrobiology Center, 2-21-1 Osawa, Mitaka, Tokyo 181-8588, Japan National Astronomical Observatory of Japan, 2-21-1 Osawa, Mitaka, Tokyo 181-8588, Japan

³⁴ Instituto de Astrofísica de Canarias (IAC), Calle Vía Láctea s/n, 38200, La Laguna, Tenerife, Spain

³⁵ Departamento de Astrofísica, Universidad de La Laguna, E-38206 La Laguna, Tenerife, Spain

³⁶ Department of Physics and Astronomy, University of the Pacific, 601 Pacific Avenue, Stockton, CA 95211, USA

³⁷ Center for Astrophysics | Harvard & Smithsonian, 60 Garden Street, Cambridge, MA 02138, USA

³⁸ Acton Sky Portal (private observatory), Acton, MA 01720, USA

³⁹ Astrobiology Research Unit, University of Liège, Allée du 6 août, 19, 4000 Liège (Sart-Tilman), Belgium

⁴⁰ Department of Earth, Atmospheric and Planetary Sciences, MIT, 77 Massachusetts Avenue, Cambridge, MA 02139, USA

⁴¹ Instituto de Astrofísica de Andalucía (IAA-CSIC), Glorieta de la Astronomía s/n, 18008 Granada, Spain

⁴² STAR Institute, University of Liège, Allée du 6 août, 19, 4000 Liège (Sart-Tilman), Belgium

⁴³ Oukaimeden Observatory, High Energy Physics and Astrophysics Laboratory, Cadi Ayyad University, Marrakech, Morocco

⁴⁴ Department of Astronomy, Box 351580, University of Washington, Seattle, WA 98195, USA

⁴⁵ Anton Pannekoek Institute for Astronomy, University of Amsterdam, Science Park 904, 1098 XH Amsterdam, The Netherlands

⁴⁶ Ankara University, Department of Astronomy and Space Sciences, TR-06100, Ankara, Türkiye

⁴⁷ Ankara University, Astronomy and Space Sciences Research and Application Center (Kreiken Observatory), İncek Blvd., TR-06837, Ahlatlıbel, Ankara, Türkiye

⁴⁸ Grand-Pra Observatory, 1984 Les Hauderes, Switzerland⁴⁹ Wild Boar Remote Observatory, San Casciano in val di Pesa, Firenze 50026, Italy⁵⁰ Department of Physics & Astronomy, Johns Hopkins University, 3400 N. Charles Street, Baltimore, MD 21218, USA; jer5346@psu.edu

Received 2024 June 29; revised 2024 September 28; accepted 2024 October 3; published 2024 December 3

Abstract

Kepler-51 is a $\lesssim 1$ Gyr old Sun-like star hosting three transiting planets with radii $\approx 6\text{--}9 R_{\oplus}$ and orbital periods $\approx 45\text{--}130$ days. Transit timing variations (TTVs) measured with past Kepler and Hubble Space Telescope (HST) observations have been successfully modeled by considering gravitational interactions between the three transiting planets, yielding low masses and low mean densities ($\lesssim 0.1 \text{ g cm}^{-3}$) for all three planets. However, the transit time of the outermost transiting planet Kepler-51d recently measured by the James Webb Space Telescope 10 yr after the Kepler observations is significantly discrepant from the prediction made by the three-planet TTV model, which we confirmed with ground-based and follow-up HST observations. We show that the departure from the three-planet model is explained by including a fourth outer planet, Kepler-51e, in the TTV model. A wide range of masses ($\lesssim M_{\text{Jup}}$) and orbital periods ($\lesssim 10$ yr) are possible for Kepler-51e. Nevertheless, all the coplanar solutions found from our brute-force search imply masses $\lesssim 10 M_{\oplus}$ for the inner transiting planets. Thus, their densities remain low, though with larger uncertainties than previously estimated. Unlike other possible solutions, the one in which Kepler-51e is around the 2:1 mean motion resonance with Kepler-51d implies low orbital eccentricities ($\lesssim 0.05$) and comparable masses ($\sim 5 M_{\oplus}$) for all four planets, as is seen in other compact multiplanet systems. This work demonstrates the importance of long-term follow-up of TTV systems for probing longer-period planets in a system.

Unified Astronomy Thesaurus concepts: Exoplanet astronomy (486); Hubble Space Telescope (761); Transit photometry (1709); Transit timing variation method (1710); Transits (1711); James Webb Space Telescope (2291)

Materials only available in the online version of record: machine-readable table

1. Introduction

Kepler-51 is a G-type star hosting unusually low density planets. The star’s ≈ 8 -day rotation period as measured from its $\sim 1\%$ quasi-periodic flux modulation suggests youth (~ 0.5 Gyr; L. M. Walkowicz & G. S. Basri 2013; J. E. Libby-Roberts et al. 2020). It has three Saturn-sized transiting planets (N. M. Batalha et al. 2013; J. H. Steffen et al. 2013) with orbital period ratios close to 1:2:3 (45 days, 85 days, and 130 days for Kepler-51b, c, and d, respectively) detected with Kepler photometry. The inner two planets were confirmed by J. H. Steffen et al. (2013), who demonstrated a significant anticorrelation in their transit timing variations (TTVs) and constrained their masses to be less than a few times that of Jupiter, considering dynamical stability. K. Masuda (2014) presented TTVs for the outermost transiting planet, Kepler-51d, and numerically modeled the TTVs of the three planets, finding that they all have masses of $< 10 M_{\oplus}$ and mean densities of $\sim 0.1 \text{ g cm}^{-3}$. The TTV-based mass measurements have been confirmed in other works (E. Agol & K. Deck 2016; S. Hadden & Y. Lithwick 2017; J. E. Libby-Roberts et al. 2020).

The nature of the Kepler-51 “super-puff” planets (E. J. Lee & E. Chiang 2016) remains elusive. For example, their large inferred gas mass fractions ($> 15\%$; E. D. Lopez & J. J. Fortney 2014) challenge formation theories, with one proposed explanation positing rapid gas accretion in a dust-free, cold outer disk followed by inward migration (E. J. Lee & E. Chiang 2016; Y. Chachan et al. 2021). Alternatively, their large sizes could be due to a hotter interior caused by obliquity tides inflating the

observed radii (S. Millholland 2019) instead of a high gas mass fraction. Meanwhile, their low gravity implies high atmospheric loss rates (assuming clear atmospheres) that may result in shorter gas envelope lifetimes than the age of the system (L. Wang & F. Dai 2019), making their low densities a mystery.

Hubble Space Telescope (HST) Wide Field Camera 3 (WFC3) observations of the transmission spectra of Kepler-51b and d between 1.1 and $1.7 \mu\text{m}$ showed no detectable features (J. E. Libby-Roberts et al. 2020), which has led to the development of two hypotheses to explain both the flat spectra and the large sizes of the planets. One hypothesis involves optically thick, high-altitude dust and haze layers entrained in atmospheric outflows increasing the apparent planet radius by significantly reducing the pressure probed by transmission spectroscopy while simultaneously flattening the spectra (L. Wang & F. Dai 2019; P. Gao & X. Zhang 2020; K. Ohno & Y. A. Tanaka 2021). The other hypothesis employs obliquely oriented planetary rings to block out more of the star than just the planet itself (thereby making the planetary shadow look larger) while also allowing the spectrally gray rings to dominate the transmission spectrum (B. Akınanmi et al. 2020; A. L. Piro & S. Vissapragada 2020; K. Ohno & J. J. Fortney 2022). In both scenarios the planets themselves possess much lower gas mass fractions and higher gravity, thereby reducing their inferred atmospheric loss rates to more reasonable values.

We observed a transit of Kepler-51d with the James Webb Space Telescope (JWST) NIRSpec-PRISM from 0.6 to $5 \mu\text{m}$ ⁵³ and an optical transit with the Apache Point Observatory (APO) simultaneously. While the transmission spectrum will provide key information to characterize the chemical composition of Kepler-51d’s atmosphere, as well as the structure of a potential haze layer, the observation also revealed new aspects of the dynamics of the system: the transit of Kepler-51d

⁵¹ NASA Postdoctoral Fellow.⁵² CITA National Fellow.[†] Joint first authors.⁵³ The transmission spectrum will be presented in a subsequent follow-up publication (J. Libby-Roberts et al. 2024, in preparation).

occurred 2 hr earlier compared to the prediction based on previous transit times and a three-planet TTV model with uncertainties of only 2.7 minutes. The timing offset was confirmed by follow-up HST transit observations of both Kepler-51c and d that will be described herein. In addition, we checked the existing ground-based transit times of Kepler-51d and found that they also consistently deviated from the three-planet model. The simplest explanation is that there is a fourth planet, Kepler-51e, and thus the masses of the three transiting planets derived from the three-planet TTV modeling need to be revisited.

In this paper, we examine the evidence of the fourth planet in the system, Kepler-51e, by utilizing an extensive transit timing data set spanning over 14 yr from various facilities, including JWST, and we update the mass constraints taking into account its presence. In Section 2, we revisit the physical properties of the host star. In Section 3, we present relevant observations and analyses to derive transit times. In Section 4, we check the accuracy of transit time measurements in the presence of a starspot-crossing feature. In Section 5, we describe our TTV model. In Section 6, we discuss evidence of the fourth planet in detail. In Section 7, we explore four-planet TTV solutions and present updated physical parameters of the system. Section 8 discusses the implications of our findings, and Section 9 summarizes the paper.

2. Host Star Mass and Radius

As the TTVs and transit light curves constrain only the planet masses and radii relative to those of the host star, we need external constraints on the stellar mass and radius to determine the physical properties of the planets. We fitted the MIST models (B. Paxton et al. 2011, 2013, 2015; J. Choi et al. 2016; A. Dotter 2016) to the effective temperature T_{eff} and metallicity [Fe/H] of Kepler-51 inferred from high-resolution spectroscopy (see below), K_s magnitude from the Two Micron All Sky Survey (2MASS; M. F. Skrutskie et al. 2006) corrected for extinction using *Bayestar17* (G. M. Green et al. 2018), and the parallax from Gaia DR3 (Gaia Collaboration et al. 2023) corrected for zero-point offset (L. Lindegren et al. 2021) and underestimated error (K. El-Badry et al. 2021). We compute the likelihood function as a product of independent Gaussians for each measurement, and we also incorporate the constraint on the stellar age from its rotation period of 8.2 days as measured from Kepler light curves (A. McQuillan et al. 2014), following the method described in R. Angus et al. (2019) using a gyrochrone calibrated to the Praesepe cluster and the Sun. We used the *jaxstar* code (K. Masuda 2022) to perform No U-Turn Sampling (S. Duane et al. 1987; M. Betancourt 2017) of the stellar parameters from the joint posterior probability density function (pdf), assuming a prior pdf uniform in the stellar mass–age–metallicity space.

For $T_{\text{eff}} = 5674$ K and [Fe/H] = 0.047 from the California Kepler Survey (E. A. Petigura et al. 2017) and assuming 110 K and 0.1 dex uncertainties, we found the mass, radius, density, and age to be $0.96 \pm 0.02 M_{\odot}$, $0.87 \pm 0.02 R_{\odot}$, $1.48 \pm 0.06 \rho_{\odot}$, and 0.7 ± 0.5 Gyr, respectively, where the quoted values are the means and standard deviations of the marginal posteriors. The assigned statistical errors of $\approx 2\%$ for the mass and radius are smaller than the systematic error floors set by the fundamental temperature scale and stellar-model dependence, which have been estimated as $\approx 4\%$ for radius and $\approx 5\%$ for mass (J. Taylor et al. 2022). Thus, we inflate the errors

following that work and adopt a stellar mass and radius of $0.96 \pm 0.05 M_{\odot}$ and $0.87 \pm 0.04 R_{\odot}$, respectively, when we convert the planet-to-star mass/radius ratios to the planet masses/radii. The values are consistent with those based on the Gaia DR2 parallax derived by E. A. Petigura et al. (2022), whose method we essentially followed except for incorporating the gyrochronal information. They are also consistent with those found in J. E. Libby-Roberts et al. (2020), who adopted an age prior from gyrochronology and the parallax from Gaia DR2. Our results remained unchanged, within error bars, when we adopted $T_{\text{eff}} = 5574$ K and [Fe/H] = -0.07 from the Spectral Properties of Cool Stars project (J. M. Brewer & D. A. Fischer 2018).

3. Transit Observations and Data Analysis

Midtransit times of all three Kepler-51 transiting planets were pulled from a wide range of observations spanning 14 yr (2010–2024) of measurements made both from the ground and from space. We provide a full list of transit times for the three transiting planets in Table 1. Below, we detail the observations and analysis of the individual data sets leading to the extraction of each reported midtransit time.

3.1. JWST

We observed a single transit of Kepler-51d with the JWST/NIRSpec-PRISM (S. M. Birkmann et al. 2022) on 2023 June 26 (Cycle 1, GO-2571, PI J. Libby-Roberts) using NIRSpec’s Bright Object Time Series. Given the relative faintness of Kepler-51 (J -mag: 13.56), we utilized 12 groups per integration, with an overall exposure time of 2.9 s and 18,082 total integrations across the ~ 14 hr of observing time. We maintained a well depth $< 75\%$ to avoid significant nonlinearities. To maximize efficiency, we used the NRSRAPID readout, with the S1600A1 slit and the SUB512 subarray.

We reduced the data using the *Eureka!* package (T. J. Bell et al. 2022) starting with Stage 0 uncalibrated files. We performed a Stage 1 reduction following the recommended steps and adopting a cosmic-ray rejection threshold of 8σ (T. J. Bell et al. 2022). We ignored a custom bias subtraction and performed a group-level column background subtraction by fitting a line to the top and bottom 7 pixels of the subarray. Stage 2 reduction followed the recommended steps as outlined in Z. Rustamkulov et al. (2022). For Stage 3 we extracted the source position by fitting a Gaussian and extracting the 1D stellar spectrum by assuming a full-aperture width of 4 pixels. We also performed an overall background subtraction by calculating a column background value from 7 pixels away from the source position. Stage 4 combined the 1D stellar spectrum into a white-light curve by summing the flux from 0.519 to 5.463 μm , with outliers $> 3\sigma$ beyond a rolling median flagged and removed. Figure 1 plots the final broadband light curve of Kepler-51d.

The observations were originally planned to center on the expected midtransit time, leaving ~ 3 hr baseline on either side of the 8.5 hr transit. As the transit occurred earlier than expected, we were left with a 45-minute pre-transit baseline, the first 30 minutes of which demonstrated a slight slope owing to instrument settling (Z. Rustamkulov et al. 2022). We also observed a pronounced starspot-crossing event during the middle of the transit, which was unsurprising given the activity of this star.

Table 1
Transit Times of Kepler-51b, c, and d

Planet	Transit Time (BJD $-2,454,833$)	σ_{lower} (days)	σ_{upper} (days)	Source
b	159.1097	0.0011	0.0011	Kepler
b	204.2631	0.0012	0.0011	Kepler
b	249.4155	0.0013	0.0012	Kepler
b	294.5732	0.0013	0.0013	Kepler
b	339.7272	0.0013	0.0013	Kepler
b	384.8783	0.0012	0.0012	Kepler
b	430.0344	0.0012	0.0012	Kepler
b	520.3435	0.0011	0.0012	Kepler
b	565.5016	0.0013	0.0012	Kepler
b	610.6583	0.0011	0.0012	Kepler
b	655.8134	0.0012	0.0012	Kepler
b	700.9750	0.0013	0.0013	Kepler
b	746.1274	0.0012	0.0012	Kepler
b	791.2877	0.0012	0.0012	Kepler
b	836.4391	0.0012	0.0012	Kepler
b	881.5991	0.0012	0.0011	Kepler
b	926.7537	0.0012	0.0012	Kepler
b	971.9066	0.0013	0.0013	Kepler
b	1017.0599	0.0013	0.0013	Kepler
b	1062.2118	0.0011	0.0011	Kepler
b	1107.3669	0.0011	0.0011	Kepler
b	1152.52080	0.00093	0.00088	Kepler
b	1197.6764	0.0011	0.0011	Kepler
b	1242.83011	0.00092	0.00099	Kepler
b	1287.98472	0.00091	0.00098	Kepler
b	1333.1420	0.0010	0.0010	Kepler
b	1378.2980	0.0010	0.0010	Kepler
b	1423.45414	0.00089	0.00092	Kepler
b	1468.61325	0.00093	0.00098	Kepler
b	1513.7670	0.0010	0.0010	Kepler
b	2462.0321	0.0020	0.0015	HST
b	2732.9527	0.0030	0.0029	HST
b	3500.5934	0.0015	0.0015	m2-LCO
b	3816.6912	0.0019	0.0019	m2
b	5035.8767	0.0011	0.0010	m3
b	5261.6574	0.0011	0.0011	APO
c	210.0118	0.0057	0.0057	Kepler
c	295.3159	0.0043	0.0045	Kepler
c	380.6394	0.0037	0.0039	Kepler
c	465.9534	0.0036	0.0034	Kepler
c	551.2621	0.0037	0.0038	Kepler
c	636.5701	0.0038	0.0038	Kepler
c	892.5190	0.0042	0.0040	Kepler
c	977.8359	0.0056	0.0056	Kepler
c	1148.4634	0.0050	0.0043	Kepler
c	1233.8052	0.0039	0.0042	Kepler
c	1319.1103	0.0046	0.0046	Kepler
c	1489.7539	0.0043	0.0044	Kepler
c	1575.0710	0.0046	0.0046	Kepler
c	3793.2836	0.0078	0.0086	m2
c	4646.4855	0.0040	0.0034	m2
c	5414.3352	0.0084	0.0043	HST
c	5584.9712	0.0047	0.0045	Palomar
d	212.02406	0.00076	0.00076	Kepler
d	342.20782	0.00095	0.00095	Kepler
d	472.39081	0.00079	0.00073	Kepler
d	602.57379	0.00079	0.00073	Kepler
d	862.93213	0.00079	0.00079	Kepler
d	993.10431	0.00073	0.00079	Kepler
d	1123.28449	0.00078	0.00077	Kepler
d	1253.45026	0.00070	0.00070	Kepler
d	1383.62997	0.00076	0.00077	Kepler
d	1513.79021	0.00087	0.00087	Kepler

Table 1
(Continued)

Planet	Transit Time (BJD $-2,454,833$)	σ_{lower} (days)	σ_{upper} (days)	Source
d	2555.2005	0.0015	0.0010	HST
d	2945.7533	0.0011	0.0014	HST
d	3466.4834	0.0044	0.0042	m2
d	3856.991	0.021	0.012	TESS
d	4247.4808	0.0021	0.0023	multiple
d	5288.84734	0.00006	0.00006	JWST
d	5419.0210	0.0014	0.0011	HST

Note. Transit times are medians (x_{50}) of the marginal posterior; σ_{lower} and σ_{upper} are $x_{50} - x_{16}$ and $x_{84} - x_{50}$, where x_{16} and x_{84} are the 16th and 84th percentiles of the marginal posterior, respectively. In calculating the likelihood for the TTV analysis, these measurements were treated as “ $\mu \pm \sigma$,” where $\mu = (x_{84} + x_{16})/2$ and $\sigma = (x_{84} - x_{16})/2$. Abbreviations in the source column are defined as follows: “m2”—MuSCAT2; “m3”—MuSCAT3; “APO”—Apache Point Observatory; “multiple”—TRAPPIST-North, Acton Sky Portal Observatory, AUKR, and KeplerCam.

We modeled the broadband light curve using the starspot package *fleck* (B. Morris 2020), which combines a starspot model with the *batman* transit package (L. Kreidberg 2015). We fit for the spot latitude, longitude, size, and contrast, as well as the transit depth, duration (scaled semimajor axis a/R_* and inclination), and midtransit time. We also fitted the stellar quadratic limb-darkening parameters and applied a second-order polynomial function for detrending. We used *emcee* assuming 50 walkers and 50,000 steps, and we confirmed convergence by checking the autocorrelation lengths of each chain (D. W. Hogg & D. Foreman-Mackey 2018). The best-fit model is included in Figure 1. We determine a midtransit time of $2,460,121.84734 \pm 0.00006$ BJD for Kepler-51d. Other planetary and stellar parameters will be reported and discussed in further detail in a separate planned publication (J. Libby-Roberts et al. 2024, in preparation).

3.2. HST

Two full transits each of Kepler-51b and d were observed with HST between 2015 and 2017 and were analyzed by J. E. Libby-Roberts et al. (2020; Cycle 23, GO 14218, PI Z. Berta-Thompson). For these transits, we adopted the transit times reported therein. More recently, HST observed a single transit each of Kepler-51c and d using the WFC3/G141 mode (Cycle 30, GO/DD 17585, PI P. Gao & J. Libby-Roberts). Each observation lasted six HST orbits (~ 8.8 hr). The Kepler-51c observation was impacted by HST crossing the South Atlantic Anomaly (SAA) during orbits 3–6. This limited the number of frames to 10–12 per HST orbit. Otherwise, we obtained 23 frames per orbit. The Kepler-51c observation was also impacted by a guide star acquisition failure in the first HST orbit. Fortunately, HST was able to acquire the guide star in the subsequent orbit, and the remainder of the observations proceeded normally. We purposefully obtained a partial transit of Kepler-51d, due to its long duration. Since the transit duration is well-known, we were able to precisely constrain the midtransit time by fitting the ingress.

The Kepler-51c and d visits were both observed and reduced using the following procedure. Each HST orbit started with a direct image using the F139M filter (GRISM256, NSAMP = 15, SAMP-SEQ = RAPID, 4.167 s exposures). We then acquired

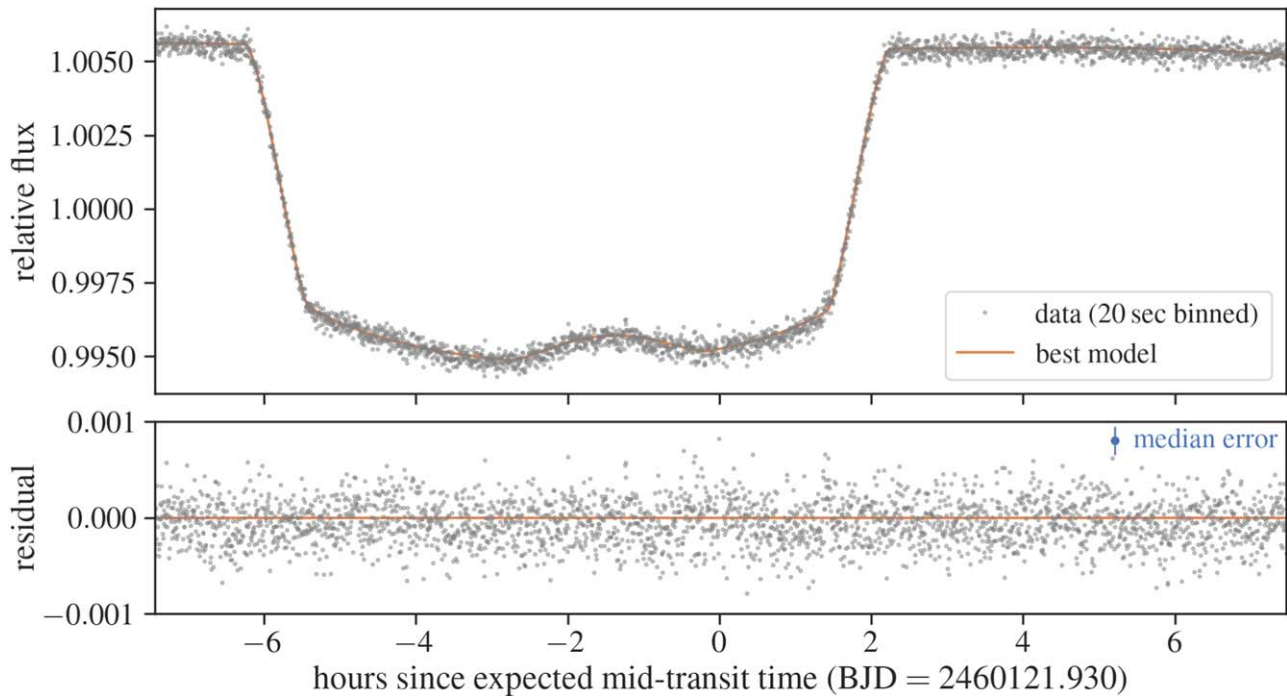


Figure 1. White-light curve (0.519–5.463 μm) of Kepler-51d observed with JWST NIRSpec/PRISM. The pronounced bump near the center of the transit is due to a starspot-crossing event. The best-fit model is included in orange, which is a combination of transit+starspot and systematics. The horizontal axis indicates the time (hours) since the expected midtransit time based on the previous three-planet TTV model. The observed midtransit time is significantly offset from the prediction.

spectroscopic data using the G141 grism (GRISM256, NSAMP = 15, SAMP-SEQ = SPARS10, 103 s exposures). The faintness of Kepler-51 permitted us to use WFC3’s “stare” mode as opposed to the spatial scan mode, which is often done with time-series observations of bright targets.

We used the Eureka! data reduction pipeline (T. J. Bell et al. 2022) to convert the FLT data files into a time series of 1D spectra. Because WFC3 was operating in stare mode, there was no benefit to using the IMA files. Starting with Stage 3, we selected a relatively small subarray region ($x = 58\text{--}200$ pixels, $y = 137\text{--}170$ pixels) to avoid nearby stars in this crowded field. To search for outliers in the background region, we performed a double-iteration, 5σ rejection threshold test for each pixel along the time axis. We then performed column-by-column background subtraction by masking the region within 8 pixels of the trace and fitting for a constant term for each column. We further rejected pixels above a 2.5σ threshold in order to remove a visibly hot pixel from one of the columns. We adopted a full-width aperture size of 7 pixels, centered on the trace, and used optimal spectral extraction (K. Home 1986) to estimate the flux in each frame.

In Stage 4 of Eureka!, we measured and corrected for a slight drift in the position of the 1D spectra (<0.15 pixels) over the course of each observation. In computing the white-light curves, we summed flux from 1.125 to 1.65 μm . Prior to fitting the white-light curves (Stage 5), we manually clipped the first good HST orbit and the first frame within each orbit. Because the guide star acquisition failed for the first orbit of the Kepler-51c observations, we effectively clipped the second HST orbit, leaving only four good orbits to work with. We used an exponential plus linear function to fit the repeating ramp in each HST orbit. When fitting the transit shape using batman (L. Kreidberg 2015), we fixed the orbital period, semimajor axis, and inclination to the values listed in Table 2. We fixed the quadratic limb-darkening parameters to $u_1 = 0.235$ and $u_2 = 0.195$ computed by J. E. Libby-Roberts et al. (2020). We

Table 2
Fixed Orbital Parameters for Kepler-51c and Kepler-51d from K. Masuda (2014)

Orbital Parameter	Kepler-51c	Kepler-51d
Period (days)	85.31	130.18
Inclination (deg)	89.38	89.885
Semimajor axis (R_*)	94.1	124.7

Note. These parameters were fixed for our HST white-light-curve fits.

found transit times of $2460247.33520^{+0.0043}_{-0.0084}$ for Kepler-51c and $2460252.02100^{+0.0011}_{-0.0014}$ for Kepler-51d. Figure 2 plots the Kepler-51c and d HST light curves with the best-fit model derived from this analysis.

We also performed two additional, independent HST analyses, and the midtransit times agree to within 1σ . The choice of different reduction midtransit times does not meaningfully change our TTV inference.

3.3. Kepler

Transit times based on the Kepler observations have been reported in multiple works (e.g., K. Masuda 2014; T. Holczer et al. 2016; J. E. Libby-Roberts et al. 2020). Here we reanalyze the whole set of available Kepler light curves in a uniform manner, since some of the transits (including the simultaneous transits of planets b and d) were not incorporated in these analyses.

All available Pre-search Data Conditioning light curves for Kepler-51 were downloaded from the Mikulski Archive for Space Telescopes⁵⁴ using the Lightkurve package (Lightkurve Collaboration et al. 2018). The time series show a $\sim 1\%$ quasi-periodic variation that has been attributed to starspots

⁵⁴ <https://archive.stsci.edu>

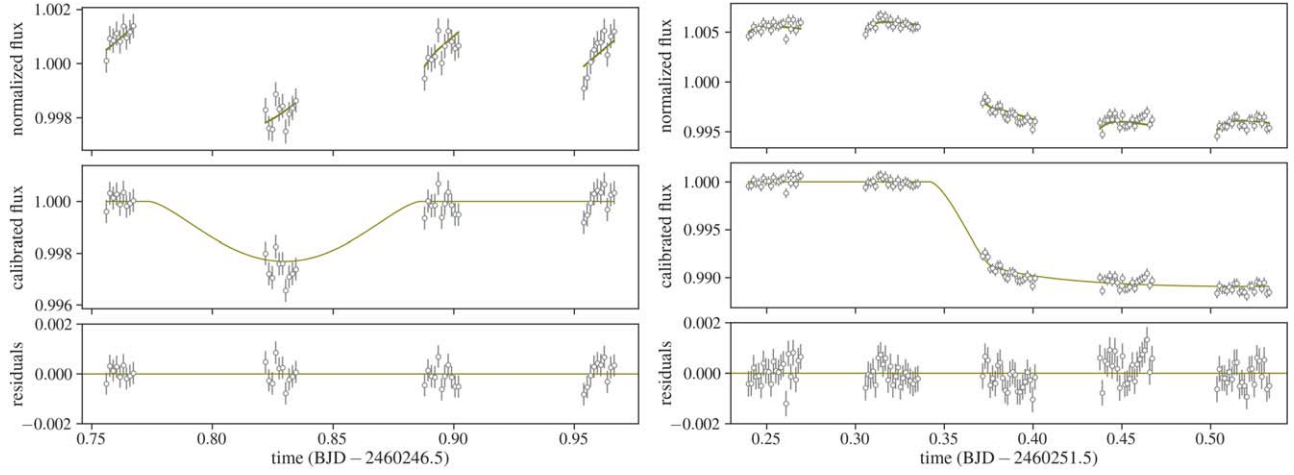


Figure 2. New HST transits of Kepler-51c (left) and d (right). The top panels show the normalized flux (circles) and the model including the transit, polynomial baseline, and HST ramp (solid line). The middle panels show the data and the model after removing the systematic model (polynomial and ramp). The bottom panels show the residuals of the fits.

rotating in and out of view in sync with the 8.2-day rotation of the star (A. McQuillan et al. 2014). We first normalized the flux in each quarter by its median, and we removed the quasi-periodic modulation by fitting the data from each quarter separately using a Gaussian process (GP; S. Aigrain & D. Foreman-Mackey 2023) and by subtracting the mean prediction from it. We excluded the data with nonzero quality flags assigned, and we masked the data around known transits when computing the likelihood for fitting. The width of the transit mask was chosen to be 1.5 times the transit duration reported in the Kepler Object of Interest catalog. Here we assumed the following likelihood function given by a multivariate normal distribution \mathcal{N} :

$$\mathcal{L}(\mu, \alpha, \rho, \sigma_{\text{jit}}) = \mathcal{N}(f; \mu, \Sigma). \quad (1)$$

The flux f is a vector of a length equal to the number of data points in a quarter. The mean flux μ is a vector of the same length, here taken to be constant and characterized by a single scalar. The ij elements of the covariance matrix Σ consist of the Matérn-3/2 covariance function and the white-noise term:

$$\Sigma_{ij} = (\sigma_i^2 + \sigma_{\text{jit}}^2)\delta_{ij} + \alpha^2 \left(1 + \frac{|t_i - t_j|}{3\rho} \right) \times \exp\left(-\frac{|t_i - t_j|}{3\rho}\right), \quad (2)$$

where δ_{ij} is the Kronecker delta, t_i and σ_i are the time and assigned flux error of the i th data point, and σ_{jit} accounts for the flux scatter in excess of the assigned error, if any. The log-likelihood $\ln \mathcal{L}$ was evaluated using the JAX (J. Bradbury et al. 2018) interface of `celerite2` (D. Foreman-Mackey et al. 2017; D. Foreman-Mackey 2018), and the scalar parameters μ , $\ln \sigma_{\text{jit}}$, α , and ρ were optimized using a truncated Newton algorithm as implemented in `jaxopt` (M. Blondel et al. 2021). The mean of the predictive distribution conditioned on f was computed for the optimal set of the parameters and was subtracted from f . The same procedure was applied to both long- and short-cadence data. We then extracted the normalized and detrended flux within 0.5 days around all the known transits of the three planets for the subsequent analysis.

We estimated transit times by fitting the transit light curves with the flux-loss model f_{model} for a quadratically limb-darkened star (E. Agol et al. 2020). The model was computed assuming circular Keplerian orbits, except that each transit was shifted in time to account for TTVs before being compared to the data. These timing shifts, Δt_{ij} (i is the index for planets, and j is the index for transits), for all transits were optimized along with the impact parameters b and radius ratios r of the three transiting planets and the mean density ρ_* and two limb-darkening coefficients q_1 and q_2 (D. M. Kipping 2013) of the star. Here the linear ephemeris (t_0 and P) was fixed to the values obtained from fitting without TTVs because they are completely degenerate with Δt ; what matters is only the combination $t_{0,i} + P_i \cdot j + \Delta t_{ij}$, and this is the transit time reported in Table 1. For the long-cadence data, we oversampled the model by a factor of 11 to account for the finite exposure time, and the simultaneous transits by planets b and d were modeled simply by summing the flux losses from the two planets (i.e., without considering the overlap). The noise (i.e., difference between the observed flux and the model light curve f_{model}) was again modeled using a GP with the kernel in Equation (2); the likelihood function is

$$\mathcal{L}(\Delta t, b, r, \rho_*, q_1, q_2, \mu, \alpha, \rho, \sigma_{\text{jit}}) = \mathcal{N}(f - f_{\text{model}}; \mu, \Sigma). \quad (3)$$

We draw posterior samples for all the parameters, including Δt adopting uniform priors, where $|\Delta t|$ was restricted to be less than 100 minutes. The sampling was performed using Hamiltonian Monte Carlo (HMC) and the No U-Turn Sampler (NUTS; S. Duane et al. 1987; M. Betancourt 2017) as implemented in `NumPyro` (E. Bingham et al. 2018; D. Phan et al. 2019). The long- and short-cadence data were modeled separately, and we adopted transit times from the short-cadence data when available. The results of this analysis are presented in Figures 3–5 and Table 1. The estimated midtransit times and their errors agreed well with those reported in J. E. Libby-Roberts et al. (2020) for the transits that were also analyzed in that work: the difference in the best estimates normalized by the error bars is 0.05 ± 0.45 , and the ratio of the error bars is 1.0 ± 0.2 .

To obtain the prior information on the radius ratios, transit durations (here taken to be the total duration T_{14} defined in J. N. Winn 2011), and impact parameters for the analyses of the

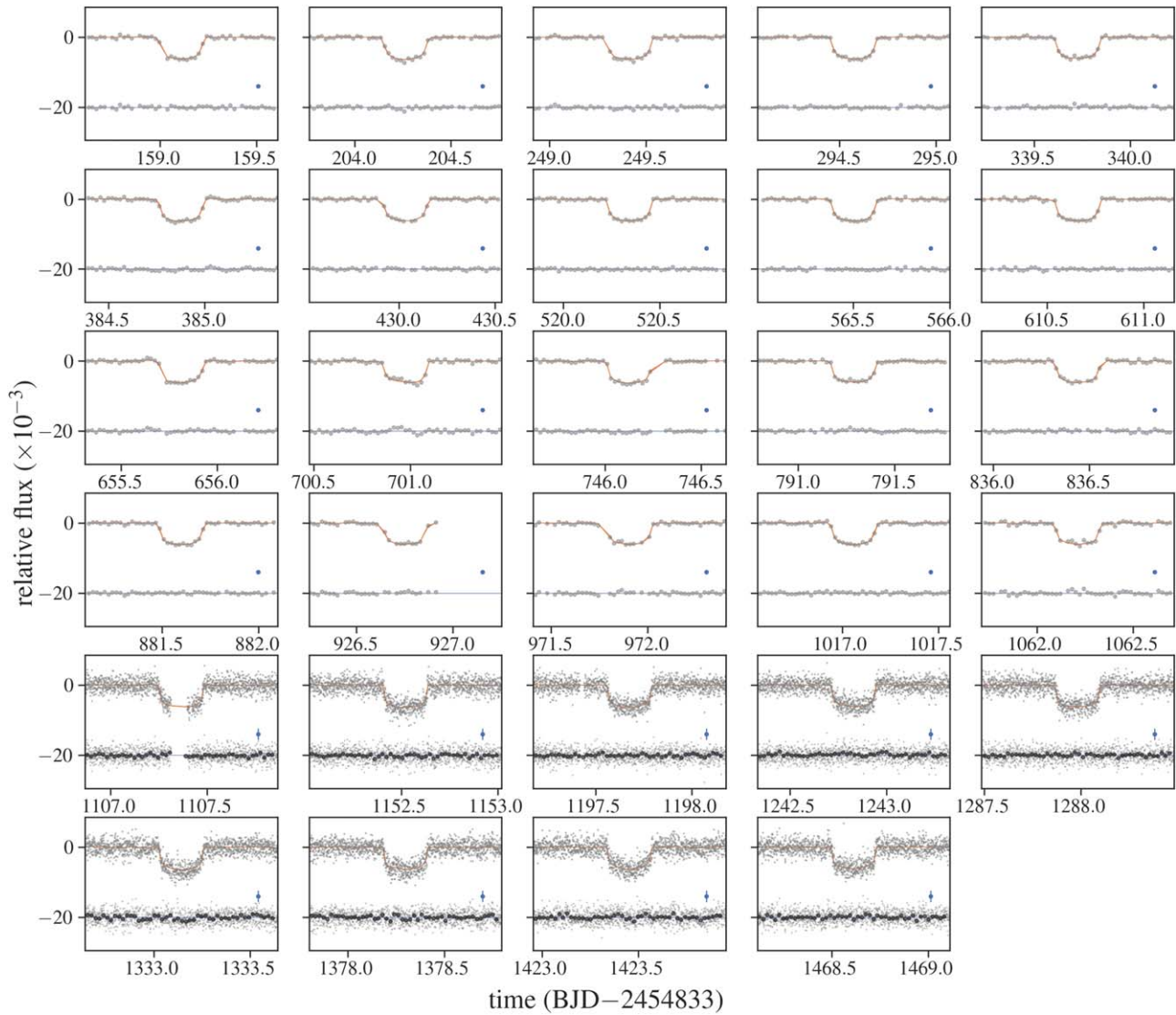


Figure 3. Transit light curves of Kepler-51b from Kepler. The orange lines show 20 GP-included models drawn from the posterior. Residuals from the mean model without GP are shown with offsets. The blue dots above the residuals show the median of the errors assigned to the fluxes. The data around the simultaneous transits of Kepler-51b and Kepler-51d are shown in Figure 5.

ground-based transits (Section 3.4), we fit their marginal posteriors from the long-cadence data with normal distributions and truncated normal distributions with a lower bound of zero. The estimated means and standard deviations (location and scale parameters) are summarized in Table 3. The mean stellar densities inferred from the long- and short-cadence data are $1.72 \pm 0.04 \rho_{\odot}$ and $1.68 \pm 0.06 \rho_{\odot}$ (mean and standard deviation), respectively. These values are consistent with the stellar mass and radius derived in Section 2, accounting for the systematic errors and with low orbital eccentricities (\lesssim a few %) inferred from the TTV modeling.

3.4. Ground-based Facilities

We observed four transits of Kepler-51b, three transits of Kepler-51c, and three transits of Kepler-51d with a variety of ground-based facilities between 2018 and 2023, which we detail below.

3.4.1. Teide Observatory

We used the MuSCAT2 multiband imager (N. Narita et al. 2019) installed at the 1.52 m Telescopio Carlos Sanchez (TCS)

at the Teide Observatory, Spain, to observe transits of the Kepler-51 planets simultaneously in g , r , i , and z_s . Transits of planet b were observed on the nights of UT 2018 August 2 (Figure 6) and 2019 June 14 (Figure 7), planet c was observed on 2019 May 22 (Figure 8) and 2021 September 21 (Figure 9), and planet d was observed on 2018 June 29 (Figure 10). Exposure times (typically 30–60 s) were chosen to avoid saturation and maximize the duty cycle, while enabling precise auto-guiding of the telescope. However, they varied from night to night depending on the atmospheric seeing conditions and focus setting of the telescope. The images were calibrated and light curves were produced following A. Fukui et al. (2011).

We fit the MuSCAT2 light curves using PyMC3 (J. Salvatier et al. 2016), exoplanet⁵⁵ (D. Foreman-Mackey et al. 2020), and starry (R. Luger et al. 2019). We obtained transit timing measurements by simultaneously fitting the light curves from all bandpasses of each observation/data set. We used a wide uniform prior for the time of midtransit, Gaussian priors

⁵⁵ <https://docs.exoplanet.codes/en/stable/>

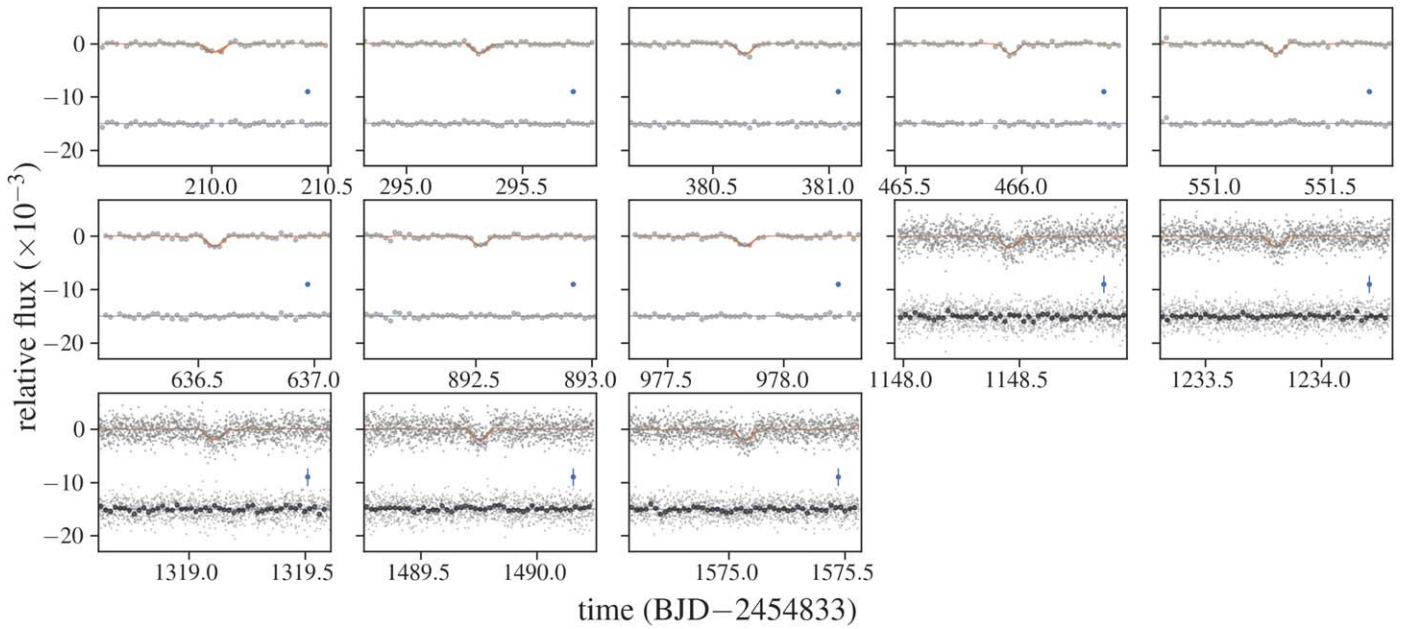


Figure 4. Same as Figure 3, but for Kepler-51c.

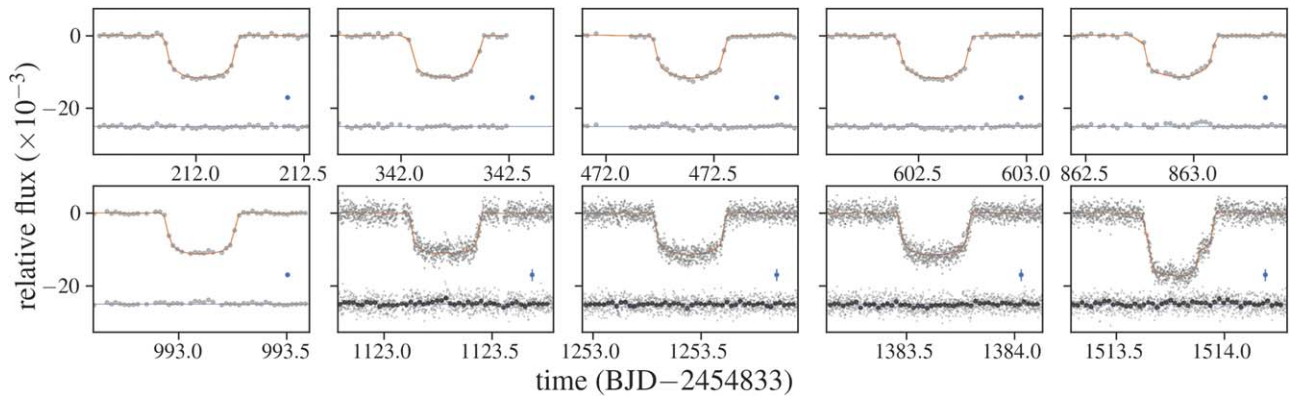


Figure 5. Same as Figure 3, but for Kepler-51d. In the last panel, both Kepler-51b and d are transiting simultaneously.

Table 3
Transit Shape Parameters from the Kepler Long-cadence Data

Parameter	Location	Scale
Kepler-51b		
Radius ratio	0.07225	0.00030
Impact parameter	0.074	0.072
Total transit duration (days)	0.23975	0.00084
Kepler-51c		
Radius ratio ^a	0.068	0.015
Impact parameter ^a	0.988	0.020
Total transit duration (days)	0.1126	0.0035
Kepler-51d		
Radius ratio	0.09857	0.00037
Impact parameter	0.003	0.095
Total transit duration (days)	0.3501	0.0012

Notes. For the impact parameters, the location and scale parameters are for the truncated normal distribution with the lower bound of zero.

^a The marginal posteriors for these parameters are not well approximated by (truncated) normal distributions owing to the grazing nature of Kepler-51c.

for the transit duration and planet-to-star radius ratio, and a truncated Gaussian prior on the impact parameter ($X \sim [\max(0, N(\mu, \sigma), \min(1, N(\mu, \sigma))]$; see Table 3). We computed quadratic limb-darkening coefficients based on interpolation of the parameters tabulated by A. Claret et al. (2012), using the effective temperature, metallicity, and surface gravity of Kepler-51 from J. E. Libby-Roberts et al. (2020). We included separate white-noise jitter parameters for each band to account for underestimated measurement errors and wavelength-dependent systematic noise. Systematics arising from variable atmospheric conditions and intrapixel gain nonuniformity were modeled as a linear combination of auxiliary variables (air mass, centroids, FWHM, and peak flux), as well as either a linear function of time or a third-degree basis spline with five equally spaced knots. We used the gradient-based BFGS algorithm (J. Nocedal & S. J. Wright 2006) implemented in `scipy.optimize` to find initial maximum a posteriori parameter estimates. We used these estimates to initialize an exploration of parameter space via NUTS (M. D. Hoffman & A. Gelman 2014), an efficient gradient-

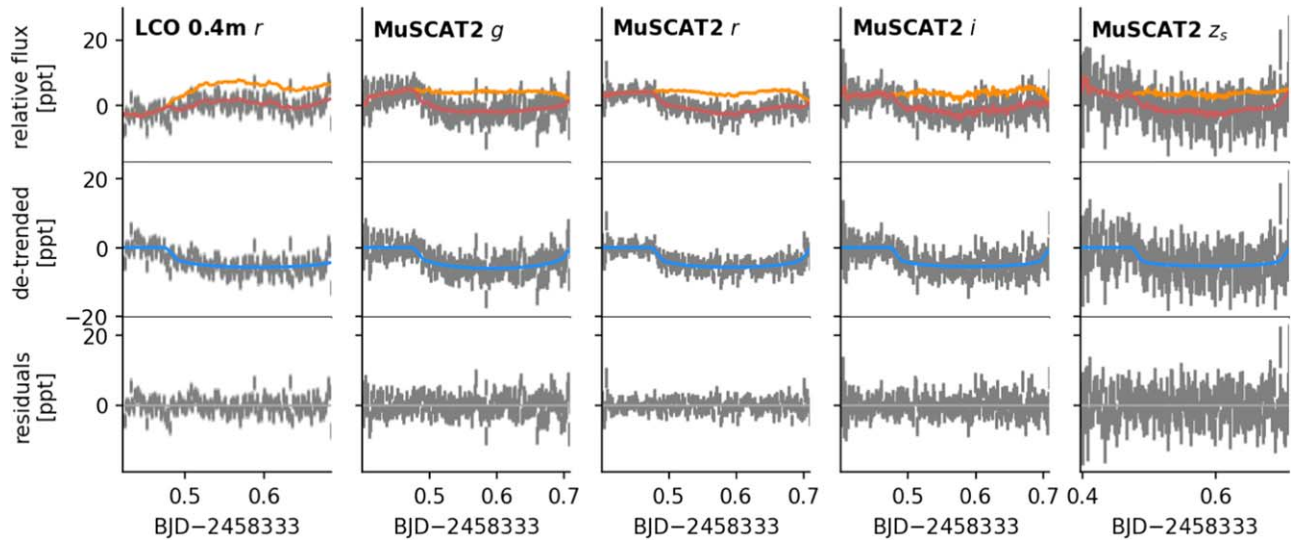


Figure 6. Transit of Kepler-51b observed with LCO (r band) and MuSCAT2 (g , r , i , z_s ; from left to right) on UT 2018 August 2. The gray lines show the measured flux values and their uncertainties, with the quadrature sum of the observed uncertainties and the best-fit jitter value shown in light gray. The top panels show the systematic model (orange) and the systematic + transit model (red). The middle panels compare the detrended flux (measured flux minus the systematic model) with the transit model (blue). The bottom panels show the residuals.

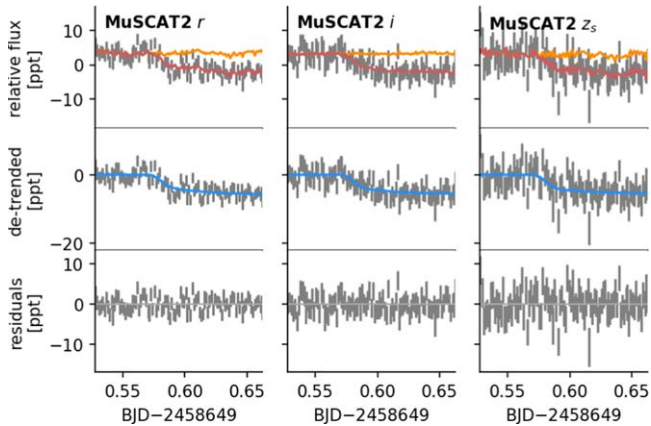


Figure 7. Transit of Kepler-51b observed with MuSCAT2 (r , i , z_s bands; from left to right) on UT 2019 June 14. The format of this figure is the same as that of Figure 6.

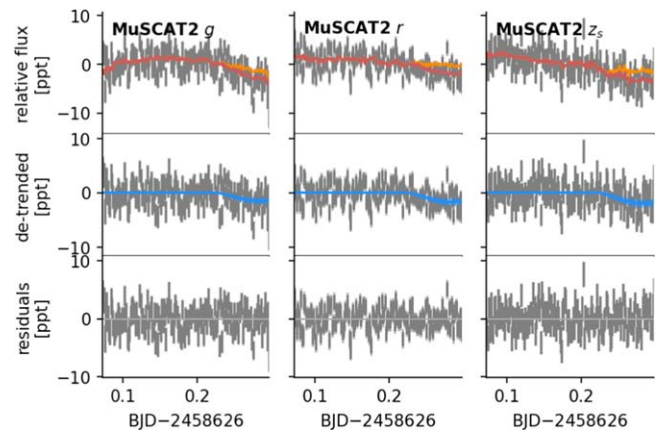


Figure 8. Transit of Kepler-51c observed with MuSCAT2 (g , r , z_s bands; from left to right) on UT 2019 May 22. The format of this figure is the same as that of Figure 6.

based HMC sampler implemented in `PyMC3`. The resulting chains had Gelman–Rubin statistic (A. Gelman & D. B. Rubin 1992) values of <1.01 , indicating that they were well mixed.

3.4.2. Las Cumbres Observatory Global Telescope

We used the SBIG camera mounted on a 0.4 m telescope of the Las Cumbres Observatory Global Telescope (LCOGT) network to observe a transit of Kepler-51b on 2018 August 2 (Figure 6). The telescope we used was physically located at Teide Observatory in Spain. We observed in r band with an exposure time of 150 s. The images were calibrated using the standard LCOGT BANZAI pipeline (C. McCully et al. 2018), and light curves were produced following A. Fukui et al. (2011). As this data set covered the same transit that was observed with MuSCAT2, we analyzed the data jointly with the MuSCAT2 light curves, from that night, as described above.

We used the MuSCAT3 multiband imager (N. Narita et al. 2020) mounted on the LCOGT 2 m Faulkes Telescope North at Haleakala Observatory on Maui, Hawai‘i, to observe a transit of Kepler-51b on UT 2022 October 15 simultaneously in the

g , r , i , z_s bands, using exposure times of 60 s (Figure 11). The images were calibrated using the LCOGT BANZAI pipeline, and light curves were produced following A. Fukui et al. (2011). We measured the midtransit time by simultaneously fitting the four MuSCAT3 light curves, as was done for the MuSCAT2 light curves (see Section 3.4.1).

3.4.3. Oukaïmeden Observatory

We observed an egress of Kepler-51d on 2020 August 18 with the TRAnspiting Planets and PlanetesImals Small Telescope (TRAPPIST-North) 60 cm robotic telescope at the Oukaïmeden Observatory in Morocco (E. Jehin et al. 2011; M. Gillon et al. 2011; K. Barkaoui et al. 2019) as part of TESS Follow-up Observing Program (TFOP-SG1) photometric follow-up (Figure 12). The transit was observed in the $I+z$ filter with an exposure time of 120 s. We reduced the photometry data and performed aperture photometry using the PROSE pipeline (L. J. Garcia et al. 2021) assuming a $4''$ aperture and using five comparison stars. We measured the

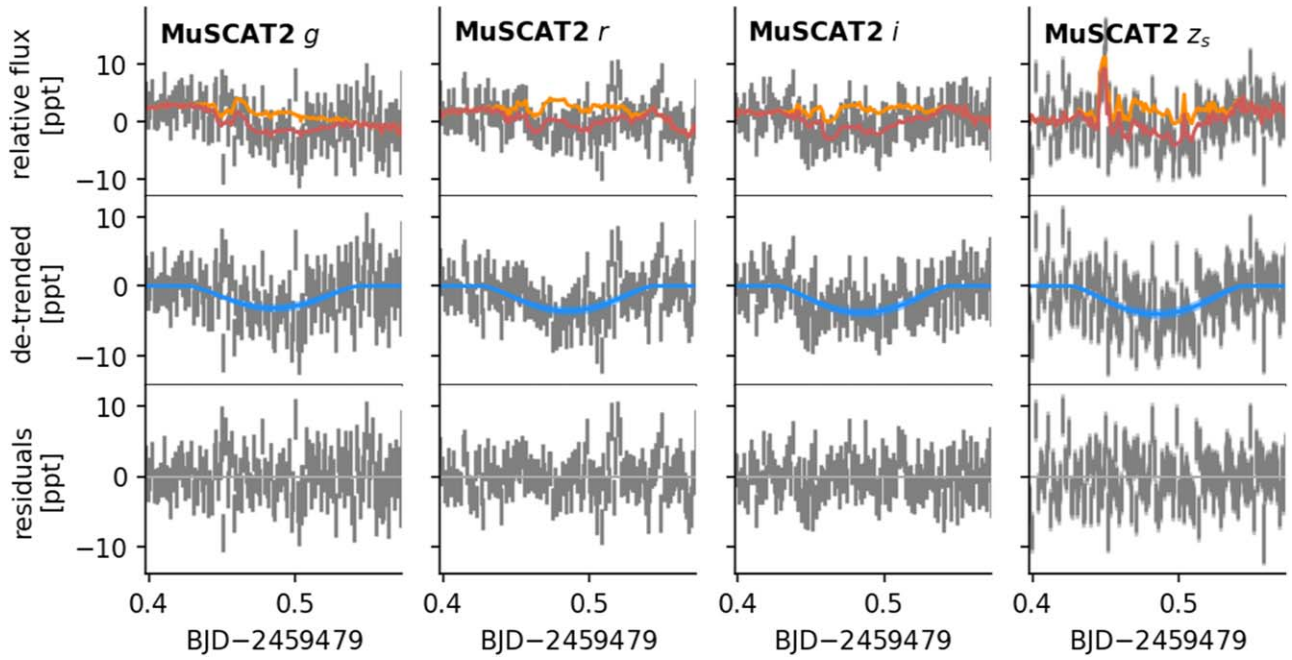


Figure 9. Transit of Kepler-51c observed with MuSCAT2 (g , r , i , z_s bands; from left to right) on UT 2019 September 21. The format of this figure is the same as that of Figure 6.

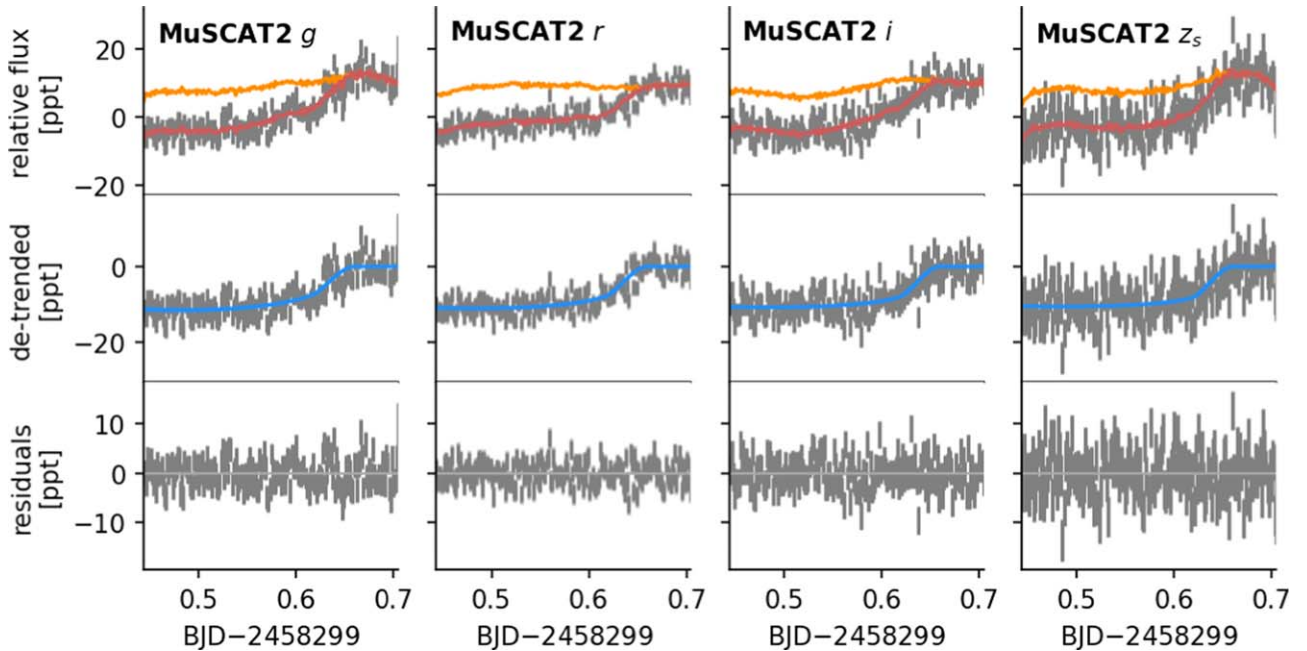


Figure 10. Transit of Kepler-51d observed with MuSCAT2 in g , r , i , and z_s bands (from left to right) on UT 2018 June 29. The format of this figure is the same as that of Figure 6.

midtransit time by simultaneously fitting the TRAPPIST-North light curve along with other light curves of the same transit described in Sections 3.4.4–3.4.6, as was done for the MuSCAT2 light curves (see Section 3.4.1).

3.4.4. Acton Sky Portal Observatory

The same 2020 August 18 egress of Kepler-51d was observed using the 0.36 m telescope on the Acton Sky Portal private observatory in Acton, Massachusetts, with a blue blocking clear Astrodon exoplanet filter (Figure 12). We used

60 s exposure times and used *AstroImageJ* (K. A. Collins et al. 2017) to reduce and perform aperture photometry on the images. The egress ended ~ 36 minutes early, and we experienced a meridian flip during the start of egress, which we accounted for during fitting.

3.4.5. AUKR

We observed the same 2020 August 18 transit of Kepler-51d in g' and r' filters with the Apogee Alta U47 CCD camera attached to the T80 Telescope located at the Ankara University

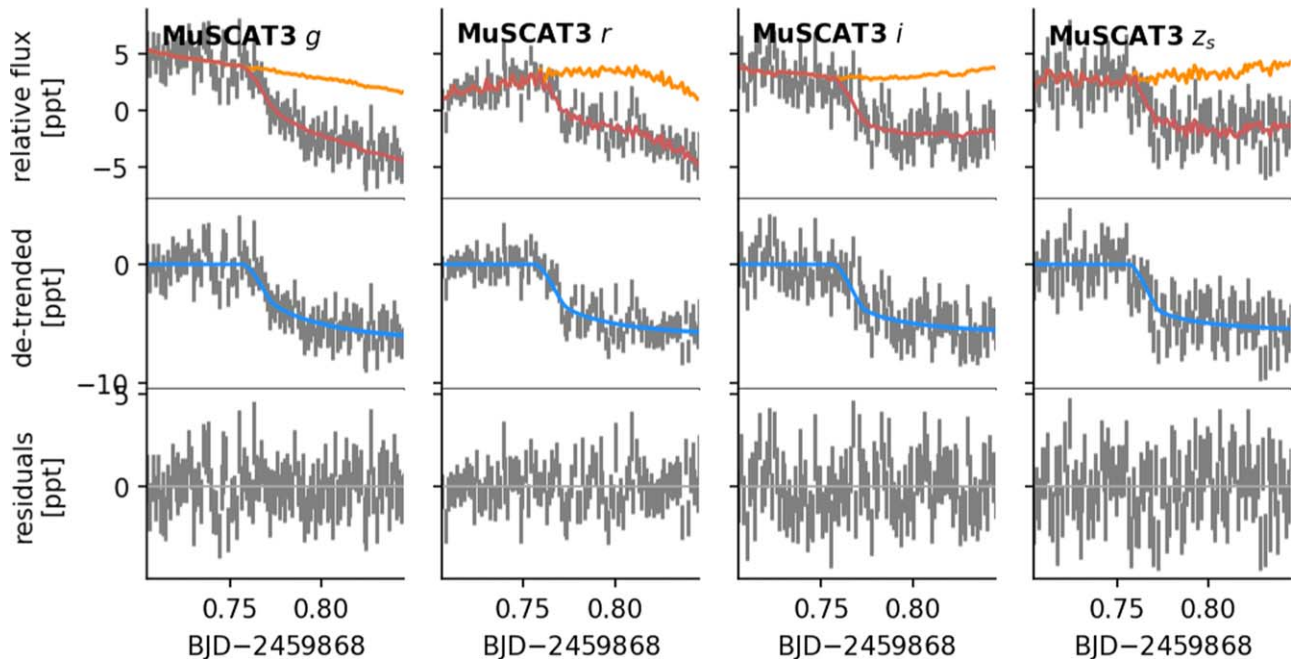


Figure 11. Transit of Kepler-51b observed with MuSCAT3 (g , r , i , z_s bands; from left to right) on UT 2022 October 15. The format of this figure is the same as that of Figure 6.

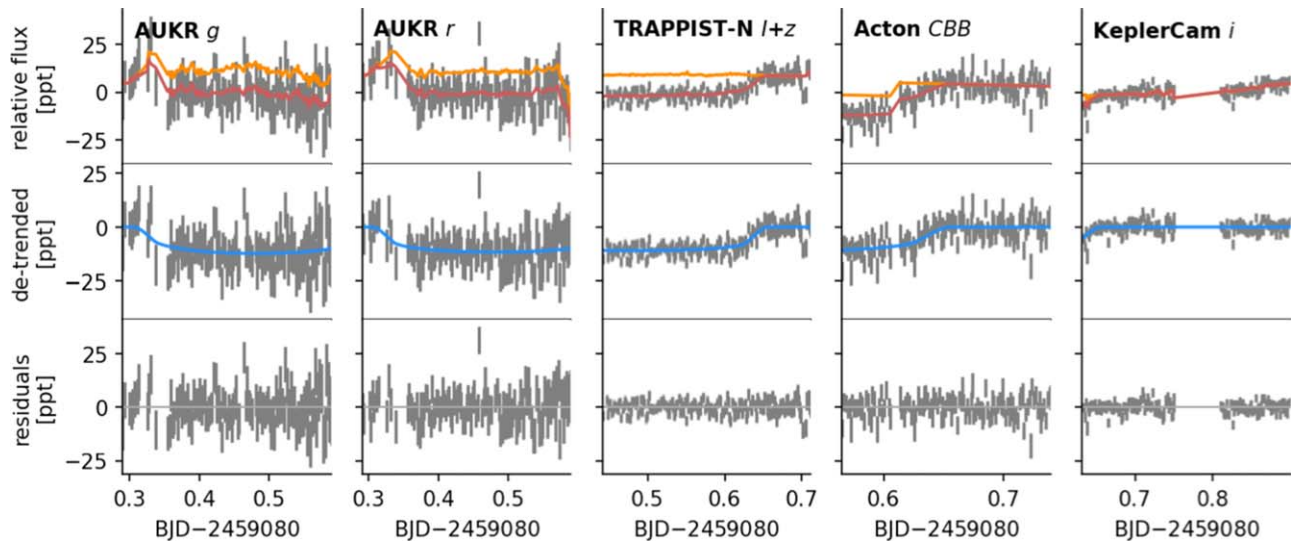


Figure 12. Transit of Kepler-51d observed from the AUKR observatory (g' and r' filters), the TRAPPIST-North telescope ($I+z$ filter), the Acton Sky Portal observatory (blue blocking clear Astrodon filter), and FLWO KeplerCam (Sloan i) on UT 2020 August 18. The format of this figure is the same as that of Figure 6.

Kreiken Observatory (AUKR). The exposure time for both g' and r' filters is 90 s. We used *AstroImageJ* (K. A. Collins et al. 2017) to reduce and perform aperture photometry on the images. The reduced data include an ingress and partial transit (Figure 12).

3.4.6. KeplerCam

We used the KeplerCam CCD mounted on the 1.2 m telescope at the Fred Lawrence Whipple Observatory (FLWO) at Mount Hopkins, Arizona, to observe the same 2020 August 18 transit of Kepler-51d. KeplerCam is a 4096×4096 Fairchild CCD 486 detector that has a field of view of $23' \times 23'$ and an image scale of $0''.672 \text{ pixel}^{-1}$ when binned by two. The observation covered a part of the egress as well as a

long out-of-transit baseline (Figure 12). Images were taken in the Sloan i band with 100 s exposure time. Data were reduced using standard IDL routines, and aperture photometry was performed using *AstroImageJ* (K. A. Collins et al. 2017).

3.4.7. Apache Point Observatory

We observed partial transits of Kepler-51b and d with the ARCTIC optical CCD camera (J. Huehnerhoff et al. 2016) attached to the 3.5 m ARC telescope at the APO in Sunspot, New Mexico, on 2023 May 30 and 2023 June 26, respectively—simultaneous with the JWST observations. Due to scheduling, we caught the transit egress baseline for Kepler-51b and ingress transit for Kepler-51d (Figure 13). We used the Sloan Digital Sky Survey (SDSS) r' filter with 15 s exposures and

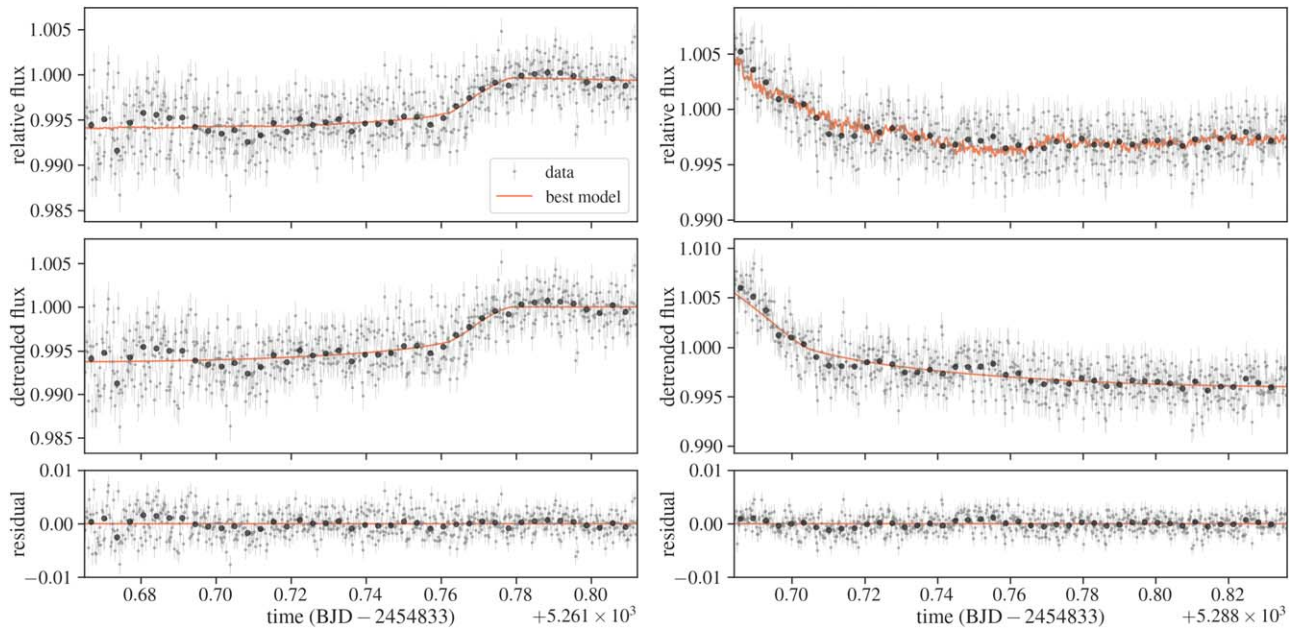


Figure 13. Partial transits of Kepler-51b (left) and Kepler-51d (right) observed with ARCTIC on the 3.5 m APO Telescope. The top panels show the normalized flux (gray dots) and the best-fit transit + systematics model (red solid line). The middle panels show the data and the model after removing the systematic model. The bottom panels show the residuals of the fits. The larger black points represent 5-minute binned data. Due to the transit time and duration, only the ingress and partial transit were observed for Kepler-51d, without any pre-transit baseline.

4×4 detector binning. Due to a nearby companion, we kept the FWHM of the point-spread function (PSF) to $\sim 3''$ over the night to minimize blending by nudging the focus to account for changes in the seeing. Images were bias-subtracted and flat-fielded⁵⁶ before we used `AstroImageJ` (K. A. Collins et al. 2017) to perform differential aperture photometry assuming a $4''$ -aperture radius. Flux errors were assumed to be a combination of photon noise from the star, background, and read noise of the instrument.

We modeled both light curves using the `batman` package, holding the transit duration constant to values reported in J. E. Libby-Roberts et al. (2020) and limb darkening to those reported by `ldtk` (H. Parviainen & S. Aigrain 2015) for Kepler-51 with the SDSS r' bandpass. We detrended the data using air mass, FWHM, sky, and centroid positions as a function of time and fit for the transit depth and midtransit times for both transits. We determined midtransit times of $2,460,094.6574 \pm 0.0011$ BJD for Kepler-51b and $2460121.8492^{+0.0032}_{-0.0043}$ BJD for Kepler-51d. The latter value is consistent with that from the JWST transit reported in Section 3.1. As JWST provides a tighter constraint, we opted to use the JWST time for Kepler-51d for the rest of the analysis.

3.4.8. Palomar

We observed a transit of Kepler-51 c in J with the Wide-field Infrared Camera (WIRC) on the Hale Telescope at Palomar Observatory in California. Palomar/WIRC is a 5.08 m telescope equipped with a 2048×2048 Rockwell Hawaii-II near-IR detector, providing a field of view of $8'.7 \times 8'.7$ with a plate scale of $0''.25 \text{ pixel}^{-1}$ (J. C. Wilson et al. 2003). Our data were taken with a beam-shaping diffuser that increased our observing efficiency and improved the photometric precision and guiding stability (G. Stefansson et al. 2017; S. Vissapragada et al. 2020).

We observed the transit of Kepler-51 c on UT 2024 April 17 from 08:10 to 12:38, between the air masses of 2.11 and 1.07 (Figure 14). Our observing window covered ~ 3.2 hr of pre-ingress baseline and nearly the full transit, ending shortly before transit egress was complete. We collected a total of 302 science images with an exposure time of 45 s per image. We initiated the observations with a five-point dither near the target to construct a background frame that we used to correct for the effects of a known detector systematic at short exposure times. We dark-subtracted, flat-fielded, and corrected for bad pixels following the methodology of S. Vissapragada et al. (2020). We scaled and subtracted the background frame from each science image to remove the full-frame background structure. We then performed circular aperture photometry with the `photutils` package (L. Bradley et al. 2020) on our target plus 10 comparison stars. We tested aperture sizes between 5 and 25 pixels and selected the aperture that minimized the rms deviation of the final photometry, which was 10 pixels. We used uncontaminated sky annuli with inner and outer radii of 70 and 100 pixels, respectively, for local background subtraction.

We fit the light curve using `exoplanet` (D. Foreman-Mackey et al. 2020) with a combined systematics and transit model. Our systematics model includes a linear combination of comparison starlight curves, an error inflation jitter term, and a linear trend. We also tested systematics models with linear combinations of weights for the target centroid offset, PSF width, air mass, and local background. We compared the Bayesian information criterion (G. Schwarz 1978 BIC) for all possible combinations of these systematic noise parameters and found that the model with the optimized BIC value included none of these four parameters. We fit a transit model with the framework of M. Greklek-McKeon et al. (2023), including a wide uniform prior of ± 10 hr on the transit time, normal priors on the radius ratio r , semimajor axis a/R_* , impact parameter b , and orbital period from J. E. Libby-Roberts et al. (2020). We modeled the data with two different limb-darkening frameworks to ensure

⁵⁶ Dark current does not affect ARCTIC images with exposure times < 60 s.

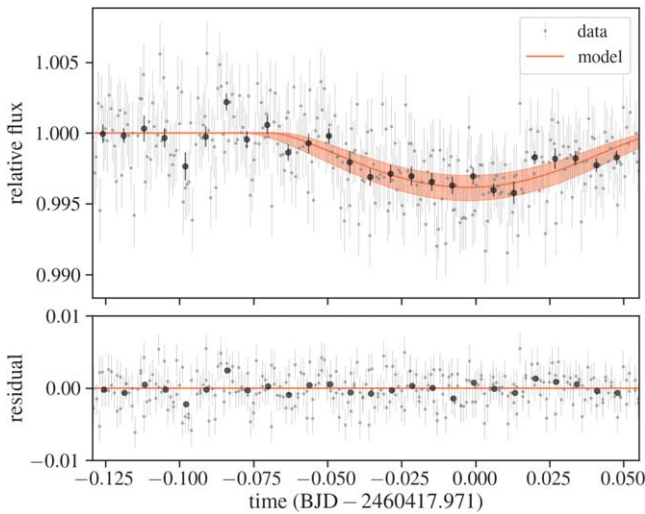


Figure 14. Full transit of Kepler-51c observed with WIRC on the Hale Telescope at Palomar Observatory. The larger black points represent 10-minute binned data, and the mean and standard deviation of the posterior models are plotted in red. Residuals are plotted in the bottom panels.

that the results were consistent despite the grazing transit configuration. First, we fixed the limb-darkening parameters u_1 and u_2 to 0.27 and 0.15, respectively, which are the predictions from `ldtk` (H. Parviainen & S. Aigrain 2015) in the J bandpass using the stellar effective temperature, metallicity, and surface gravity values from J. E. Libby-Roberts et al. (2020). Then, we ran the same model with free quadratic limb-darkening parameters. The posterior results were consistent across both cases, so we report the results from the model with free limb darkening here. We explore the parameter space with the NUTS sampler in `PyMC3` (J. Salvatier et al. 2016) and ensure that the chains have evolved until the Gelman–Rubin statistic (A. Gelman et al. 2014) values are < 1.01 for all parameters. We measure a transit time of $2,460,417.9711 \pm 0.0047$ BJD.

3.4.9. Other Attempts

We attempted to observe transits of Kepler-51b on UT 2020 July 25 with a 0.4m LCOGT telescope, and on UT 2020 September 8 with the Grand-Pra Observatory 0.4m and Wild Boar Remote Observatory 0.24m telescopes. The light curves from these observations yielded inconclusive transit detections owing to the faintness of the target star, poor seeing conditions, and/or limited in-transit coverage; we did not consider these data further in our analyses. These data are publicly available on the ExoFOP website.⁵⁷

3.5. TESS

The TESS photometry is analyzed using the `tgloc` package (T. Han & T. D. Brandt 2023). `tgloc` removes contamination from nearby stars in the full-frame images (FFIs) using locally fitted effective PSFs derived using Gaia DR3 as priors of star positions and magnitude. A 3×3 aperture is then applied to the decontaminated FFI to produce the `cal_aper_flux` light curve that we use in this work, which is also detrended with the biweight method from `wotan` (M. Hippke et al. 2019).

TESS observed Kepler-51 in six different sectors. The transits of Kepler-51b were caught in Sectors 14, 54, and 55 and Kepler-51d

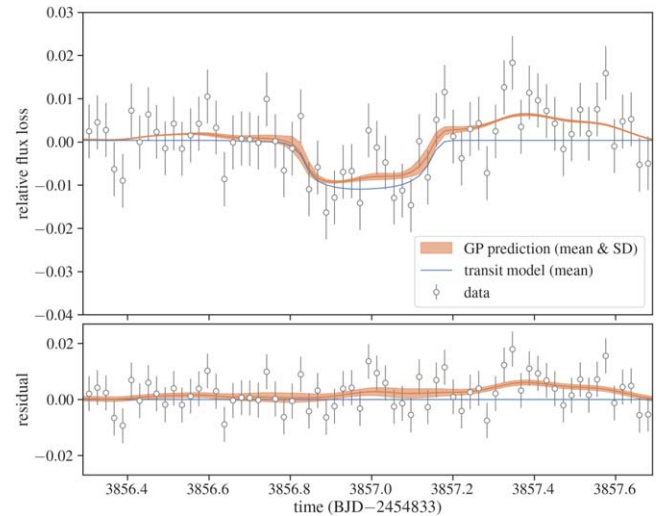


Figure 15. TESS Sector 14 transit of Kepler-51d. Top: the white circles with error bars show the relative flux loss. The orange line and shading show the mean and standard deviation of the predictions of the GP-included transit models computed from posterior samples. The blue line shows the mean of the transit models computed from posterior samples. Bottom: residuals of the fit relative to the mean transit model (blue line in the top panel).

in Sector 14. We first fit the Sector 14 data with a similar GP model to that described in Section 3.3, adopting the (truncated) normal priors in Table 3 and the priors on $u_1 + (u_2/2)$ and $u_1 - (u_2/2)$ derived from the Kepler data in a similar manner. For Kepler-51d, we obtained the transit time of $\text{BJD} - 2457000 = 1689.991^{+0.012}_{-0.021}$ (median and symmetric 68% interval of the marginal posterior),⁵⁸ which is consistent with the measurement by D. Jontof-Hutter et al. (2022). The former measurement is adopted in Table 1, and the light-curve data and model are shown in Figure 15. For Kepler-51b, we obtained $\text{BJD} - 2457000 = 1694.875^{+0.08}_{-0.02}$. This is again consistent with D. Jontof-Hutter et al. (2022), but the uncertainty we derived is larger (~ 100 minutes), as the planet’s shallower transit is not clearly distinguished from the correlated noise in our light-curve model. Since we are not confident in the accuracy of this timing measurement, we discard this transit of Kepler-51b from the subsequent TTV modeling, although adding this transit does not affect the result owing to its large uncertainty in any case. Similarly, we could not clearly identify the expected transits of Kepler-51b in Sectors 54 and 55, so they are not included in our timing analysis either.

4. Impact of Spot-crossing Events on Transit Time Measurements

The JWST transit light curve of Kepler-51d shows clear evidence of a spot-crossing event (Figure 1). The hints of similar events are also seen in the residuals of the Kepler transits of planets b and d (Figures 3 and 5).⁵⁹ It has been pointed out that such events, if unaccounted for, can introduce systematic errors in transit times up to a few minutes for transit parameters similar to Kepler-51b and d (e.g., S. C. C. Barros et al. 2013; M. Oshagh et al. 2013; T. Mazeh et al. 2015;

⁵⁸ We found a slightly bimodal marginal posterior for the transit time. This summary based on percentiles is associated with the higher mode by construction.

⁵⁹ This is a plausible explanation for a “bump” during the simultaneous transits of the two planets, as discussed in K. Masuda (2014) and T. A. Gordon & E. Agol (2022).

⁵⁷ <https://exofop.ipac.caltech.edu/tess/>

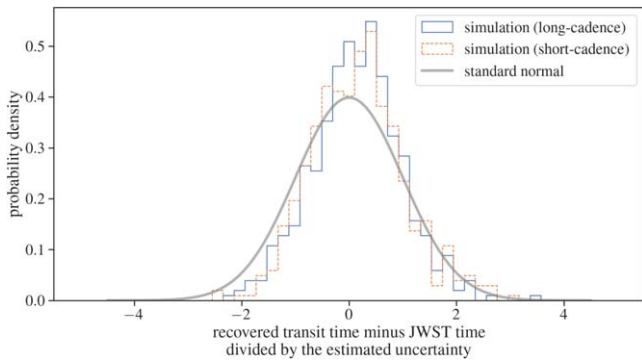


Figure 16. Results of injection-and-recovery tests for the timing bias using the simulated Kepler-like light curves including a spot-crossing event. The blue solid and orange dashed histograms show the distributions of the bias of the recovered transit times normalized by the estimated uncertainty. The gray solid line shows the standard normal distribution (a normal distribution with a mean of 0 and a variance of 1).

P. Ioannidis et al. 2016). In most of the timing measurements in Section 3, we explicitly modeled the correlated noise using a GP, and we expect that the impact of the wiggles caused by spot-crossing events is mitigated. That said, the GP model is not necessarily the correct model for the correlated noise introduced by such events, and so it is a priori unclear how accurate the resulting transit times and their uncertainties are.

This motivates us to explore the accuracy of our timing measurements using the JWST transit light curve as a “real template” of a transit including a significant spot-crossing event. Because the noise in the JWST data is much smaller and the cadence is much shorter than in the Kepler observations, the data can be used to simulate how this transit would have been observed by Kepler, by adding extra noise and then by appropriately downsampling the JWST light curve. We simulated 500 realizations of the Kepler long-cadence observations of this transit, changing the random seed for the extra white noise injected into the JWST data. Then, for each realization we performed the same analysis as described in Section 3.5 to obtain posterior samples for the midtransit time, derived their mean μ_{sim} and standard deviation σ_{sim} , and checked the distribution of $\delta = (\mu_{\text{sim}} - \mu_{\text{JWST}})/\sigma_{\text{sim}}$, where μ_{JWST} is the transit time derived in Section 3.1 incorporating the spot crossing in the model and is considered to be the ground truth in this simulation. If our timing estimate is not biased and its uncertainty is correctly estimated, δ would follow the standard normal distribution with the mean of zero and the standard deviation of unity. We found the mean and standard deviation of δ to be 0.14 and 0.83, respectively (blue solid line in Figure 16). This suggests that the bias is small, ~ 0.1 minutes for a typical timing error of ~ 1 minute, and that the estimated uncertainty is reasonably accurate, though it could be over-estimated by $\sim 10\%$. We repeated the same analysis simulating the Kepler short-cadence observations too (see orange dashed line) and found similar values (0.16 for the mean and 0.90 for the standard deviation). Of course, this result applies only to Kepler-51d and only for spot-crossing events near the middle of the transit just as observed by JWST, and the impact is likely larger for similar events happening in the ingress/egress. However, such events should be rarer by the fraction of the ingress/egress duration to the total transit duration. We have not simulated transit observations with other facilities either, but we suspect that other noise sources will be more dominant

in the lower signal-to-noise ratio light curves: the relative flux change due to the observed spot crossing ($\sim 10^{-3}$) is comparable to or smaller than the measurement errors in the ground-based light curves analyzed in Section 3.4. Thus, we do not believe that a majority of the measured transit times and their uncertainties are systematically in error owing to spot-crossing events that we did not explicitly model.

5. The TTV Model

We model the TTVs by numerically computing the transit times of the three transiting planets considering gravitational interactions between the planets and the star. The interaction was assumed to be Newtonian, and the light-travel time was ignored. The model parameters are the planet-to-star mass ratio m and the osculating orbital elements at the start of integration, here chosen to be $t_{\text{epoch}}(\text{BJD}_{\text{TDB}}) = 2454833 + 155$. These quantities are defined for each planet and are specified by the subscripts b, c, d, and e when necessary. The mass ratios (rather than masses) are adopted as fitting parameters because the TTVs (in which the light-travel time effect is not apparent) only constrain the mass ratios between the star and the planets. Throughout the paper we will frequently quote m in units of M_{\oplus}/M_{\odot} . This value will be the planet mass in units of Earth mass for a solar-mass host star, and the actual planet mass in units of M_{\oplus} is m multiplied by the stellar mass in units of M_{\odot} : if the stellar mass is $2M_{\odot}$, for example, the planet mass is $2m$ Earth masses. For Kepler-51 with $\approx 0.96M_{\odot}$ (see Section 2), the mass ratio quoted in this unit is close to the planet mass in units of M_{\oplus} . The osculating orbital elements are as follows: orbital period P , eccentricity e , argument of periastron ω , and time T of inferior conjunction nearest to the start of integration, which was converted to the time of periastron passage τ via $2\pi(T - \tau)/P = E_0 - e \sin E_0$, with $E_0 = 2 \arctan \left[\sqrt{\frac{1-e}{1+e}} \tan\left(\frac{\pi}{4} - \frac{\omega}{2}\right) \right]$.⁶⁰

We assume coplanarity and fix the orbital inclination i to be $\pi/2$ and the longitude of the ascending node Ω to be 0. We choose the sky plane to be the reference plane, and we adopt the $+Z$ -axis pointing toward the observer.⁶¹

The input masses and osculating orbital elements are converted to Jacobi coordinates. Here we use the total interior mass as the mass entering in the conversion from the orbital periods to coordinates, as in REBOUND (H. Rein & D. Tamayo 2015, see Section 2.2).⁶² We then perform an N -body integration using a symplectic integrator (J. Wisdom & M. Holman 1991; J. Wisdom 2006; K. M. Deck et al. 2014). The resulting orbits are used to derive midtransit times of each planet where the planet–star distance in the sky plane is minimized, following the iterative scheme described in D. C. Fabrycky (2010).⁶³ During this iteration, a fourth-order Hermite integrator

⁶⁰ Here $f = \pi/2 - \omega$ at inferior conjunction is converted to E via $\tan(E/2) = \sqrt{(1-e)/(1+e)} \tan(f/2)$. This is why the argument of arctan includes $\pi/4 - \omega/2$.

⁶¹ Some authors choose the opposite (e.g., E. Agol et al. 2021b), in which case the “ascending” node moves to the opposite side of the line of nodes and ω changes by π . Our choice is the same as that adopted in TTVFast (K. M. Deck et al. 2014).

⁶² We note that this convention is different from TTVFast. This results in the difference in the “orbital period” corresponding to the same position and velocity, and so appropriate conversion is needed to specify the same initial state using Jacobi elements. See also footnote 51 of F. Dai et al. (2023).

⁶³ The difference between the “transit times” computed this way and the times of inferior conjunctions as constrained in Section 3 is negligible for Kepler-51b, c, and d since their orbital periods are sufficiently long and eccentricities are sufficiently small (e.g., A. Hamann et al. 2019).

(E. Kokubo & J. Makino 2004) is used. The N -body code is implemented in `JAX` (J. Bradbury et al. 2018) to enable automatic differentiation with respect to the input mass ratios and orbital elements (see also E. Agol et al. 2021b) and is available through GitHub as a part of the `jnkepler` package;⁶⁴ see K. Masuda (2024, in preparation) for details of the implementation and F. Dai et al. (2023) for an application of the code. In this work, the time step of the symplectic integrator was fixed to be 1 day. For this step size and for typical system parameters as presented in Section 7, the fractional energy change during integration was $\sim 10^{-9}$, and the resulting transit times agreed with those computed using `TTVFast` (K. M. Deck et al. 2014) within ~ 1 s.

6. Evidence for a Fourth Planet

To validate the model in Section 5, we repeated the TTV analysis in J. E. Libby-Roberts et al. (2020) using the same timing data and including no planets other than the three transiting planets. We ran four HMC chains in parallel for 500 warm-up steps and for 1500 sampling steps (i.e., 6000 samples in total). We found split Gelman–Rubin statistics (A. Gelman et al. 2014) of <1.01 and effective number of samples >1000 for all parameters. The distribution of the posterior samples shows an excellent agreement with that in J. E. Libby-Roberts et al. (2020), as shown in Figure 25 in Appendix A. The mean and standard deviations of the marginal posteriors for the mass ratios are $m_b/M_*(M_\oplus/M_\odot) = 3.9 \pm 1.8$, $m_c/M_*(M_\oplus/M_\odot) = 4.5 \pm 0.5$, and $m_d/M_*(M_\oplus/M_\odot) = 5.8 \pm 1.1$; the 95% highest-density intervals (HDI) are [0.7, 7.3], [3.5, 5.5], and [3.7, 7.9] for planets b, c, and d, respectively.⁶⁵

In Figure 17, we show TTVs of the three transiting planets computed from the above three-planet fit (blue circles and shades). This model predicts that the midtransit time of Kepler-51d we aimed to observe with JWST should have been $\text{BJD} = 2,460,121.9304 \pm 0.0018$ (mean and standard deviation of the posterior distribution). However, the JWST transit of Kepler-51d (Section 3.1) happened earlier by 120 minutes compared to this prediction (which exhibits a 1σ uncertainty of 2.6 minutes), as shown in Figure 1 and by the star symbol in the bottom panel of Figure 17. We see evidence of a spot-crossing event in the light curve, but obviously it does not explain the offset, and the JWST timing measurement was also confirmed independently by the APO observation from the ground (Section 3.4.7). This indicates that the three-planet TTV model is incorrect.

The timing discrepancy was further supported by the HST observation of the subsequent transit of Kepler-51d (Section 3.2). The transit times from the ground-based facilities obtained before these measurements (Section 3.4) also show (smaller) deviations from the three-planet prediction. These data are shown in Figure 17 with squares and diamonds, respectively.⁶⁶ Thus, the data from different space- and ground-based observatories all show that the model involving only the three known transiting planets does not replicate the observed

TTVs. The simplest explanation is that there is a fourth planet in the system. We explore this scenario in Section 7.

6.1. Light-travel Time Effect

We modeled TTVs only, due to the physical variations of the orbits, and ignored the light-travel time effect associated with the reflex motion of the central star around the common center of mass. This is because the expected amplitude of this signal (E. Agol et al. 2005),

$$\delta t_{\text{LTTE}} = \frac{a M_p}{c M_*} \approx 0.5 \text{ s} \left(\frac{M_p/M_{\text{Jup}}}{M_*/M_\odot} \right) \left(\frac{a}{1 \text{ au}} \right), \quad (4)$$

is small for Kepler-51b, c, and d. This equation shows that a stellar-mass perturber on an au-scale orbit could generate a signal comparable to the excess TTVs of ~ 100 minutes observed for planet d. However, we do not consider this to be a plausible explanation, as the light-travel time effect should similarly impact Kepler-51b and c, for which such TTVs are not observed.

6.2. Three-planet Fit to All Timing Data

Above we demonstrated the discrepancy between the three-planet prediction based on the Kepler and previous HST data and the new timing measurement from JWST. This implies that both data sets cannot be consistently modeled. To check this, we also fitted all available transit times with a three-planet model, minimizing the χ^2 ,

$$\chi^2 = \sum_{i \in \text{all data}} \left(\frac{t_i - m_i}{\sigma_i} \right)^2, \quad (5)$$

using the Trust Region Reflective method implemented in `scipy.optimize.curve_fit`: here t_i and σ_i are the observed transit time and error (see the note in Table 1), m_i is the transit time from the N -body model, and the summation is over all transit times in Table 1. This optimization was repeated by fixing the mass ratio of each planet to be 1, 2, ..., $20 M_\oplus/M_\odot$; the search ranges for the other parameters are listed in Table 4. The best model we found is shown with the orange dashed lines in Figure 17, where the model for Kepler-51d now fits the JWST data with a small error but fails to explain the others. The model gives $\chi^2 \approx 2500$ for 70 data points, which again argues against the three-planet model.

6.3. Impact of Nonzero Mutual Orbital Inclinations

To explore the potential impact of nonzero mutual inclinations, we also performed a “photodynamical” modeling of the Kepler light curves, in which models of transit light curves were computed based on numerically integrated orbits and the mutual inclinations of the planetary orbits were allowed to vary; see Appendix C for details of the analysis setup and results. This modeling incorporates the information on the transit shapes and is therefore more sensitive to the mutual orbital inclinations than the analysis of TTVs alone. We found the inclinations of the orbits of Kepler-51b and Kepler-51c relative to that of Kepler-51d to be $0^\circ\text{--}13^\circ$ and $0^\circ\text{--}3^\circ$ (95% HDIs), and the mass ratios for all three transiting planets are consistent with the coplanar TTV modeling as described above. The TTV predictions

⁶⁴ <https://github.com/kemasuda/jnkepler>

⁶⁵ The value of ω for Kepler-51b reported in Table 10 of J. E. Libby-Roberts et al. (2020) is erroneously shifted by π . Posterior samples in their Table 9 are correct.

⁶⁶ On the other hand, the TESS transit time for Kepler-51d happened to be consistent with the three-planet model, as shown in the bottom panel. This explains the deviation from the three-planet model was not noted by D. Jontof-Hutter et al. (2022).

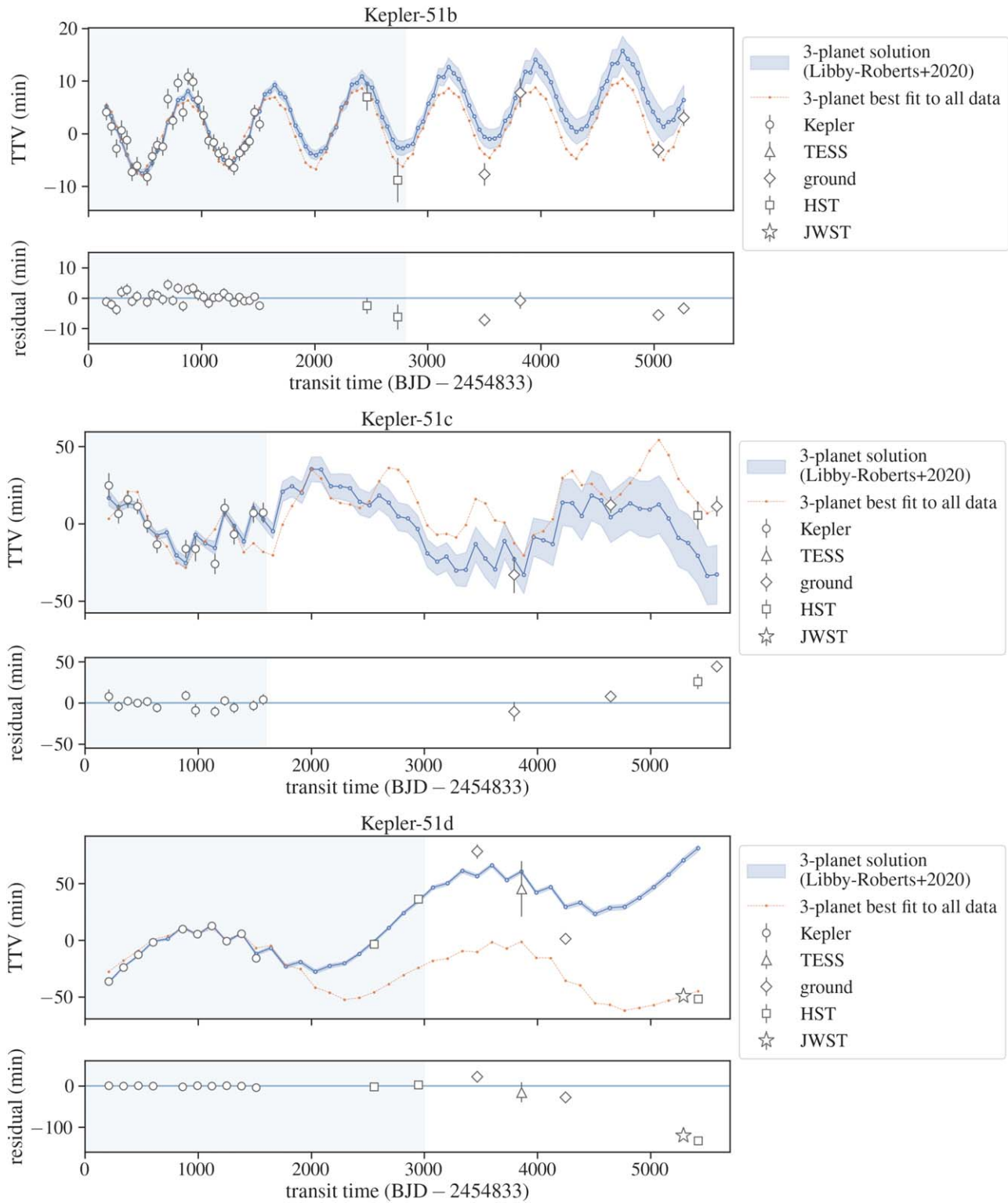


Figure 17. Comparison between the three-planet model prediction and all the timing data presented in this paper (Table 1). Here the TTVs in the vertical axes are shown with respect to the linear ephemerides given by t_0 (BJD $-2,454,833$) = 159.1068, 209.9946, and 212.0493 and P (days) = 45.155296, 85.316963, and 130.175183 for planets b, c, and d, respectively; note that the appearance of the plot depends on these arbitrary choices. The three-planet model based on the Kepler and HST data presented in J. E. Libby-Roberts et al. (2020) is shown with the blue circles (mean) and shading (standard deviation); the solution is *not* conditioned on the other data at time >3000 . The JWST data for Kepler-51d (star symbol in the bottom panel) were ≈ 2 hr off from the predicted transit time. The discrepancy was confirmed with the ground-based data (diamonds) and the later HST data (rightmost squares for Kepler-51c and d). The best three-planet model based on *all* transit times (Section 6.2) is shown with orange dashed lines.

extrapolated after Kepler observations also remained similar. Thus, the three-planet model fails to explain the data even considering nonzero mutual inclinations. This analysis also

suggests that the planetary masses from coplanar TTV models are largely unaffected by mutual orbital inclinations of $\lesssim 10^\circ$.

Table 4
Parameter Ranges of the Brute-force Searches in Section 7.1

	Search1 (Kepler-like, inside d)	Search2 (Kepler-like, outside d)	Search3 (Outer Giant)
	Fourth Planet		
Period P_c	[1.1 P_b , 1.7 P_b], $N = 50$ [1.1 P_c , 1.4 P_c], $N = 50$	[1.1 P_d , 5 P_d], $N = 100$	[5 P_d , 50 P_d], $N = 200$
Orbital phase $(T_e - T_{\text{epoch}})/P_c$	[0, 1], $N = 50$	[0, 1], $N = 50$	[0, 1], $N = 250$
$e \cos \omega$, $e \sin \omega$	[-0.1, 0.1], $N = 1$	[-0.2, 0.2], $N = 1$	[-0.7, 0.7], $N = 1$
Mass ratio m_c/M_*	[10^{-6} , 10^{-4}], $N = 1$	[3×10^{-7} , 3×10^{-4}], $N = 4$	[3×10^{-5} , 3×10^{-3}], $N = 2$
	Inner Three Transiting Planets		
Period P		[$P_0 - 0.1$, $P_0 + 0.1$], $N = 1$	
Orbital phase T		[$T_0 - 0.01$, $T_0 + 0.01$], $N = 1$	
$e \cos \omega$, $e \sin \omega$		[-0.1, 0.1], $N = 1$	
Mass ratio		[10^{-6} , 10^{-4}], $N = 1$	

Note. $[a, b]$ shows the edges of the bins, and N shows the number of bins between a and b ($N = 1$ means that the interval was not divided). We adopt log-uniform bins for the period and mass ratio and uniform bins for the orbital phase. For the inner transiting planets, P_0 and T_0 denote the linear ephemeris for each planet obtained by linear fitting to the transit times against the number of transits.

7. Four-planet TTV Modeling Assuming Coplanarity

Here we explore possible four-planet solutions to the observed TTVs and assess how adding this planet may or may not impact other planets' parameters, especially their masses. We find no clear evidence of transits of Kepler-51e in the Kepler data, leaving its orbital period and inclination unknown. Any planet outside Kepler-51b, whose semimajor axis is about 60 times larger than the stellar radius, will not transit the star from our perspective if its orbital inclination is less than $\arccos(1/60) = 89^\circ$. As such, the lack of transit detection is not informative and does not necessarily imply significant deviation from coplanarity (see also Section 8.4).

Deriving the mass and orbit of a planet without detected transits using TTV data alone has been possible only in a few cases where strong gravitational interactions and good data coverage enabled detection of TTV signals with multiple frequencies (e.g., D. Nesvorný et al. 2012). This is not the case here, as the TTV residuals of Kepler-51d only show a part of an excess long-term modulation, and we will assume that the orbital planes of the four planets are aligned in the following analyses. We expect that the mass constraints will not change significantly for deviations of $\lesssim 10^\circ$ from perfect coplanarity (see also Section 6.3), but other qualitatively different solutions involving larger mutual inclinations for Kepler-51e could exist. That said, the assumption of near coplanarity is not without foundation: the mutual inclinations of the orbits of nontransiting planets in systems with multiple transiting planets have been inferred to be small ($\lesssim 10^\circ$) in general, for those that are both near and far from the transiting planets (W. Zhu et al. 2018; K. Masuda et al. 2020).

7.1. Brute-force Search for the Solutions

TTV inversions involving a nontransiting planet typically result in multiple solutions with different orbital periods and phases for the nontransiting planet (e.g., S. E. Jones et al. 2024; J. M. Almenara et al. 2024). This motivates us to perform a brute-force search over a “grid” of orbital periods and phases for Kepler-51e.

7.1.1. Grid Optimization and Stability Analysis

We set up bins in the parameter space as shown in Table 4 and performed bounded optimization in each of the $100 \times 50 \times 1$ (Search1), $100 \times 50 \times 4$ (Search2), and $200 \times 250 \times 2$ (Search3) bins minimizing the χ^2 in Equation (5). Search1 and Search2 are to probe “Kepler-like” systems where the fourth planet is near the inner three and its orbit has a modest eccentricity. The fourth planet is assumed to be inside and outside of Kepler-51d's orbit in Search1 and Search2, respectively. Here the lower boundary of the period ratio (1.1) is smaller than the period ratios of known Kepler planets in multitransiting systems (J. N. Winn & D. C. Fabrycky 2015), and the corresponding orbits are likely dynamically unstable (B. Pu & Y. Wu 2015; see also below). For Search2, the upper bounds of $|e \cos \omega|$ and $|e \sin \omega|$ were set to 0.2 for most parameter combinations, but they were truncated for small P_c/P_d so that the orbits do not cross. Search3 is to explore another common situation where (not-so-metal-poor) stars with Kepler-like planets have an outer giant planet whose orbit is not necessarily circular (W. Zhu & Y. Wu 2018; M. L. Bryan et al. 2019).

Search1, Search2, and Search3 result in optimal solutions in each of the $100 \times 50 \times 1 = 5000$, $100 \times 50 \times 4 = 20,000$, and $200 \times 250 \times 2 = 100,000$ bins, respectively. For those that give reasonably good fits (see below), we used FeatureClassifier in the SPOCK (D. Tamayo et al. 2020) software to compute the probability that the system is stable over 10^9 orbits, which is comparable to our rough age estimate of ~ 0.7 Gyr (Section 2).

7.1.2. Results

Figure 18 shows a subset of the optimal solutions from the brute-force search in the period–mass–eccentricity plane of planet e. The color of each point corresponds to the value of χ^2 , and the solutions for which the stability probability computed with SPOCK is less than 50% are shown with crosses. Here we show the solutions with $\chi^2 < 82$, which corresponds to a p -value of $\approx 0.3\%$ for 50 degrees of freedom, i.e., 70 (number of data points) minus 20 (number of fitted parameters). We set a rather generous threshold because the effective number of degrees of freedom in this nonlinear problem may be larger than calculated above (R. Andrae et al. 2010). Indeed, we

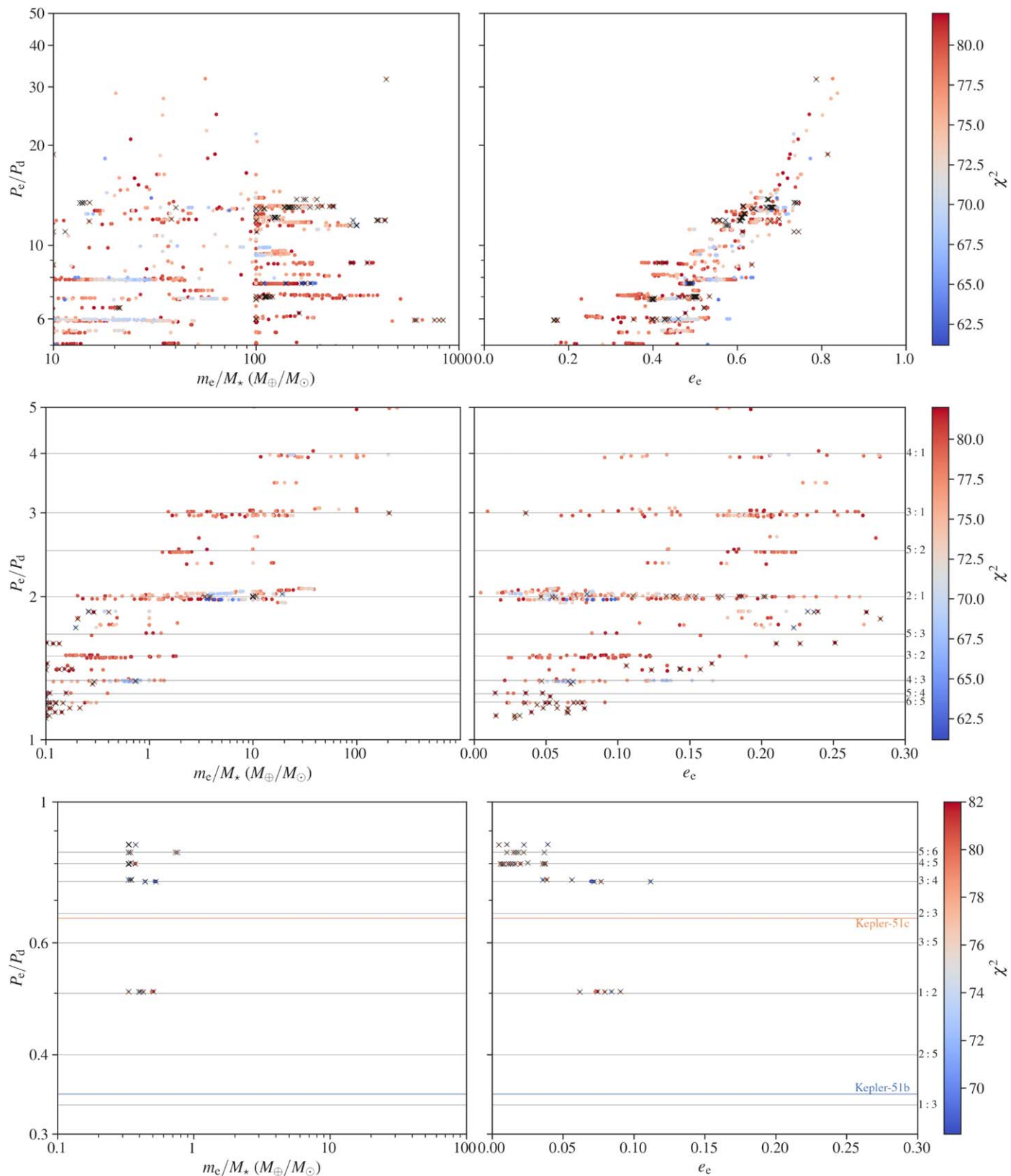


Figure 18. Results of the brute-force search and stability analysis for Search3 (top), Search2 (middle), and Search1 (bottom) in Table 4. Note the different scales of the x -axes. The colored points show the period ratio of planet e and planet d against the mass ratio (left column) and orbital eccentricity (right column) of planet e. Their colors correspond to the χ^2 values shown in the right color bar. The crosses show the solutions for which the probability that the system is long-term stable is lower than 50% (see Section 7.1).

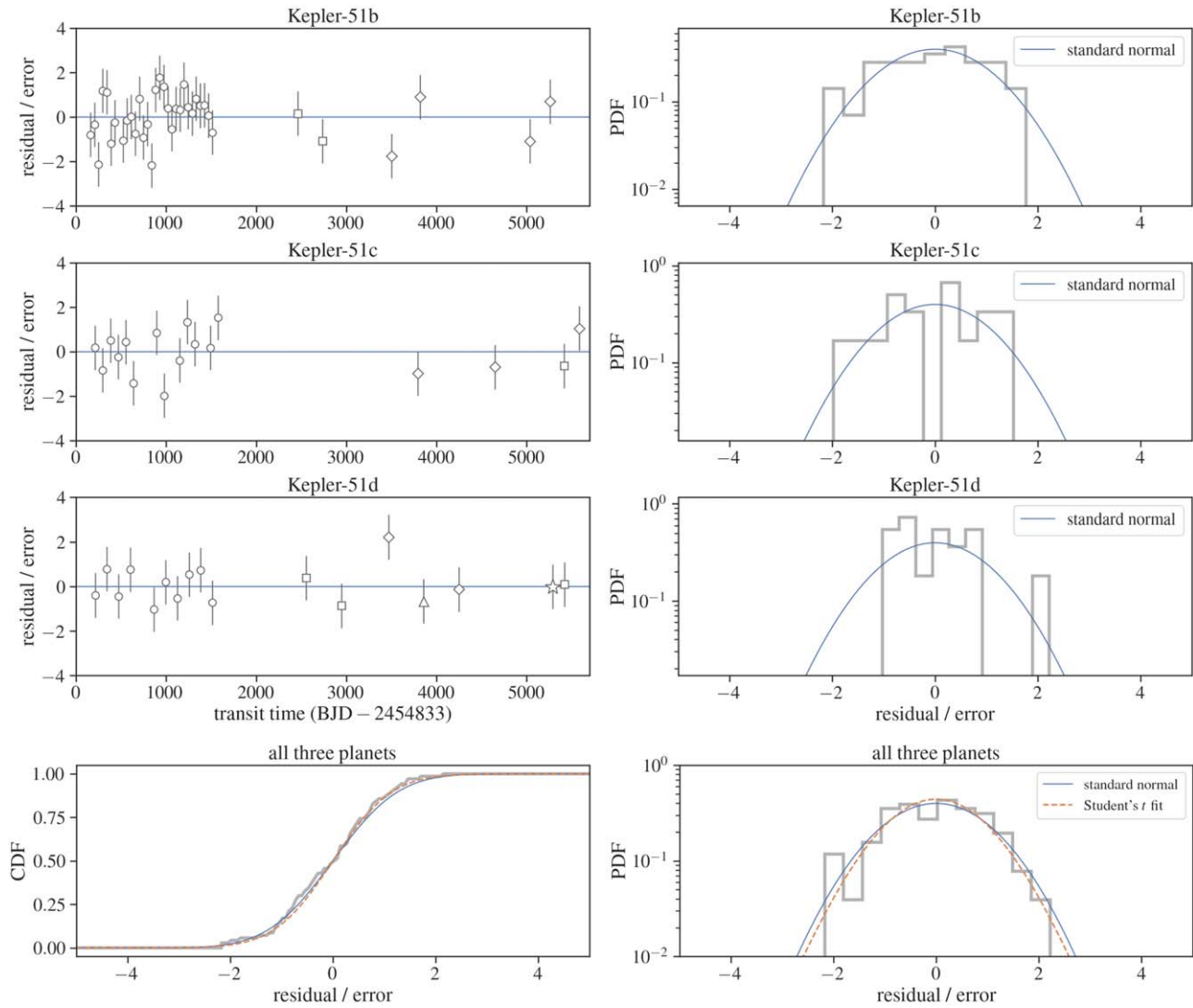


Figure 19. Normalized fitting residuals vs. time (top three panels on the left) and their distributions (the other panels) for the best 2:1 solution found from the brute-force search described in Section 7.1. The length of the error bars is unity for all points by construction. In the residuals vs. time plots, the symbols represent observations as in Figure 17. In the distribution plots, the (cumulative) distributions of the normalized residuals are shown with the thick gray lines. The blue solid lines show the standard normal distribution. The orange dashed lines in the bottom two panels show the Student’s *t* distribution fitted to the normalized residuals (see Section 7.1.2).

performed a Kolmogorov–Smirnov test for the null hypothesis that the distribution of the fitting residuals normalized by the assigned errors is drawn from the standard normal distribution, and we found *p*-values larger than 0.1 for all of these solutions with $\chi^2 < 82$. Thus, none of these solutions are completely excluded by the available data, although the solutions in which planet e is inside Kepler-51d (Search1; bottom panels) generally seem disfavored from a stability point of view. The list of parameters corresponding to these solutions is available through the author’s GitHub.⁶⁷ The minimum χ^2 value of ≈ 61 was found for $P_e/P_d \approx 2$ (Search2) and $P_e/P_d \approx 8$ (Search3).

In Figure 19, we show the distribution of the normalized residuals (i.e., residuals divided by the assigned errors) for the minimum χ^2 solution around $P_e/P_d = 2$ as an example. The TTV models corresponding to this class of solutions are shown in Figure 22 (see also Section 7.3). As stated above, we see no clear evidence that the normalized residuals deviate from the

standard normal distribution. This is consistent with our assessment of the accuracy of timing errors in Section 4. We also fit the normalized residuals with a Student’s *t* distribution to estimate the number of degrees of freedom, ν , and the scale of the distribution squared, V_1 , considering that more heavy-tailed residual distributions have been reported in previous transit timing analyses (e.g., D. Jontof-Hutter et al. 2016; E. Agol et al. 2021a). We find $\ln \nu = 3.3 \pm 0.9$ (or $\nu \approx 27$) and $\ln V_1 \approx -0.21 \pm 0.22$, which support the consistency with the standard normal distribution (see orange dashed lines in the bottom panels of Figure 19).

In short, we have found that the four-planet model works well to explain the observed TTVs. However, the property of the fourth planet remains unconstrained by the available data: it could be either a relatively low mass planet on a near-circular orbit outside of and close to Kepler-51d or a relatively massive planet on a distant, eccentric orbit. A general tendency, as shown in Figure 18, is that the required mass and eccentricity of the fourth planet increase as the period ratio P_e/P_d increases. More timing data are needed to pin down the properties of

⁶⁷ https://github.com/kemasuda/kep51_jwst

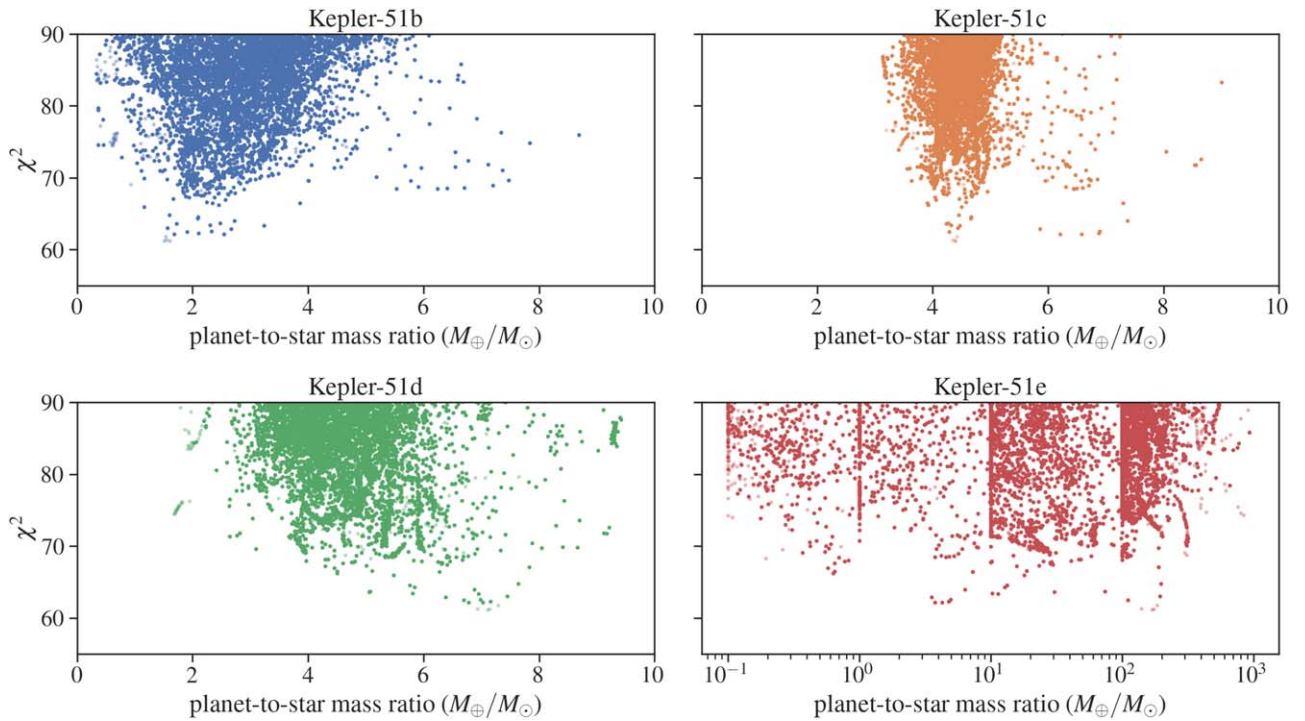


Figure 20. Mass ratios of the four planets from the brute-force search. Note the different axis scale in the bottom right panel for planet e; the vertical stripes correspond to the edges of the mass grids (see Table 4). This plot shows only the best masses corresponding to each set of the fourth planet’s parameters (but see also Figure 21).

Kepler-51e. They will also be important to better characterize the noise distribution including its tails. While we see no clear evidence for the non-Gaussianity in the current timing residuals, if more timing data reveal that it is more appropriate to treat part of the data as outliers, the parameter estimates and their uncertainties may be quantitatively affected.

In contrast, we found that all of these solutions consistently imply mass ratios $\lesssim 10 M_{\oplus}/M_{\odot}$ for the inner three transiting planets (Figure 20). The values are comparable to those found from the previous three-planet model (see Section 6). We interpret this result as a reasonable consequence of the fact that the masses of planets c and d are mainly determined by the chopping signal in the TTVs of planets d and c from Kepler, respectively, and that the mass of planet b is constrained by the absence of its gravitational impact on the TTVs of planet c. The amplitude of the chopping signal is mainly determined by the mass ratios and the period ratios of the planets (K. M. Deck & E. Agol 2015), the latter of which does not change much by adding a fourth planet.

That said, Figure 20 shows only the best-fit masses for given properties of the fourth planet, and the above searches do not quantify the uncertainty of the inner planets’ masses associated with each given set of the fourth planet’s parameters. For example, if the planet mass were constrained to be $10 \pm 5 M_{\oplus}$ (with $10 M_{\oplus}$ giving the highest likelihood values) for all possible values of P_e , Figure 20 would have shown points only at $10 M_{\oplus}$ without conveying any information about the $5 M_{\oplus}$ uncertainty. More generally, the above searches could have missed solutions with larger masses for the inner planets that are qualitatively different from the three-planet solutions, given that the search involves nonlinear optimization in a high-dimensional parameter space. We thus further explore the constraints on the masses of the inner three transiting planets in the next subsection.

7.2. Constraints on the Mass Ratios of the Inner Three Transiting Planets

Here we attempt to quantify the uncertainties of the mass ratios of the inner three transiting planets by evaluating the profile likelihood for these parameters. For each of planets b, c, and d, we fix the mass ratio to be 1, 2, 3, ..., $15 M_{\oplus}/M_{\odot}$; perform the brute-force search as described in the previous subsection for each fixed mass ratio; and determine the minimum value of χ^2 as a function of the fixed mass ratio after optimizing all other parameters. To save computational time, we limited the search range of P_e/P_d around the values for which good solutions were found (see Figure 18). The search ranges for the other parameters are the same as in Table 4.

The results are shown in Figure 21 for the period ratios of $P_e/P_d \approx 4/3, 3/2, 5/3, 2/1, 5/2, 3/1, 4/1, 6/1,$ and $8/1$. For the 2:1 ratio, solutions with $P_e/P_d < 2$ (in) and $P_e/P_d > 2$ (out) are shown separately (see also Section 7.3). For the period ratios examined here, we confirm that the best-fit mass ratios for planets b–d are low, as in Figure 20, and also that the models involving larger mass ratios do yield poorer fits to the data and lower likelihood values. Quantitatively, the largest mass ratios are allowed for either 2:1 (in) or 2:1 (out) solutions depending on the planet. In these cases, the ranges of mass ratios corresponding to $\Delta\chi^2 < 4$ are $< 13 M_{\oplus}/M_{\odot}$ for Kepler-51b (2:1 out), $4.5\text{--}8.1 M_{\oplus}/M_{\odot}$ for Kepler-51c (2:1 in), and $3.8\text{--}9.2 M_{\oplus}/M_{\odot}$ for Kepler-51d (2:1 out). This analysis therefore further supports the conclusion that the inner three transiting planets have masses $\lesssim 10 M_{\oplus}$ (given $M_{\star} \approx 0.96 M_{\odot}$; Section 2) regardless of the properties of the fourth planet, although the mass uncertainties in the four-planet model have become larger than estimated from three-planet models (J. E. Libby-Roberts et al. 2020).

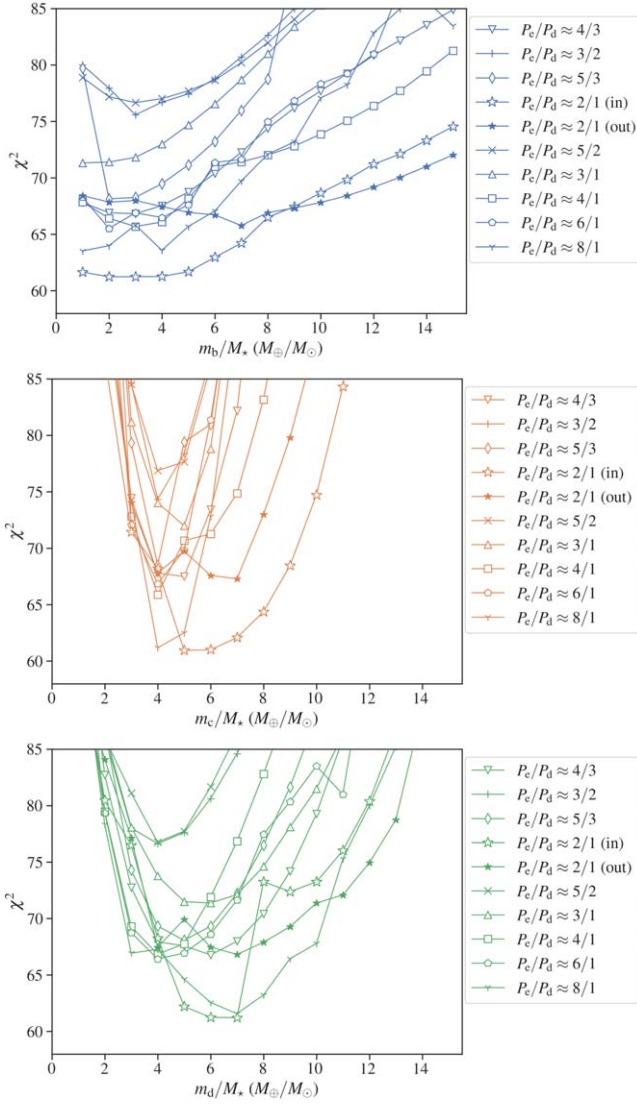


Figure 21. The minimum χ^2 values as a function of the mass ratio of planets b (top), c (middle), and d (bottom), for selected orbital periods of planet e shown on the right.

7.3. Posterior Sampling for the 2:1 Solution

We further examine the mass constraints from Section 7.2 with a Markov Chain Monte Carlo analysis. Since it is not computationally feasible to perform the analysis for all possible period ratios, here we focus on the 2:1 solution, which yields the largest mass upper limit for planet b among the solutions searched (Figure 21). Such a solution deserves attention in light of the puzzlingly low inferred densities of the Kepler-51 planets, as it can accommodate higher densities. Therefore, it is useful to examine the accuracy of the mass limits for this solution with an independent analysis.

There are several additional properties of the 2:1 solution that are worth noting. First, this is one of the best solutions in terms of the χ^2 values (Figure 21). Second, at this period ratio the largest number of “good” solutions are found among the T_4 bins, i.e., the points in the middle panels of Figure 18 are the most densely clustered around this period ratio. This solution is therefore less fine-tuned in terms of the unknown orbital phase of planet e than the others. Third, the 2:1 solution favors $e_e \lesssim 0.1$ and $m_e/M_* \sim 1\text{--}10 M_{\oplus}$, as shown in the middle panels of Figure 18,

Table 5

The Prior pdf’s Adopted When Sampling from the Posterior Distributions for the 2:1 Solutions in Section 7.3

Parameter	Prior
Inner Three Transiting Planets	
Planet-to-star mass ratio	$\mathcal{U}(0, 5 \times 10^{-4})$
Orbital period (days)	$\mathcal{U}(P_0 - 0.05, P_0 + 0.05)$
Orbital eccentricity	$\mathcal{U}(0, 0.2)$
Argument of periastron	$\mathcal{U}(0, 2\pi)^a$
Time of inferior conjunction (days)	$\mathcal{U}(T_0 - 0.05, T_0 + 0.05)$
Kepler-51e	
Planet-to-star mass ratio	$\mathcal{U}(0, 5 \times 10^{-4})$
Orbital period (days)	$\mathcal{U}(250.35, 260.35)$ (inside) or $\mathcal{U}(260.35, 270.35)$ (outside)
Orbital eccentricity	$\mathcal{U}(0, 0.2)$
Argument of periastron	$\mathcal{U}(0, 2\pi)^a$
Time of inferior conjunction	$\mathcal{U}(200, 400)$
(BJD $-2,454,833$)	

Notes. $\mathcal{U}(a, b)$ denotes the uniform distribution between a and b . $\mathcal{LU}(a, b)$ denotes the log-uniform distribution between a and b . The symbols P_0 and T_0 denote the linear ephemeris computed from the observed transit times for each planet.

^a These parameters were treated as angles, and the distributions were wrapped at the edges.

and this is essentially the only solution from the brute-force search that satisfies both. The inferred low eccentricity is reminiscent of planets in the compact multitransiting systems from Kepler (S. Hadden & Y. Lithwick 2014; V. Van Eylen & S. Albrecht 2015), while the inferred mass range is comparable to the masses of the inner three transiting planets (as will be further quantified below). Mass uniformity has been suggested for other known compact multiplanet systems (S. Millholland et al. 2017). The 2:1 period ratio is also fairly common among Kepler multiplanet systems (J. N. Winn & D. C. Fabrycky 2015). Thus, the properties of Kepler-51e from the 2:1 solution appear to be a priori plausible, although it is difficult to quantify the plausibility relative to the other solutions. This provides further motivation to examine this solution in detail.

We draw samples from the joint posterior pdf for the set of system parameters θ conditioned on the timing data d :

$$p(\theta|d) = \frac{p(d|\theta)p(\theta)}{p(d)}. \quad (6)$$

The parameter θ consists of the mass ratios and orbital elements of the four planets (see Section 5). Here we adopt the likelihood function given by

$$\ln p(\theta|d) = -\frac{1}{2} \sum_{i \in \text{all data}} \left[\frac{(t_i - m_i)^2}{\sigma_i^2} + \ln(2\pi\sigma_i^2) \right]. \quad (7)$$

The prior pdf $p(\theta)$ is assumed to be separable for each model parameter, as summarized in Table 5. Because we found it difficult to sample simultaneously from solutions inside (i.e., $P_e/P_d < 2$) and outside ($P_e/P_d > 2$) the 2:1 resonance owing to the presence of a low-likelihood region near $P_e/P_d = 2$ (see the middle left panel of Figure 18), we split the prior for P_e at $2P_d$ and sampled separately. The sampling was performed using NUTS (S. Duane et al. 1987; M. Betancourt 2017) as implemented in NumPyro (E. Bingham et al. 2018; D. Phan et al. 2019), turning on the dense mass matrix option that adjusts the nondiagonal

Table 6
Planetary and Orbital Parameters of the 2:1 Solution Computed from the Posterior Samples Obtained in Section 7.3

	Outside 2:1			Inside 2:1		
	Mean	SD	95% HDI	Mean	SD	95% HDI
Kepler-51b						
Mass ratio $m (M_{\oplus}/M_{\odot})$	6.9	2.9	[1.53, 12.84]	3.7	2.2	[0.0, 7.6]
Time of inferior conjunction (BKJD)	159.11087	0.00039	[159.1101, 159.1116]	159.11053	0.00047	[159.1096, 159.1114]
Orbital period P (days)	45.15396	0.00022	[45.15350, 45.15436]	45.15405	0.00039	[45.1532, 45.1548]
Eccentricity e	0.0162	0.0038	[0.009, 0.024]	0.026	0.010	[0.007, 0.046]
$e \cos \omega$	-0.0156	0.0038	[-0.023, -0.008]	-0.0114	0.0048	[-0.021, -0.002]
$e \sin \omega$	-0.0012	0.0044	[-0.010, 0.007]	-0.022	0.011	[-0.045, -0.002]
Mass (M_{\oplus})	6.7	2.8	[1.39, 12.22]	3.5	2.1	[0.1, 7.3]
Radius (R_{\oplus})	6.83	0.13	[6.57, 7.08]	6.83	0.13	[6.57, 7.08]
Density (g cm^{-3})	0.115	0.048	[0.02, 0.21]	0.060	0.037	[0.00, 0.13]
Kepler-51c						
Mass ratio $m (M_{\oplus}/M_{\odot})$	6.34	0.40	[5.5, 7.1]	5.89	0.83	[4.4, 7.5]
Time of inferior conjunction (BKJD)	210.0049	0.0025	[209.9999, 210.0097]	210.0078	0.0029	[210.002, 210.013]
Orbital period P (days)	85.3147	0.0018	[85.3111, 85.3182]	85.3139	0.0020	[85.3103, 85.3180]
Eccentricity e	0.0093	0.0077	[0.000, 0.026]	0.063	0.020	[0.021, 0.104]
$e \cos \omega$	0.0073	0.0077	[-0.003, 0.026]	0.029	0.014	[0.001, 0.054]
$e \sin \omega$	-0.00073	0.00575	[-0.012, 0.013]	-0.054	0.019	[-0.094, -0.016]
Mass (M_{\oplus})	6.09	0.41	[5.3, 6.9]	5.65	0.81	[4.1, 7.2]
Radius (R_{\oplus})	6.4	1.4	[4.5, 8.9]	6.4	1.4	[4.5, 8.9]
Density (g cm^{-3})	0.151	0.068	[0.03, 0.28]	0.140	0.066	[0.02, 0.27]
Kepler-51d						
Mass ratio $m (M_{\oplus}/M_{\odot})$	6.9	1.1	[4.9, 9.1]	5.9	1.3	[3.4, 8.4]
Time of inferior conjunction (BKJD)	212.0223	0.0017	[212.0194, 212.0258]	212.02524	0.00081	[212.0237, 212.0269]
Orbital period P (days)	130.1858	0.0018	[130.1824, 130.1891]	130.1820	0.0024	[130.1776, 130.1868]
Eccentricity e	0.0061	0.0056	[0.000, 0.018]	0.048	0.016	[0.013, 0.080]
$e \cos \omega$	0.0027	0.0062	[-0.006, 0.018]	0.020	0.011	[-0.001, 0.041]
$e \sin \omega$	0.00099	0.00467	[-0.008, 0.012]	-0.042	0.016	[-0.076, -0.012]
Mass (M_{\oplus})	6.6	1.0	[4.7, 8.7]	5.6	1.2	[3.4, 8.2]
Radius (R_{\oplus})	9.32	0.18	[8.98, 9.66]	9.32	0.18	[8.98, 9.66]
Density (g cm^{-3})	0.0448	0.0071	[0.031, 0.059]	0.0381	0.0085	[0.022, 0.055]
Kepler-51e						
Mass ratio $m (M_{\oplus}/M_{\odot})$	5.6	1.6	[2.6, 8.5]	3.9	1.3	[1.8, 6.5]
Time of inferior conjunction (BKJD)	262.508	11.445	[240.75, 283.64]	285.174	9.210	[266.89, 302.55]
Orbital period P (days)	264.284	0.905	[262.5, 265.9]	256.860	0.631	[255.8, 258.2]
Eccentricity e	0.020	0.015	[0.000, 0.048]	0.080	0.032	[0.01, 0.13]
$e \cos \omega$	-0.011	0.015	[-0.044, 0.015]	0.023	0.019	[-0.010, 0.060]
$e \sin \omega$	-0.0068	0.0148	[-0.040, 0.020]	-0.074	0.032	[-0.13, 0.00]
Mass (M_{\oplus})	5.4	1.5	[2.5, 8.1]	3.8	1.3	[1.6, 6.1]

Note. The values and uncertainties shown in this table are derived assuming that Kepler-51e is near the 2:1 resonance with Kepler-51d; other orbital periods are not excluded by the data, and the mass of Kepler-51e varies from $\sim 0.1 M_{\oplus}$ to $\sim M_{\text{Jup}}$ depending on the value of the correct period. As indicated by the HDI (within which every point has a higher probability density than any point outside it), we do not find a very stringent lower bound on the mass of Kepler-51b. This upper limit is also sensitive to the period of Kepler-51e. Among the solutions we found, the “outside 2:1” case shown here provides the largest upper limit and may be considered most conservative. The masses of Kepler-51c and d are more robustly determined and remain within $\sim 2\sigma$ regardless of the period of Kepler-51e. BKJD refers to BJD $-2,454,833$.

elements of the mass matrix in addition to the diagonal ones. We ran four independent chains in parallel for 2000 steps, after which we found the effective number of samples n_{eff} to be a few hundred to a few thousand and the split Gelman–Rubin statistic \hat{R} to be 1.00–1.04 for each parameter (A. Gelman et al. 2014).

Our results are summarized in Table 6, which also includes the absolute masses of the four planets and the radii and mean densities of the three transiting planets, computed using the posterior samples for the mass ratios from the TTVs, the posterior samples for the radius ratios from the Kepler long-cadence light curves (Section 3.3), and the stellar mass and radius from Section 2. As mentioned in Section 5, the planetary masses in units of M_{\oplus} are mostly the mass ratios in units of M_{\oplus}/M_{\odot} , but their uncertainties include that of the stellar mass and are therefore larger. The full posterior samples for each

solution are available through the author’s GitHub (see footnote 69). The corresponding TTV models and corner plot are shown in Figures 22 and 26, respectively.

The 95% HDIs for the mass ratios are comparable to those from the χ^2 analysis in Section 7.2 and Figure 21 and confirm those mass constraints from a Bayesian point of view. We note that exact agreement is not necessarily expected because the two constraints have different meanings even for the uniform priors on the mass ratios adopted here. Figure 21 shows the *projection* of the (negative log) likelihood profiles onto the mass ratio axes, while Figure 23 shows the probability distributions for the mass ratios after *integrating* over the other parameters. Thus, the latter, in principle, depends on how the mass ratios are degenerate with the other parameters, as well as on the prior pdf’s assumed for all the model parameters. The two constraints could therefore differ

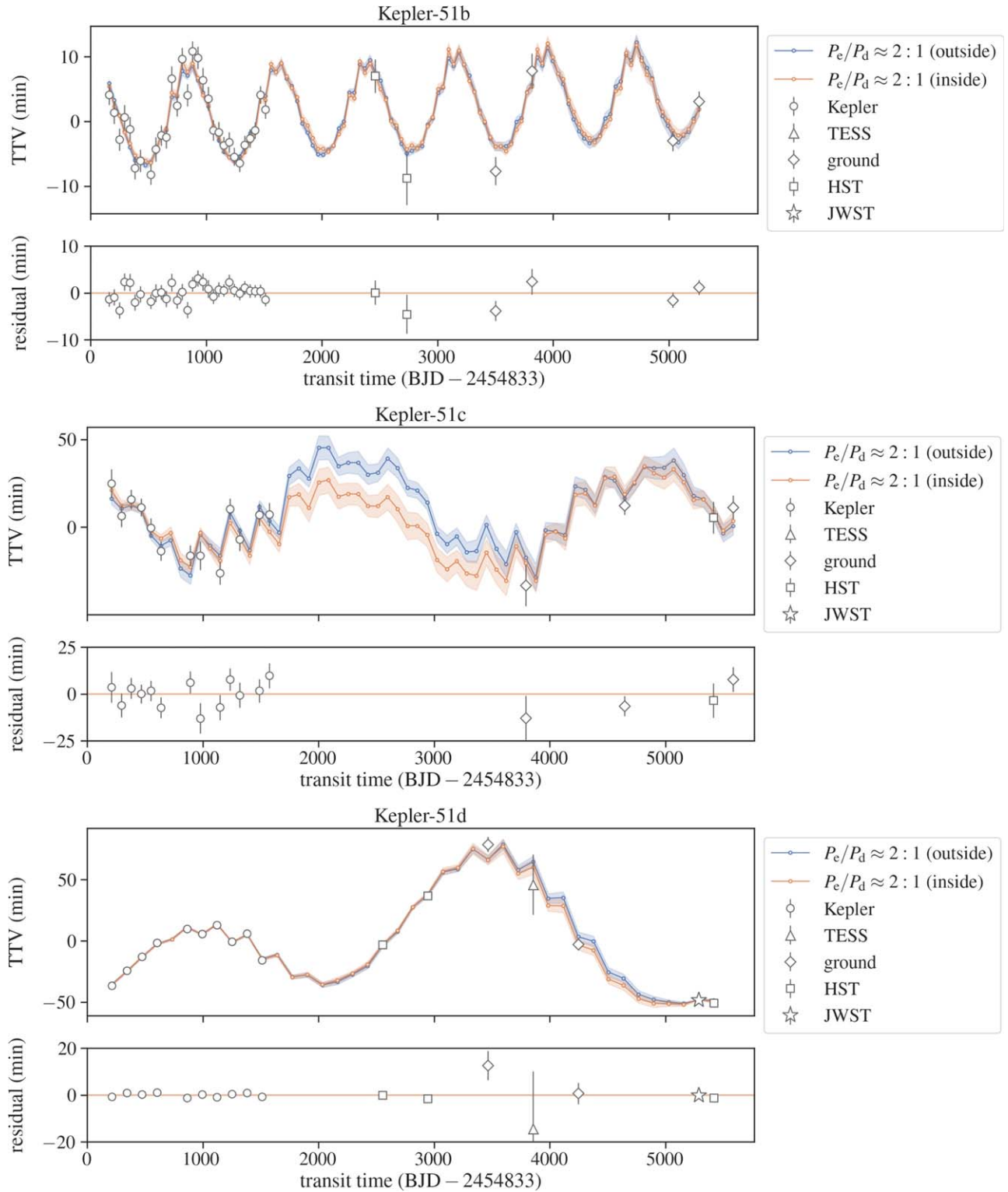


Figure 22. Comparison between the solutions in which Kepler-51e is around the 2:1 resonance with Kepler-51d and all the timing data presented in this paper (Table 1). Here the TTVs in the vertical axes are shown with respect to the linear ephemerides given by t_0 (BJD $-2,454,833$) = 159.1068, 209.9946, and 212.0493 and P (days) = 45.155296, 85.316963, and 130.175183 for planets b, c, and d, respectively; note that the appearance of the plot depends on these arbitrary choices. The solid line and the shaded region show the mean and standard deviation, respectively, of the TTV models at each time computed for the posterior samples obtained in Section 7.3.

significantly if the posterior distribution is sensitive to the prior. This does not appear to be the case here.

As shown in Figure 23, the mass of planet e is inferred to be $\approx 5 M_{\oplus}$ for solutions both outside and inside the 2:1 period ratio, consistent with the masses of the three transiting planets within the

uncertainties. The latter masses did not change drastically from the previous three-planet model (bottom row of Figure 23), although the mass ratio posterior for Kepler-51c shifted upward by $\sim 1 M_{\oplus}/M_{\odot}$. This is likely due to the fact that Kepler-51d's TTVs now include contributions from both Kepler-51c and e.

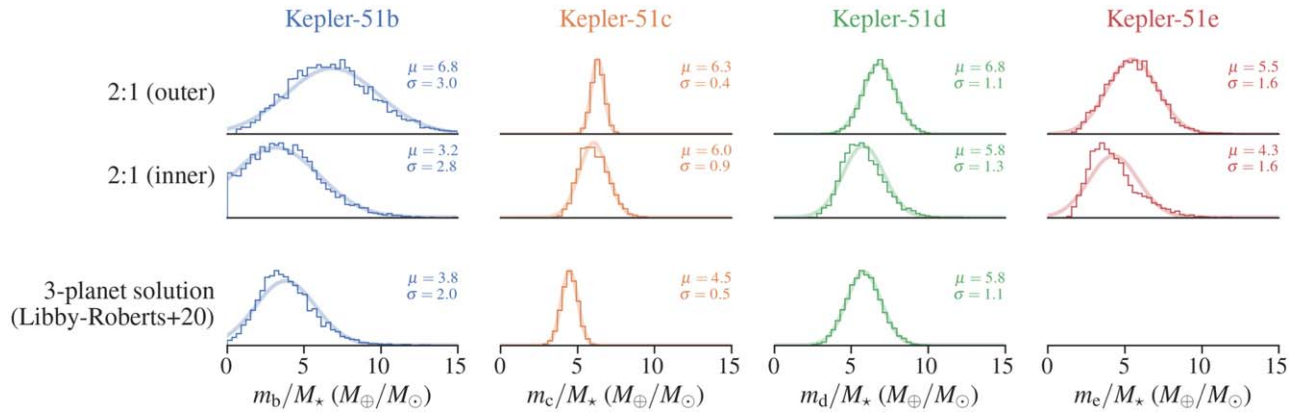


Figure 23. Comparison of the mass ratio posteriors from the four-planet model assuming the nearly 2:1 period ratio for the outermost pair (top two rows) and from the previous three-planet model (bottom row). The thick solid lines show the truncated normal distributions with lower bounds of zero fitted to the posterior samples, whose location (μ) and scale (σ) parameters are given in each panel. These values agree with the means and standard deviation of the posteriors for planets c and d but not those for planet b because the distribution is truncated at zero. As discussed in Section 7, the TTV data do not exclude other solutions with different orbital periods for planet e, in which the masses of the inner three planets vary only slightly, while that of Kepler-51e can vary by orders of magnitudes (see Figures 18 and 20–21 and the discussion in Sections 7.1.2–7.2).

8. Discussion

8.1. Prospects of Determining the Properties of Kepler-51e with Future TTVs

We showed that all observed TTVs, including the discrepant JWST data, can be accounted for with a wide range of masses and orbital periods for Kepler-51e. In other words, the properties of Kepler-51e are not well constrained with the available timing data. What observations could remedy this situation?

We used the solutions found from the brute-force search (Section 7.1) and the posterior samples for the 2:1 solution (Section 7.3) to predict future TTVs of the three transiting planets. The blue and orange lines and shaded areas in Figure 24 show the mean and standard deviation of the posterior models computed for the solutions outside and inside 2:1, respectively. As we discussed in Section 7.1, these solutions are not the only ones allowed by the data, but here we show them as an example to illustrate the prediction uncertainty associated with a solution with a given period for planet e. In contrast, the gray dashed lines show the same interval (one standard deviation around the mean) for all the solutions in Figure 18 found from the brute-force search, which involve a wide range of orbital periods for planet e. This interval does not possess a statistically well-defined interpretation, but here we show it to illustrate the degree of scatter of all possible solutions. These predicted transit times are given in Table 7 in Appendix B.

As exemplified by the blue and orange curves for planets c and d, the high-probability regions differ for each solution. At the same time, there is overlap in the prediction ranges at a given epoch: the areas shaded in orange and blue overlap with, or fall between, the two gray dashed lines. Therefore, a single timing measurement or just a few will not be able to completely single out a specific solution. Instead, continuous measurements of transit times that constrain the shape of the TTV curve will be necessary to distinguish different solutions. These follow-up observations will be particularly informative for planets c and d, for which predictions made by different solutions exhibit a larger dispersion than for b. However, we also emphasize the importance of monitoring planet b to continuously verify the accuracy of the four-planet model, considering how the presence of planet e was revealed.

It is currently challenging to measure the masses of the Kepler-51 planets using the radial velocity method for multiple reasons: the host star Kepler-51 is faint ($G \approx 14.7$) and exhibits a strong

stellar activity, and its planets have relatively low masses and long orbital periods. For the 2:1 solution, for example, the radial velocity semiamplitude induced by Kepler-51e ($m \approx 5 M_{\oplus}$ and $P \approx 260$ days) is only $\approx 0.5 \text{ m s}^{-1}$. The amplitudes induced by the inner transiting planets are $\lesssim 1 \text{ m s}^{-1}$.

8.2. Implications of the Updated Masses of the Inner Three Transiting Planets

Despite the uncertainties in the properties of the fourth planet, all the solutions found from our brute-force search imply $\lesssim 10 M_{\oplus}$ for the inner three transiting planets (Sections 7.1, 7.2). More quantitatively, the masses of Kepler-51c and d were found to be relatively insensitive to the assumed properties of the fourth planet and remain consistent with the previous values within $\sim 2\sigma$. A firm lower bound on the mass was not found for Kepler-51b, and the upper limit turned out to depend on the assumed period of Kepler-51e. The largest upper limit of $\lesssim 12$ (16) M_{\oplus} at the 95% (99.7%) level was found for the solutions in which Kepler-51e is slightly outside the 2:1 mean-motion resonance with Kepler-51d. The three planets' densities therefore remain low, as discussed in Section 1, although the larger upper limit for planet b's mass may help alleviate some of the theoretical difficulties for understanding its origins and atmospheric-loss history.

8.3. Peas-in-a-pod Pattern Extending beyond Kepler-51d?

It is not well understood what determines the orbital period distribution of the outermost transiting planets in the Kepler sample. S. C. Millholland et al. (2022) argued that the outermost transiting planets have shorter periods than expected purely from geometric and detection biases and that this could result from a drop-off in planet occurrence (i.e., physical truncation), a decrease in the typical planet radius, an increase in the period ratios between the adjacent planets, an increase in the mutual orbital inclination (i.e., change in architecture), or a combination of all of the above in the outer parts of planetary systems. In any of these cases, the system architecture beyond the transiting planets provides important clues for the formation and dynamical evolution of compact multiplanet systems.

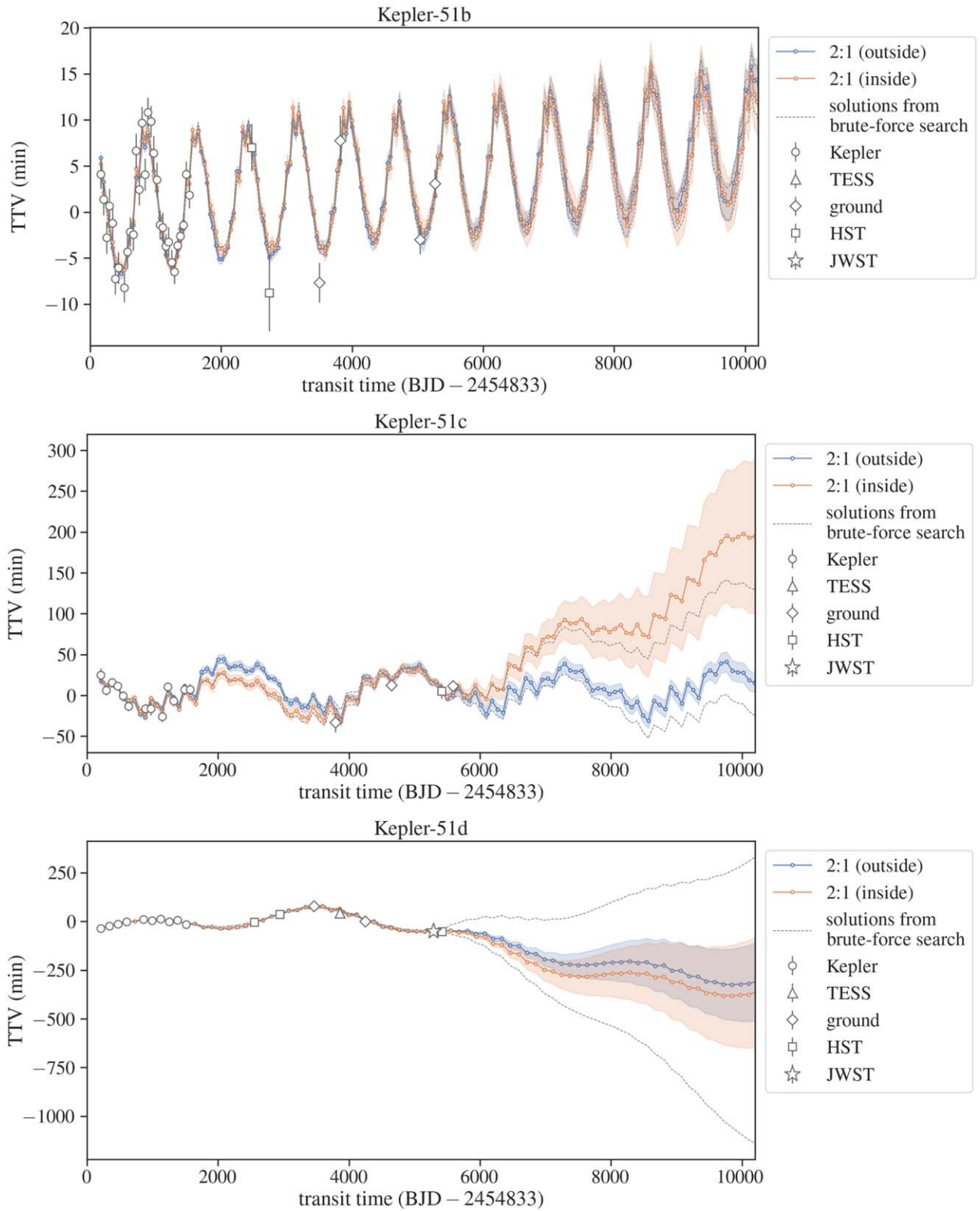


Figure 24. The TTVs of Kepler-51b, c, and d predicted up to 2036. Here the TTVs in the vertical axes are shown with respect to the linear ephemerides given by t_0 (BJD $-2,454,833$) = 159.1068, 209.9946, and 212.0493 and P (days) = 45.155296, 85.316963, and 130.175183 for planets b, c, and d, respectively; note that the appearance of the plot depends on these arbitrary choices. The 68% intervals of the solutions from the brute-force search are shown with the gray dashed lines. The 68% intervals for the 2:1 solutions based on posterior samples are shown with blue (outside) and orange (inside) shades; these are not the only possible solutions, and they are meant to illustrate the prediction uncertainty within a solution with a given period ratio.

Our analysis demonstrates that long-term TTV monitoring can provide useful insights for testing the various scenarios as described above. For Kepler-51, we show that the system is not physically

truncated at the outermost transiting planet by identifying another longer-period planet. We also find a solution that implies similar masses and period ratios for all four planets, i.e., the “peas-in-a-

pod” architecture extending beyond transiting planets (S. Millholland et al. 2017; L. M. Weiss et al. 2018). If this turns out to be a generic feature of Kepler multitransiting systems, then it might be that an increase in the mutual inclination is responsible for the “truncation” of the transiting systems. At this point, this is just one possible solution for Kepler-51, but our analysis suggests that this scenario is testable with more observations. To probe mutual orbital inclinations, searches for transit duration variations (TDVs) in addition to TTVs will also be informative, as we will discuss next.

8.4. Is the Whole System Indeed Coplanar?

Throughout the paper, we assumed that the orbits of the Kepler-51 planets are coplanar. The fact that Kepler-51b, c, and d are all transiting supports this assumption at least for these three. The assumption may also be supported from a dynamical point of view: a misalignment in the orbits necessarily induces nodal precession of the orbital planes, which would have easily caused the grazing orbit of Kepler-51c to rotate out of our line of sight to the star (see also Section 6.3). That said, this argument is less constraining for the orbit of Kepler-51e, which affects Kepler-51c’s orbit less than Kepler-51b and d. Indeed, a larger mutual inclination is consistent with the lack of its transits, although we note that a misalignment as small as 1° is sufficient for this to happen.

If the orbit of Kepler-51e is misaligned, Kepler-51d may exhibit TDVs associated with a slow drift of the transit impact parameter owing to nodal precession of its orbit (J. Miralda-Escudé 2002). We searched for TDVs of Kepler-51d using the precise transit durations from JWST and Kepler separated by 10 yr. We did not use the transits from the other facilities because they include gaps during transits, in particular around the ingress and egress. We evaluated the interval T between the halfway points of ingress and egress as an average of the “total” and “full” durations (Equations (14) and (15) of J. N. Winn 2011) using the posterior samples obtained from transit fits in Sections 3.1 and 3.3. The mean and standard deviation of the posterior distribution for the duration difference ΔT (JWST minus Kepler) were found to be 0.9 ± 1.7 minutes for the Kepler long-cadence data and 0.1 ± 2.2 minutes for the short-cadence data. Thus, there is no evidence of TDVs \dot{T} at a rate higher than a few $\times 10^{-1}$ minutes yr^{-1} . On the other hand, nodal precession due to planet e should induce the TDVs of planet d at a rate of

$$\dot{T} \sim 1 \text{ minute yr}^{-1} \left(\frac{b_d}{\sqrt{1-b_d^2}} \right) \left(\frac{P_d}{P_e} \right)^2 \left(\frac{m_e/M_\star}{M_\oplus/M_\odot} \right) \Delta i, \quad (8)$$

where Δi (rad) denotes the mutual inclination between the orbits of planets d and e (S. Shahaf et al. 2021). This reduces to $\dot{T} \sim 0.1 \Delta i$ minutes yr^{-1} adopting $b_d \sim 0.1$, $P_d/P_e \sim 1/2$, and $m_e/M_\star \sim 5M_\oplus/M_\odot$ (i.e., 2:1 solution). Thus, the lack of clear TDVs for Kepler-51d does not provide useful constraints on Δi at the moment: Δi of order unity is not excluded. We note, however, that a dynamical analysis also incorporating the transit durations/shapes of Kepler-51c may improve the constraint on Δi , because its grazing transits may serve as a more sensitive probe of nodal precession (note the $1/\sqrt{1-b^2}$ dependence in Equation (8)). We leave such an analysis for future work.

8.5. Are Four Planets Enough?

While we find no clear flaw in the four-planet model based on the available timing data, this does not necessarily rule out the possibility of a fifth planet in the system. There may indeed be

theoretical motivations for investigating such a hypothesis. For example, the period ratio of Kepler-51b and c deviates more from 1:2 ($(P_c/P_b)/2 - 1 = -0.055$) than is typically observed in other compact multitransiting systems (e.g., D. C. Fabrycky et al. 2014; F. Dai et al. 2024). This might be more naturally explained by the presence of another planet between planets b and c, forming a chain of three-body generalized Laplace resonances as seen in the TRAPPIST-1 system (e.g., E. Agol et al. 2021a). Although we found that a single planet located in between planets b and c does not appear to provide a satisfactory explanation for all the TTV data (see Figure 18), such solutions could work better in the presence of a fifth planet in the system, perhaps outside of Kepler-51d as in our four-planet solutions, so that it also affects the TTVs of Kepler-51d. Given the vast parameter space and the challenges in distinguishing between solutions even within the four-planet model, we leave further exploration of these possibilities for future work.

9. Summary and Conclusion

The Kepler-51 system is unlike any other discovered to date, with a young ($\lesssim 1$ Gyr) Sun-like star hosting three low-mass transiting planets all with mean densities $\sim 0.1 \text{ g cm}^{-3}$. The masses of these planets are derived via TTVs, and thus understanding the dynamical architecture of the entire system is critical for accurate mass measurements.

In this paper, we presented the discovery of a fourth planet in the Kepler-51 system based on an extensive transit timing data set spanning over 14 yr, which we compiled by reanalyzing the available Kepler/TESS photometry and by adding new measurements from JWST, HST, and ground-based facilities (Section 3). Our key findings are summarized as follows:

1. The new transit time of the outermost transiting planet, Kepler-51d, from JWST Cycle 1 observations significantly deviates from the prediction based on TTV models that consider the three known transiting planets alone (Section 6), which we confirmed with ground-based and follow-up HST observations. This demonstrates the presence of a fourth planet in the system,⁶⁸ whose transits have not been identified.
2. The fourth planet, Kepler-51e, located beyond Kepler-51d’s orbit with a wide range of masses and orbital periods can account for all the observed TTVs, including the discrepancy found in the JWST data (Section 7). In other words, the property of Kepler-51e is not well determined by the available TTVs. It could be either a low-mass ($\lesssim 10 M_\oplus$) planet on a near-circular orbit around a certain low-order mean-motion resonance with Kepler-51d or a more massive planet on a distant, eccentric orbit.
3. Despite this uncertainty, all the coplanar four-planet solutions found from our brute-force search imply $\lesssim 10 M_\oplus$ for the inner three transiting planets (Sections 7.1, 7.2); thus, their densities remain low. However, the increase in the mass upper limit for planet b will need to be considered carefully in the quantitative discussion.
4. One of the best solutions found from the brute-force search implies that Kepler-51e is around the 2:1 mean-motion resonance with Kepler-51d. This solution, unlike others, implies that Kepler-51e has a near-circular orbit and has a mass of $\sim 5 M_\oplus$ consistent with those of the inner three transiting planets. Thus, the near-circular, flat,

⁶⁸ This is the first incidental planet discovery made by JWST.

“peas-in-a-pod”-type architecture as seen in many compact multiplanet systems may extend to ≈ 260 days in this system. This is also the solution that allows for the largest mass for Kepler-51b and is least fine-tuned in terms of the orbital phase of Kepler-51e.

Long-term monitoring of Kepler systems for dynamical signatures of additional planets is proving essential for uncovering their full architecture and gaining the insights needed to understand the formation and evolution of compact multiplanet systems. Future observations of the Kepler-51 planets are vital both for robustly testing the various possible solutions for Kepler-51e and for improving the mass constraints on the three transiting planets, while also searching for any additional long-period TTVs and TDVs. Regardless of whether it is possible to uniquely determine Kepler-51e’s properties from the timing data alone, it is important to keep observing transits of the Kepler-51 planets so that their ephemerides are kept up to date to enable follow-up transit studies of this planet. The 2 hr deviation of Kepler-51d’s transit time from the prediction of the three-planet model during the JWST observation was fortunately not large enough for us to miss the transit. However, without more timing measurements for Kepler-51d, the prediction uncertainty grows to even larger values in the next few years, jeopardizing future transit investigations. We provide future predicted transit times of all three transiting planets (Table 7) to facilitate such follow-up observations.

Acknowledgments

This work is based on observations made with the NASA/ESA/CSA James Webb Space Telescope. The data were obtained from the Mikulski Archive for Space Telescopes at the Space Telescope Science Institute, which is operated by the Association of Universities for Research in Astronomy, Inc., under NASA contract NAS 5-03127 for JWST. These observations are associated with program GO-2571. Support for program GO-2571 was provided by NASA through a grant from the Space Telescope Science Institute, which is operated by the Association of Universities for Research in Astronomy, Inc., under NASA contract NAS 5-03127.

This research is based on observations made with the NASA/ESA Hubble Space Telescope obtained from the Space Telescope Science Institute, which is operated by the Association of Universities for Research in Astronomy, Inc., under NASA contract NAS 5-26555. These observations are associated with program DD Program 17585.

This paper made use of data collected by the Kepler and TESS missions. Funding for these mission is provided by the NASA Science Mission directorate. This research made use of Lightkurve, a Python package for Kepler and TESS data analysis (Lightkurve Collaboration et al. 2018).

This work has made use of data from the European Space Agency (ESA) mission Gaia (<https://www.cosmos.esa.int/gaia>), processed by the Gaia Data Processing and Analysis Consortium (DPAC, <https://www.cosmos.esa.int/web/gaia/dpac/consortium>). Funding for the DPAC has been provided by national institutions, in particular, the institutions participating in the Gaia Multilateral Agreement.

This publication makes use of data products from the Two Micron All Sky Survey, which is a joint project of the University of Massachusetts and the Infrared Processing and Analysis Center/California Institute of Technology, funded by

the National Aeronautics and Space Administration and the National Science Foundation.

This work is partly based on observations made with the MuSCAT2 instrument, developed by ABC, at Telescopio Carlos Sánchez operated on the island of Tenerife by the IAC in the Spanish Observatorio del Teide.

This work is partly based on observations made with the MuSCAT3 instrument, developed by the Astrobiology Center and under financial supports by JSPS KAKENHI (JP18H05439) and JST PRESTO (JPMJPR1775), at Faulkes Telescope North on Maui, HI, operated by the Las Cumbres Observatory.

The research leading to these results has received funding from the ARC grant for Concerted Research Actions, financed by the Wallonia-Brussels Federation. TRAPPIST is funded by the Belgian Fund for Scientific Research (Fond National de la Recherche Scientifique, FNRS) under the grant PDR T.0120.21. TRAPPIST-North is a project funded by the University of Liege (Belgium), in collaboration with Cadi Ayyad University of Marrakech (Morocco). M.G. is F.R.S.-FNRS Research Director and E.J. is F.R.S.-FNRS Senior Research Associate. The postdoctoral fellowship of K.B. is funded by F.R.S.-FNRS grant T.0109.20 and by the Francqui Foundation.

This work is partly based on observations from the Apache Point Observatory 3.5 m telescope, owned and operated by the Astrophysical Research Consortium. We acknowledge support from NSF grants AST 1907622, 1909506, 1909682, and 1910954 and the Research Corporation.

The Center for Exoplanets and Habitable Worlds is supported by Penn State and the Eberly College of Science.

Computations for this research were performed on the Pennsylvania State University’s Institute for Computational and Data Sciences Advanced CyberInfrastructure (ICDS-ACI), including the CyberLAMP cluster supported by NSF grant MRI-1626251. This content is solely the responsibility of the authors and does not necessarily represent the views of the Institute for Computational and Data Sciences.

Part of this research was carried out at the Jet Propulsion Laboratory, California Institute of Technology, under a contract with the National Aeronautics and Space Administration (80NM0018D0004).

We acknowledge financial support from the Agencia Estatal de Investigación of the Ministerio de Ciencia e Innovación MCIN/AEI/10.13039/501100011033 and the ERDF “A way of making Europe” through project PID2021-125627OB-C32, and from the Centre of Excellence “Severo Ochoa” award to the Instituto de Astrofísica de Canarias.

Work by K.M. was supported by JSPS KAKENHI grant No. 21H04998. E.E.-B. acknowledges financial support from the European Union and the State Agency of Investigation of the Spanish Ministry of Science and Innovation (MICINN) under the grant PRE2020-093107 of the Pre-Doc Program for the Training of Doctors (FPI-SO) through FSE funds. C.I.C. acknowledges support by NASA Headquarters through an appointment to the NASA Postdoctoral Program at the Goddard Space Flight Center, administered by ORAU through a contract with NASA. K.A.C. acknowledges support from the TESS mission via subaward s3449 from MIT. This work is partly supported by JSPS KAKENHI grant Nos. JP24H00017 and JP24K00689 and JSPS Bilateral Program No. JPJSBP120249910.

Facilities: JWST, HST(WFC3), Kepler, TESS, Astrophysical Research Consortium (ARC) 3.5m Telescope At Apache Point Observatory (APO) (ARCTIC), Instituto de Astrofísica

de Canarias 1.52m Carlos Sanchez Infrared Telescope (TCS) at Observatorio del TeideSanchezAfrica and Canary Islands, Las Cumbres Observatory Global Telescope Network (LCOGTN) 2m Faulkes Telescope North at Haleakala Observatory, LCO 2.0m (MuSCAT3).

Software: corner (D. Foreman-Mackey 2016), JAX (J. Bradbury et al. 2018), NumPyro (E. Bingham et al. 2018; D. Phan et al. 2019), AstroImageJ (K. A. Collins et al. 2017), TAPIR (E. Jensen 2013), jaxstar (K. Masuda 2023).

Some of the data presented in this article were obtained from the Mikulski Archive for Space Telescopes (MAST) at the Space Telescope Science Institute. The specific observations analyzed can be accessed via [10.17909/kxr3-7m59](https://doi.org/10.17909/kxr3-7m59) (transits of Kepler-51c and Kepler-51d) and [10.17909/t002-ht63](https://doi.org/10.17909/t002-ht63) (JWST transit of Kepler-51d).

Appendix A Corner Plots

A.1. Three-planet Model

In Section 6, we reproduced the TTV analysis in J. E. Libby-Roberts et al. (2020) using the code described in Section 5. Figure 25 compares the distributions of the posterior samples from the two analyses.

A.2. Four-planet Model Assuming $P/P_d \approx 2$ in Section 7.3

In Section 7.3, we performed an HMC sampling from the joint posterior pdf for the system parameters, assuming that Kepler-51e is around the 2:1 resonance with Kepler-51d. Figure 26 shows the corresponding corner plot, in which the

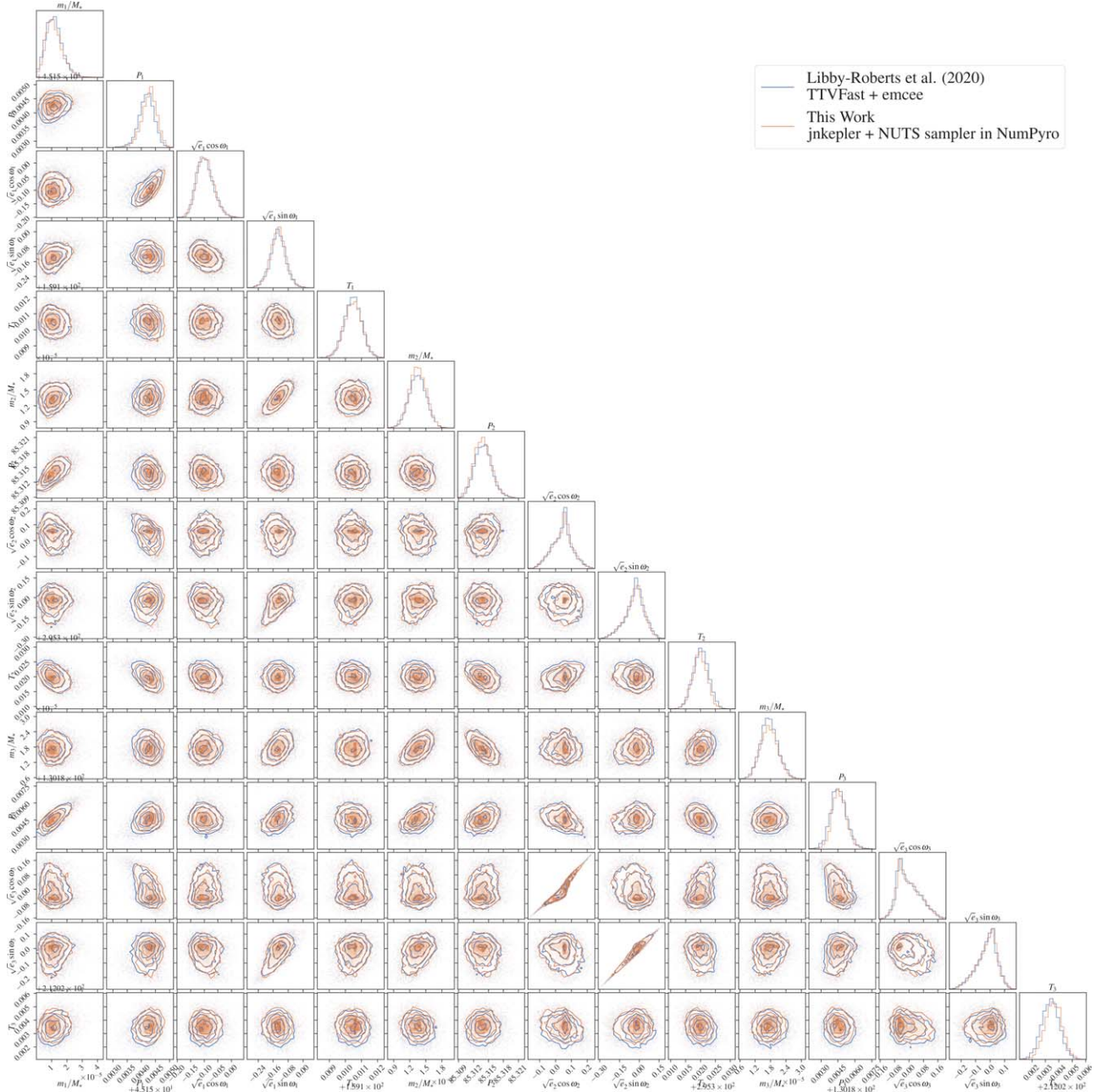


Figure 25. Corner plot (D. Foreman-Mackey 2016) for the posterior samples from the three-planet fit to the TTV data in J. E. Libby-Roberts et al. (2020).

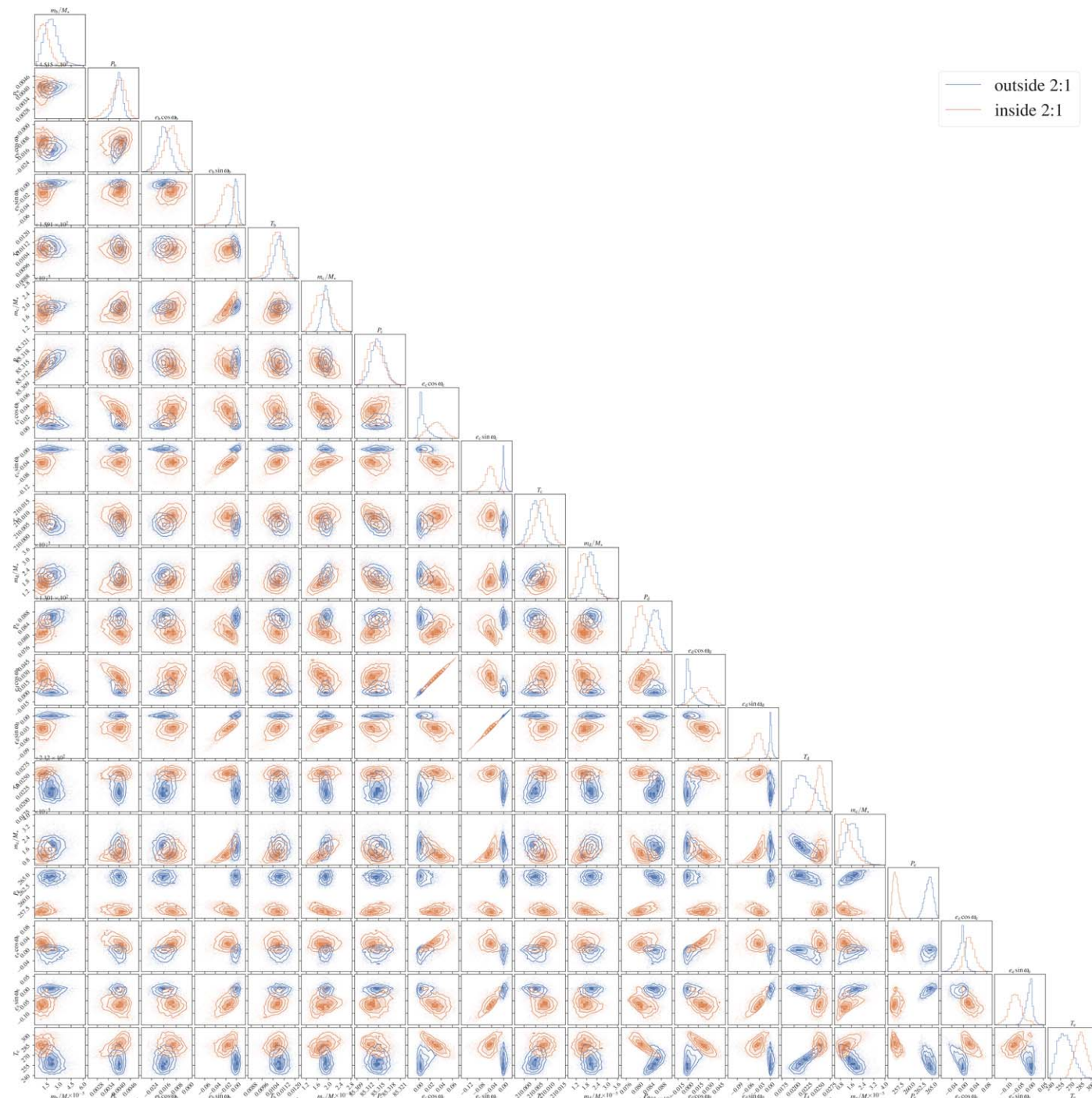


Figure 26. Corner plot (D. Foreman-Mackey 2016) for the posterior samples from the four-planet fit to all the TTV data in Table 1 assuming $P_e \approx 2P_d$.

blue and orange contours show samples for the priors assuming $P_e/P_d > 2$ and $P_e/P_d < 2$, respectively.

Appendix B Prediction of Future Transit Times

Table 7 lists the future predicted transit times of Kepler-51b, c, and d discussed in Section 8.1. The predictions

are based on the solutions with $P_e/P_d \approx 2$ (first four columns) and for all the solutions from the brute-force search (last two columns). For the former, the mean and standard deviation of the posterior models obtained in Section 7.3 are shown. For the latter, the same statistics are shown for timing models computed for all the solutions found from the brute-force search in Section 7.1.

Table 7
 Future Predicted Transit Times of Kepler-51b, c, and d based on the 2:1 Solutions and All Solutions from the Brute-force Search

Outside 2:1		Inside 2:1		All Solutions	
Mean (BJD)	SD (days)	Mean (BJD)	SD (days)	Mean (BJD)	SD (days)
Kepler-51b					
2460591.36365	0.00088	2460591.36346	0.00091	2460591.36313	0.00043
2460636.51763	0.00084	2460636.51745	0.00085	2460636.51743	0.00034
2460681.67237	0.00082	2460681.67235	0.00086	2460681.67222	0.00035
2460726.82830	0.00082	2460726.82760	0.00091	2460726.82779	0.00050
2460771.98367	0.00081	2460771.98341	0.00087	2460771.98346	0.00045
2460817.14042	0.00083	2460817.13958	0.00098	2460817.13977	0.00066
2460862.29691	0.00083	2460862.29649	0.00088	2460862.29660	0.00054
2460907.45488	0.00087	2460907.4547	0.0011	2460907.45399	0.00073
2460952.61018	0.00089	2460952.60994	0.00096	2460952.61010	0.00054
2460997.76918	0.00094	2460997.7700	0.0011	2460997.76872	0.00057
2461042.92390	0.00095	2461042.9239	0.0011	2461042.92368	0.00054
2461088.0806	0.0010	2461088.0810	0.0011	2461088.08083	0.00043
2461133.2351	0.0010	2461133.2354	0.0011	2461133.23504	0.00049
2461178.3896	0.0010	2461178.3892	0.0011	2461178.38945	0.00060
2461223.5432	0.0010	2461223.5434	0.0011	2461223.54304	0.00053
2461268.6966	0.0010	2461268.6967	0.0011	2461268.69631	0.00057
2461313.85053	0.00098	2461313.8509	0.0010	2461313.85034	0.00042
2461359.00414	0.00098	2461359.0045	0.0010	2461359.00387	0.00040
2461404.15842	0.00095	2461404.15857	0.00097	2461404.15838	0.00037
2461449.31329	0.00094	2461449.31341	0.00099	2461449.31310	0.00040
2461494.46873	0.00094	2461494.4681	0.0010	2461494.46829	0.00056
2461539.62414	0.00093	2461539.62377	0.00100	2461539.62394	0.00057
2461584.78109	0.00095	2461584.7799	0.0011	2461584.78022	0.00083
2461629.93727	0.00096	2461629.9363	0.0011	2461629.93668	0.00076
2461675.0951	0.0010	2461675.0943	0.0013	2461675.09392	0.00096
2461720.2507	0.0010	2461720.2497	0.0012	2461720.25010	0.00083
2461765.4095	0.0011	2461765.4096	0.0013	2461765.40845	0.00085
2461810.5640	0.0011	2461810.5634	0.0013	2461810.56335	0.00089
2461855.7210	0.0011	2461855.7208	0.0013	2461855.72068	0.00066
2461900.8756	0.0011	2461900.8753	0.0013	2461900.87493	0.00092
2461946.0299	0.0012	2461946.0292	0.0014	2461946.02938	0.00098
2461991.1835	0.0012	2461991.1835	0.0013	2461991.18304	0.00093
2462036.3372	0.0012	2462036.3372	0.0013	2462036.3366	0.0010
2462081.4909	0.0011	2462081.4915	0.0012	2462081.49052	0.00082
2462126.6443	0.0011	2462126.6450	0.0012	2462126.64405	0.00082
2462171.7991	0.0011	2462171.7997	0.0012	2462171.79895	0.00068
2462216.9537	0.0011	2462216.9545	0.0012	2462216.95363	0.00068
2462262.1088	0.0011	2462262.1090	0.0011	2462262.10874	0.00068
2462307.2647	0.0011	2462307.2651	0.0011	2462307.26482	0.00068
2462352.4216	0.0011	2462352.4212	0.0012	2462352.42108	0.00079
2462397.5774	0.0011	2462397.5773	0.0012	2462397.57734	0.00072
2462442.7356	0.0011	2462442.7354	0.0013	2462442.73487	0.00087
2462487.8914	0.0011	2462487.8909	0.0013	2462487.89108	0.00078
2462533.0498	0.0012	2462533.0502	0.0014	2462533.04912	0.00081
2462578.2046	0.0012	2462578.2042	0.0014	2462578.20421	0.00086
2462623.3619	0.0013	2462623.3617	0.0015	2462623.36162	0.00075
2462668.5162	0.0013	2462668.5156	0.0015	2462668.51551	0.00097
2462713.6706	0.0013	2462713.6695	0.0015	2462713.6700	0.0011
2462758.8244	0.0013	2462758.8239	0.0015	2462758.8237	0.0011
2462803.9779	0.0013	2462803.9772	0.0015	2462803.9769	0.0013
2462849.1313	0.0013	2462849.1313	0.0014	2462849.1307	0.0011
2462894.2849	0.0013	2462894.2848	0.0014	2462894.2842	0.0010
2462939.4396	0.0012	2462939.4395	0.0014	2462939.43893	0.00097
2462984.5939	0.0012	2462984.5941	0.0014	2462984.59342	0.00096
2463029.7490	0.0012	2463029.7487	0.0014	2463029.7486	0.0010
2463074.9052	0.0012	2463074.9051	0.0014	2463074.9047	0.0010
2463120.0617	0.0012	2463120.0610	0.0015	2463120.0608	0.0012
2463165.2174	0.0012	2463165.2172	0.0014	2463165.2171	0.0011
2463210.3760	0.0012	2463210.3758	0.0016	2463210.3749	0.0012
2463255.5316	0.0013	2463255.5314	0.0015	2463255.5312	0.0011
2463300.6898	0.0013	2463300.6907	0.0016	2463300.6892	0.0011

Table 7
(Continued)

Outside 2:1		Inside 2:1		All Solutions	
Mean (BJD)	SD (days)	Mean (BJD)	SD (days)	Mean (BJD)	SD (days)
2463345.8452	0.0013	2463345.8452	0.0016	2463345.8448	0.0010
2463391.0025	0.0014	2463391.0029	0.0016	2463391.00235	0.00092
2463436.1564	0.0014	2463436.1566	0.0016	2463436.1561	0.0010
2463481.3114	0.0014	2463481.3110	0.0016	2463481.3112	0.0011
2463526.4653	0.0014	2463526.4653	0.0016	2463526.4648	0.0011
2463571.6184	0.0014	2463571.6181	0.0016	2463571.6178	0.0012
2463616.7722	0.0014	2463616.7724	0.0016	2463616.7718	0.0010
2463661.9258	0.0014	2463661.9259	0.0016	2463661.9253	0.0011
2463707.0801	0.0013	2463707.0800	0.0016	2463707.0797	0.0010
2463752.2346	0.0013	2463752.2345	0.0016	2463752.2342	0.0011
2463797.3898	0.0013	2463797.3891	0.0016	2463797.3893	0.0012
2463842.5456	0.0013	2463842.5450	0.0016	2463842.5450	0.0013
2463887.7020	0.0013	2463887.7006	0.0017	2463887.7010	0.0015
2463932.8579	0.0013	2463932.8569	0.0016	2463932.8573	0.0014
2463978.0164	0.0014	2463978.0151	0.0019	2463978.0148	0.0016
2464023.1717	0.0014	2464023.1706	0.0018	2464023.1709	0.0015
2464068.3301	0.0014	2464068.3300	0.0018	2464068.3290	0.0015
2464113.4855	0.0015	2464113.4848	0.0019	2464113.4846	0.0015
2464158.6426	0.0015	2464158.6426	0.0018	2464158.6421	0.0013
2464203.7966	0.0015	2464203.7964	0.0019	2464203.7960	0.0015
2464248.9521	0.0015	2464248.9514	0.0019	2464248.9514	0.0015
2464294.1057	0.0015	2464294.1057	0.0019	2464294.1050	0.0014
2464339.2587	0.0015	2464339.2586	0.0019	2464339.2581	0.0015
2464384.4130	0.0015	2464384.4134	0.0018	2464384.4125	0.0013
2464429.5665	0.0015	2464429.5669	0.0018	2464429.5659	0.0013
2464474.7204	0.0015	2464474.7209	0.0018	2464474.7202	0.0012
2464519.8753	0.0014	2464519.8758	0.0018	2464519.8750	0.0012
2464565.0305	0.0014	2464565.0303	0.0018	2464565.0301	0.0013
2464610.1858	0.0014	2464610.1858	0.0018	2464610.1856	0.0013
2464655.3426	0.0015	2464655.3417	0.0018	2464655.3419	0.0015
2464700.4986	0.0015	2464700.4980	0.0018	2464700.4982	0.0015
2464745.6565	0.0015	2464745.6556	0.0020	2464745.6553	0.0016
2464790.8122	0.0015	2464790.8112	0.0019	2464790.8116	0.0016
Kepler-51c					
2460588.5952	0.0047	2460588.5966	0.0050	2460588.5946	0.0041
2460673.9091	0.0049	2460673.9127	0.0055	2460673.9094	0.0051
2460759.2335	0.0046	2460759.2385	0.0062	2460759.2321	0.0066
2460844.5395	0.0049	2460844.5477	0.0067	2460844.5417	0.0078
2460929.8488	0.0052	2460929.8606	0.0074	2460929.8537	0.0090
2461015.1778	0.0047	2461015.1903	0.0085	2461015.180	0.011
2461100.4873	0.0053	2461100.5026	0.0088	2461100.492	0.012
2461185.8012	0.0060	2461185.8196	0.0091	2461185.808	0.012
2461271.1403	0.0061	2461271.1579	0.0099	2461271.143	0.013
2461356.4540	0.0067	2461356.473	0.010	2461356.459	0.014
2461441.7643	0.0071	2461441.787	0.011	2461441.773	0.015
2461527.0987	0.0067	2461527.123	0.012	2461527.105	0.016
2461612.4119	0.0066	2461612.439	0.012	2461612.421	0.016
2461697.7198	0.0066	2461697.751	0.013	2461697.733	0.017
2461783.0487	0.0064	2461783.080	0.014	2461783.060	0.018
2461868.3664	0.0062	2461868.400	0.015	2461868.379	0.019
2461953.6803	0.0065	2461953.716	0.015	2461953.694	0.019
2462039.0083	0.0070	2462039.043	0.016	2462039.020	0.019
2462124.3296	0.0071	2462124.364	0.017	2462124.341	0.020
2462209.6408	0.0071	2462209.678	0.017	2462209.654	0.020
2462294.9562	0.0068	2462294.995	0.018	2462294.970	0.021
2462380.2742	0.0062	2462380.315	0.019	2462380.288	0.022
2462465.5829	0.0059	2462465.627	0.020	2462465.599	0.023
2462550.8915	0.0056	2462550.937	0.021	2462550.909	0.024
2462636.2099	0.0053	2462636.257	0.022	2462636.226	0.025
2462721.5261	0.0057	2462721.575	0.023	2462721.541	0.025
2462806.8387	0.0065	2462806.888	0.024	2462806.854	0.026
2462892.1574	0.0069	2462892.207	0.025	2462892.172	0.027

Table 7
(Continued)

Outside 2:1		Inside 2:1		All Solutions	
Mean (BJD)	SD (days)	Mean (BJD)	SD (days)	Mean (BJD)	SD (days)
2462977.4755	0.0069	2462977.527	0.026	2462977.489	0.028
2463062.7821	0.0071	2463062.837	0.027	2463062.798	0.029
2463148.0949	0.0071	2463148.153	0.029	2463148.112	0.030
2463233.4171	0.0063	2463233.478	0.031	2463233.432	0.031
2463318.7224	0.0066	2463318.786	0.032	2463318.741	0.032
2463404.0345	0.0070	2463404.101	0.033	2463404.054	0.034
2463489.3688	0.0063	2463489.436	0.035	2463489.384	0.035
2463574.6821	0.0073	2463574.751	0.035	2463574.699	0.036
2463659.9953	0.0081	2463660.067	0.036	2463660.014	0.037
2463745.3316	0.0073	2463745.403	0.038	2463745.346	0.039
2463830.6423	0.0074	2463830.718	0.039	2463830.660	0.040
2463915.9514	0.0075	2463916.032	0.040	2463915.972	0.041
2464001.2859	0.0067	2464001.368	0.042	2464001.304	0.043
2464086.5977	0.0066	2464086.683	0.044	2464086.619	0.044
2464171.9080	0.0069	2464171.996	0.044	2464171.931	0.045
2464257.2445	0.0073	2464257.333	0.047	2464257.263	0.046
2464342.5655	0.0082	2464342.656	0.048	2464342.585	0.046
2464427.8787	0.0088	2464427.971	0.048	2464427.900	0.047
2464513.2055	0.0091	2464513.299	0.050	2464513.225	0.048
2464598.5235	0.0092	2464598.620	0.052	2464598.544	0.049
2464683.8329	0.0092	2464683.934	0.054	2464683.856	0.050
2464769.1486	0.0088	2464769.252	0.055	2464769.172	0.051
Kepler-51d					
2460642.5493	0.0043	2460642.5429	0.0044	2460642.556	0.033
2460772.7134	0.0058	2460772.7033	0.0062	2460772.723	0.042
2460902.8905	0.0074	2460902.8765	0.0084	2460902.899	0.052
2461033.0471	0.0091	2461033.028	0.011	2461033.058	0.062
2461163.223	0.011	2461163.199	0.015	2461163.231	0.073
2461293.374	0.013	2461293.345	0.019	2461293.385	0.084
2461423.548	0.016	2461423.514	0.024	2461423.555	0.095
2461553.698	0.018	2461553.660	0.029	2461553.71	0.11
2461683.871	0.021	2461683.828	0.035	2461683.88	0.12
2461814.027	0.024	2461813.981	0.041	2461814.03	0.13
2461944.199	0.029	2461944.149	0.047	2461944.20	0.14
2462074.363	0.033	2462074.311	0.053	2462074.37	0.15
2462204.536	0.038	2462204.482	0.059	2462204.54	0.16
2462334.709	0.042	2462334.654	0.065	2462334.71	0.17
2462464.886	0.048	2462464.829	0.071	2462464.88	0.19
2462595.064	0.053	2462595.007	0.077	2462595.06	0.20
2462725.243	0.059	2462725.183	0.084	2462725.23	0.21
2462855.422	0.064	2462855.362	0.090	2462855.41	0.22
2462985.599	0.070	2462985.536	0.097	2462985.58	0.23
2463115.778	0.075	2463115.71	0.10	2463115.76	0.25
2463245.948	0.081	2463245.88	0.11	2463245.92	0.26
2463376.126	0.085	2463376.06	0.12	2463376.10	0.28
2463506.288	0.091	2463506.22	0.13	2463506.26	0.29
2463636.465	0.095	2463636.39	0.13	2463636.43	0.31
2463766.62	0.10	2463766.55	0.14	2463766.59	0.33
2463896.80	0.10	2463896.72	0.15	2463896.76	0.35
2464026.95	0.11	2464026.88	0.16	2464026.91	0.36
2464157.13	0.11	2464157.05	0.17	2464157.08	0.38
2464287.29	0.12	2464287.21	0.18	2464287.24	0.40
2464417.46	0.12	2464417.38	0.18	2464417.40	0.42
2464547.63	0.13	2464547.54	0.19	2464547.57	0.44
2464677.80	0.13	2464677.72	0.20	2464677.74	0.46
2464807.98	0.13	2464807.90	0.21	2464807.91	0.48

(This table is available in machine-readable form in the [online article](#).)

Appendix C

Three-planet Photodynamical Modeling of the Kepler Data

We performed a so-called photodynamical modeling of the Kepler light curves, in which model transit light curves are computed using the planets' orbits from numerical integration. Here we consider only three planets (Kepler-51b, c, d) that are known to transit.

C.1. The Data

We used the normalized and detrended flux obtained in Section 3.3. We used short-cadence data whenever available and excluded from the analysis the transits with more than 20% of the data points missing in the 1-day window, as well as the last transits of Kepler-51b and Kepler-51d that occurred simultaneously around $\text{BJD} = 2,456,346.8$.

C.2. The Flux Model

Our model computes the relative flux loss F at a given time due to all three transiting planets, taking into account the mutual gravitational interactions between the planets when solving their motion. We assume that the planets are fully optically thick spheres and that the stellar surface brightness profile is described by the quadratic limb-darkening law, $\propto 1 - u_1(1 - \mu) - u_2(1 - \mu)^2$, with μ being the sky-projected distance from the star's center normalized by the stellar radius.

The model parameters are as follows:

1. planet-to-star mass ratio m ;
2. planet-to-star radius ratio r ;
3. osculating orbital elements at the start of integration, here chosen to be $\text{BJD} = 2,454,833 + 155$;
4. mean density of the star ρ_* ; and
5. limb-darkening coefficients $q_1 = (u_1 + u_2)^2$ and $q_2 = u_1/2(u_1 + u_2)$.

The first three quantities are defined for each planet and are specified by the subscripts b, c, and d when necessary. We use the same set of osculating orbital elements as given in Section 5, though in practice we use the transit impact parameter b instead of the inclination i , computing the latter from the former and other parameters via Equation (7) of J. N. Winn (2011). Because the relative flux data alone do not constrain the absolute dimensions of the system, we fix the stellar mass to be $1 M_\odot$ and fit R_* and ρ_* interchangeably in the dynamical modeling. Instead of u_1 and u_2 , we use q_1 and q_2 , which can be sampled from the bounded prior following D. M. Kipping (2013).

Given the mass ratios and initial osculating orbital elements, we numerically compute the transit times of the planets and their positions and velocities at the transit centers in the same way as described in Section 5. The positions of the planets at each time are then calculated assuming that the in-transit motion is linear. The flux loss is computed using the solution vector as defined in E. Agol et al. (2020), where we use `exoplanet-ops[jax]`, which provides JAX implementations of `exoplanet` (D. Foreman-Mackey et al. 2020). For long-cadence data, the flux is upsampled by a factor of 11 and averaged to take into account finite integration time (D. M. Kipping 2010). We checked the flux calculation by comparing the code output (with planetary mass ratios set to be 10^{-12}) with flux computed using `exoplanet` (D. Foreman-Mackey et al. 2020) for several sets of the common orbital parameters. The relative flux difference without finite time integration was found to be $\sim 10^{-6}$ at most, and the errors due to

finite time integration were confirmed to be at most $\sim 20\%$ of the assigned flux errors, whose medians are 2.9×10^{-4} and 1.6×10^{-3} for the long- and short-cadence data, respectively.

C.3. Likelihood

The above model provides the flux loss for the long- and short-cadence data, F_{long} and F_{short} , for given times and a set of physical model parameters $\theta_{\text{phys}} = \{m, r, P, e, \omega, b, \Omega, T, q_1, q_2, R_*\}$. The flux model was then used to define the likelihood $\mathcal{L}_{\text{long}}$ and $\mathcal{L}_{\text{short}}$ for the long-cadence data f_{long} and the short-cadence data excluding the simultaneous transits of Kepler-51b and Kepler-51d f_{short} , respectively:

$$\begin{aligned} \mathcal{L}_{\text{long}}(\theta_{\text{phys}}, \theta_{\text{noise}}, \mu_{\text{long}}) \\ \equiv \mathcal{N}(f_{\text{long}}; F_{\text{long}}(\theta_{\text{phys}}) + \mu_{\text{long}}, \Sigma(\theta_{\text{noise}})) \end{aligned} \quad (\text{C1})$$

$$\begin{aligned} \mathcal{L}_{\text{short}}(\theta_{\text{phys}}, \theta_{\text{noise}}, \mu_{\text{short}}) \\ \equiv \mathcal{N}(f_{\text{short}}; F_{\text{short}}(\theta_{\text{phys}}) + \mu_{\text{short}}, \Sigma(\theta_{\text{noise}})), \end{aligned} \quad (\text{C2})$$

where f and F are treated as vectors and $\mathcal{N}(x; \mu, \Sigma)$ is a multivariate normal distribution with the mean μ and covariance matrix Σ . We adopt the same covariance matrix given by Equation (2), which is the sum of the Matérn-3/2 covariance and the white-noise term, and so θ_{noise} consists of α , ρ , and σ_{jit} defined separately for the long- and short-cadence data.

C.4. Inference

To obtain a reasonable initial guess for the full N -body photodynamical fitting, we first fitted the whole long-cadence light curve with an N -body transit model by minimizing χ^2 using `jaxopt.ScipyBoundedMinimize`. Here we fixed the mass ratios and orbital parameters except for the inclination to the values derived from the TTV fit, but we optimized the impact parameters, radius ratios, limb-darkening coefficients, and mean stellar density. This allowed us to obtain a set of system parameters for the N -body light-curve model that fits the long-cadence data.

We then sampled from the joint posterior distribution for all the parameters $\theta = \{\theta_{\text{phys}}, \theta_{\text{noise}}, \mu\}$ conditioned on the flux data f :

$$p(\theta|f) \propto \mathcal{L}(f|\theta) \pi(\theta) \quad (\text{C3})$$

adopting the log-likelihood

$$\ln \mathcal{L}(\theta) = \ln \mathcal{L}_{\text{long}}(\theta) + \ln \mathcal{L}_{\text{short}}(\theta) \quad (\text{C4})$$

and the prior pdf π separable for the parameters. We adopted a uniform, log-uniform, or normal distribution for the prior of each parameter as summarized in Table 8. Here we fixed Ω_d to be zero without loss of generality, and restricted $|\Omega_b|$ and $|\Omega_c|$ to be less than 1 rad. Care should be taken about the range of impact parameters; usually it is chosen to be positive, but in multitransiting systems both signs (i.e., $i < 90^\circ$ and $i > 90^\circ$) need to be considered if the difference matters. Here we assume $b_c > 0$, again without loss of generality, and allow b_b and b_d to take both positive and negative values. We were able to sample b_b and b_d well from such a prior, as the joint posterior pdf happened to have large enough density at $(b_b, b_d) \approx (0, 0)$ in this problem.

The sampling was performed using NUTS (S. Duane et al. 1987; M. Betancourt 2017) as implemented in `NumPyro` (E. Bingham et al. 2018; D. Phan et al. 2019). We initialized the Markov chains at the parameter values derived in the first

Table 8
Parameters of the Kepler-51 System from Three-planet Photodynamical Modeling in Appendix C

	Mean	95% HDI	Prior
Physical Parameters			
Host star:			
Mean density ρ_* (ρ_\odot)	1.818	[1.572, 2.118]	...
Radius $R_*/M_*^{1/3}$ ($R_\odot/M_\odot^{1/3}$)	0.820	[0.777, 0.857]	$\mathcal{N}(1, 1), R_*/M_*^{1/3} > 0$
Limb-darkening coefficients q_1	0.296	[0.198, 0.401]	$\mathcal{U}(0, 1)$
Limb-darkening coefficients q_2	0.400	[0.265, 0.556]	$\mathcal{U}(0, 1)$
Kepler-51b:			
Mass ratio m (M_\oplus/M_\odot)	2.060	[0.001, 4.897]	$\mathcal{U}(0, 5 \times 10^{-4})$
Radius ratio r	0.073	[0.072, 0.073]	$\mathcal{U}(0, 0.2)$
Mean density ρ_p (g cm^{-3})	0.041	[0.000, 0.096]	
Time of inferior conjunction (BKJD)	159.110	[159.109, 159.111]	$\mathcal{U}(T_0 - 0.1, T_0 + 0.1)$
Orbital period (days)	45.154	[45.153, 45.155]	$\mathcal{U}(P_0 - 0.5, P_0 + 0.5)$
Eccentricity e	0.042	[0.014, 0.079]	$\mathcal{U}(0, 0.3)$
$e \cos \omega$	-0.022	[-0.039, -0.006]	$\omega \sim \mathcal{U}(0, 2\pi)$
$e \sin \omega$	-0.034	[-0.072, -0.003]	$\omega \sim \mathcal{U}(0, 2\pi)$
Impact parameter b	0.043	[-0.300, 0.315]	$\mathcal{U}(-1.1, 1.1)$
Longitude of ascending node Ω (deg)	-0.625	[-13.976, 12.200]	$\mathcal{U}(-1 \text{ rad}, 1 \text{ rad})$
Kepler-51c:			
Mass ratio m (M_\oplus/M_\odot)	4.080	[3.062, 5.153]	$\mathcal{U}(0, 5 \times 10^{-4})$
Radius ratio r	0.060	[0.048, 0.077]	$\mathcal{U}(0, 0.2)$
Mean density ρ_p (g cm^{-3})	0.158	[0.053, 0.269]	
Time of inferior conjunction (BKJD)	210.009	[210.003, 210.016]	$\mathcal{U}(T_0 - 0.1, T_0 + 0.1)$
Orbital period (days)	85.312	[85.308, 85.316]	$\mathcal{U}(P_0 - 0.5, P_0 + 0.5)$
Eccentricity e	0.038	[0.000, 0.092]	$\mathcal{U}(0, 0.3)$
$e \cos \omega$	0.016	[-0.009, 0.051]	$\omega \sim \mathcal{U}(0, 2\pi)$
$e \sin \omega$	-0.031	[-0.090, 0.007]	$\omega \sim \mathcal{U}(0, 2\pi)$
Impact parameter b	0.979	[0.956, 1.005]	$\mathcal{U}(0, 1.1)$
Longitude of ascending node Ω (deg)	0.782	[-2.149, 3.660]	$\mathcal{U}(-1 \text{ rad}, 1 \text{ rad})$
Kepler- 51d:			
Mass ratio m (M_\oplus/M_\odot)	6.210	[3.988, 8.573]	$\mathcal{U}(0, 5 \times 10^{-4})$
Radius ratio r	0.099	[0.098, 0.099]	$\mathcal{U}(0, 0.2)$
Mean density ρ_p (g cm^{-3})	0.050	[0.034, 0.067]	
Time of inferior conjunction (BKJD)	212.024	[212.022, 212.026]	$\mathcal{U}(T_0 - 0.1, T_0 + 0.1)$
Orbital period (days)	130.184	[130.182, 130.186]	$\mathcal{U}(P_0 - 0.5, T_0 + 0.5)$
Eccentricity e	0.030	[0.000, 0.075]	$\mathcal{U}(0, 0.3)$
$e \cos \omega$	0.010	[-0.011, 0.038]	$\omega \sim \mathcal{U}(0, 2\pi)$
$e \sin \omega$	-0.025	[-0.075, 0.006]	$\omega \sim \mathcal{U}(0, 2\pi)$
Impact parameter b	0.012	[-0.256, 0.262]	$\mathcal{U}(-1.1, 1.1)$
Longitude of ascending node Ω (deg)		0 (fixed)	
Noise Parameters			
Mean flux $\mu \times 10^5$ (long cadence)	1.196	[-0.941, 3.460]	$\mathcal{N}(0, 10)$
$\ln \sigma_{\text{jit}}$ (long cadence)	-11.463	[-13.953, -9.277]	$\mathcal{U}(-14, -4)$
$\ln \alpha$ (long cadence)	-8.812	[-9.025, -8.607]	$\mathcal{U}(-14, -4)$
$\ln \rho$ (long cadence)	-3.577	[-4.079, -3.089]	$\mathcal{U}(-5, 1)$
Mean flux $\mu \times 10^5$ (short cadence)	-0.425	[-3.199, 2.433]	$\mathcal{N}(0, 100)$
$\ln \sigma_{\text{jit}}$ (short cadence)	-11.939	[-13.996, -9.907]	$\mathcal{U}(-14, -4)$
$\ln \alpha$ (short cadence)	-8.679	[-8.909, -8.460]	$\mathcal{U}(-14, -4)$
$\ln \rho$ (short cadence)	-3.926	[-4.395, -3.416]	$\mathcal{U}(-5, 1)$

Note. Note that this model fails to reproduce the JWST transit time, as does the three-planet TTV-only model in Section 6.

paragraph of this subsection and ran four chains for 1000 tuning steps and for 2000 steps to draw 8000 posterior samples in total, setting the target acceptance probability to be 0.95 and the maximum tree depth to be 11. We found $\hat{R} = 1.00$ – 1.05 and estimated $n_{\text{eff}} = 100$ – 1000 except for b_b , for which $\hat{R} = 1.08$ and $n_{\text{eff}} \approx 80$. The poorer convergence is a result of the bimodal nature of the parameter’s posterior distribution, and we did not attempt to improve the statistics through extended sampling.

C.5. Results

The summary statistics based on the posterior samples are shown in Table 8. The resulting posterior models appear to be almost identical to those in Figures 3–5 and thus are not shown. The residuals from the maximum likelihood model (i.e., $f - F - \mu$ in Equations (C1)–(C2)) divided by the assigned flux errors (i.e., σ) were found to be consistent with zero-mean normal distributions with the standard deviations of 1.1 and

0.98 for the long- and short-cadence data, respectively, except for a small number of outliers. The χ^2 values are ≈ 1465 for the 1458 long-cadence data points and $\approx 22,800$ for the 24,208 short-cadence data points. When the mean GP prediction was subtracted from these residuals, the normalized standard deviations were 0.90 and 0.97, respectively. These are consistent with small inferred jitters σ_{jit} .

The photodynamical modeling constrains the mutual orbital inclinations, apparently driven by planet c's grazing orbit, which makes its transits highly sensitive to small variations in orbital inclination. The inclinations of the orbits of Kepler-51b and Kepler-51c relative to that of Kepler-51d are inferred to be 0° – 13° and 0° – 3° (95% HDIs), respectively. Despite this difference, the resulting planetary masses and eccentricities remain consistent with those from TTV-only fitting (see Section 6), and so do the transit time predictions after the Kepler observations. Therefore, we conclude that the three-planet model is incompatible with the JWST timing measurement, even when accounting for the possibility of nonzero mutual orbital inclinations.

ORCID iDs

Kento Masuda  <https://orcid.org/0000-0003-1298-9699>
 Jessica E. Libby-Roberts  <https://orcid.org/0000-0002-2990-7613>
 John H. Livingston  <https://orcid.org/0000-0002-4881-3620>
 Kevin B. Stevenson  <https://orcid.org/0000-0002-7352-7941>
 Peter Gao  <https://orcid.org/0000-0002-8518-9601>
 Shreyas Vissapragada  <https://orcid.org/0000-0003-2527-1475>
 Guangwei Fu  <https://orcid.org/0000-0002-3263-2251>
 Te Han  <https://orcid.org/0000-0002-7127-7643>
 Michael Greklek-McKeon  <https://orcid.org/0000-0002-0371-1647>
 Suvrath Mahadevan  <https://orcid.org/0000-0001-9596-7983>
 Eric Agol  <https://orcid.org/0000-0002-0802-9145>
 Aaron Bello-Arufe  <https://orcid.org/0000-0003-3355-1223>
 Zachory Berta-Thompson  <https://orcid.org/0000-0002-3321-4924>
 Caleb I. Cañas  <https://orcid.org/0000-0003-4835-0619>
 Yayaati Chachan  <https://orcid.org/0000-0003-1728-8269>
 Leslie Hebb  <https://orcid.org/0000-0003-1263-8637>
 Renyu Hu  <https://orcid.org/0000-0003-2215-8485>
 Yui Kawashima  <https://orcid.org/0000-0003-3800-7518>
 Heather A. Knutson  <https://orcid.org/0000-0002-5375-4725>
 Caroline V. Morley  <https://orcid.org/0000-0002-4404-0456>
 Catriona A. Murray  <https://orcid.org/0000-0001-8504-5862>
 Kazumasa Ohno  <https://orcid.org/0000-0003-3290-6758>
 Armen Tokadjian  <https://orcid.org/0000-0002-4675-9069>
 Xi Zhang  <https://orcid.org/0000-0002-8706-6963>
 Luis Welbanks  <https://orcid.org/0000-0003-0156-4564>
 Matthew C. Nixon  <https://orcid.org/0000-0001-8236-5553>
 Richard Freedman  <https://orcid.org/0000-0001-9333-4306>
 Norio Narita  <https://orcid.org/0000-0001-8511-2981>
 Akihiko Fukui  <https://orcid.org/0000-0002-4909-5763>
 Jerome P. de Leon  <https://orcid.org/0000-0002-6424-3410>
 Mayuko Mori  <https://orcid.org/0000-0003-1368-6593>
 Enric Palle  <https://orcid.org/0000-0003-0987-1593>
 Felipe Murgas  <https://orcid.org/0000-0001-9087-1245>
 Hannu Parviainen  <https://orcid.org/0000-0001-5519-1391>

Emma Esparza-Borges  <https://orcid.org/0000-0002-2341-3233>
 Daniel Jontof-Hutter  <https://orcid.org/0000-0002-6227-7510>
 Karen A. Collins  <https://orcid.org/0000-0001-6588-9574>
 Paul Benni  <https://orcid.org/0000-0001-6981-8722>
 Khalid Barkaoui  <https://orcid.org/0000-0003-1464-9276>
 Francisco J. Pozuelos  <https://orcid.org/0000-0003-1572-7707>
 Michaël Gillon  <https://orcid.org/0000-0003-1462-7739>
 Emmanuel Jehin  <https://orcid.org/0000-0001-8923-488X>
 Zouhair Benkhaldoun  <https://orcid.org/0000-0001-6285-9847>
 Suzanne Hawley  <https://orcid.org/0000-0002-6629-4182>
 Andrea S. J. Lin  <https://orcid.org/0000-0002-9082-6337>
 Guðmundur Stefánsson  <https://orcid.org/0000-0001-7409-5688>
 Allyson Bieryla  <https://orcid.org/0000-0001-6637-5401>
 Mesut Yilmaz  <https://orcid.org/0000-0002-3276-0704>
 Hakan Volkan Senavci  <https://orcid.org/0000-0002-8961-277X>
 Eric Girardin  <https://orcid.org/0000-0002-5443-3640>
 Giuseppe Marino  <https://orcid.org/0000-0001-8134-0389>
 Gavin Wang  <https://orcid.org/0000-0003-3092-4418>

References

- Agol, E., & Deck, K. 2016, *ApJ*, 818, 177
 Agol, E., Dorn, C., Grimm, S. L., et al. 2021a, *PSJ*, 2, 1
 Agol, E., Hernandez, D. M., & Langford, Z. 2021b, *MNRAS*, 507, 1582
 Agol, E., Luger, R., & Foreman-Mackey, D. 2020, *AJ*, 159, 123
 Agol, E., Steffen, J., Sari, R., & Clarkson, W. 2005, *MNRAS*, 359, 567
 Aigrain, S., & Foreman-Mackey, D. 2023, *ARA&A*, 61, 329
 Akinsanmi, B., Santos, N. C., Faria, J. P., et al. 2020, *A&A*, 635, L8
 Almenara, J. M., Bonfils, X., Guillot, T., et al. 2024, *A&A*, 683, A96
 Andrae, R., Schulze-Hartung, T., & Melchior, P. 2010, arXiv:1012.3754
 Angus, R., Morton, T. D., Foreman-Mackey, D., et al. 2019, *AJ*, 158, 173
 Barkaoui, K., Burdanov, A., Hellier, C., et al. 2019, *AJ*, 157, 43
 Barros, S. C. C., Boue, G., Gibson, N. P., et al. 2013, *MNRAS*, 430, 3032
 Batalha, N. M., Rowe, J. F., Bryson, S. T., et al. 2013, *ApJS*, 204, 24
 Bell, T. J., Ahler, E.-M., Brande, J., et al. 2022, *JOSS*, 7, 4503
 Betancourt, M. 2017, arXiv:1701.02434
 Bingham, E., Chen, J. P., Jankowiak, M., et al. 2018, arXiv:1810.09538
 Birkmann, S. M., Ferruit, P., Giardino, G., et al. 2022, *A&A*, 661, A83
 Blondel, M., Berthet, Q., Cuturi, M., et al. 2021, arXiv:2105.15183
 Bradbury, J., Frostig, R., Hawkins, P., et al. 2018, JAX: Composable Transformations of Python+NumPy Programs, 0.2.5, <http://github.com/google/jax>
 Bradley, L., Sipőcz, B., Robitaille, T., et al. 2020, *astropy/photutils: v1.0.0*, Zenodo, doi:10.5281/zenodo.4044744
 Brewer, J. M., & Fischer, D. A. 2018, *ApJS*, 237, 38
 Bryan, M. L., Knutson, H. A., Lee, E. J., et al. 2019, *AJ*, 157, 52
 Chachan, Y., Lee, E. J., & Knutson, H. A. 2021, *ApJ*, 919, 63
 Choi, J., Dotter, A., Conroy, C., et al. 2016, *ApJ*, 823, 102
 Claret, A., Hauschildt, P. H., & Witte, S. 2012, *A&A*, 546, A14
 Collins, K. A., Kielkopf, J. F., Stassun, K. G., & Hessman, F. V. 2017, *AJ*, 153, 77
 Dai, F., Goldberg, M., Batygin, K., et al. 2024, *AJ*, 168, 239
 Dai, F., Masuda, K., Beard, C., et al. 2023, *AJ*, 165, 33
 Deck, K. M., & Agol, E. 2015, *ApJ*, 802, 116
 Deck, K. M., Agol, E., Holman, M. J., & Nesvorný, D. 2014, *ApJ*, 787, 132
 Dotter, A. 2016, *ApJS*, 222, 8
 Duane, S., Kennedy, A. D., Pendleton, B. J., & Roweth, D. 1987, *PhLB*, 195, 216
 El-Badry, K., Rix, H.-W., & Heintz, T. M. 2021, *MNRAS*, 506, 2269
 Fabrycky, D. C. 2010, arXiv:1006.3834
 Fabrycky, D. C., Lissauer, J. J., Ragozzine, D., et al. 2014, *ApJ*, 790, 146
 Foreman-Mackey, D. 2016, *JOSS*, 24
 Foreman-Mackey, D. 2018, *RNAAS*, 2, 31
 Foreman-Mackey, D., Agol, E., Angus, R., & Ambikasaran, S. 2017, arXiv:1703.09710

- Foreman-Mackey, D., Luger, R., Czekala, I., et al. 2020, *exoplanet-dev/exoplanet v0.3.2*, Zenodo, doi:10.5281/zenodo.1998447
- Fukui, A., Narita, N., Tristram, P. J., et al. 2011, *PASJ*, **63**, 287
- Gaia Collaboration, Vallenari, A., Brown, A. G. A., et al. 2023, *A&A*, **674**, A1
- Gao, P., & Zhang, X. 2020, *ApJ*, **890**, 93
- Garcia, L. J., Timmermans, M., Pozuelos, F. J., et al. 2021, *MNRAS*, **509**, 4817
- Gelman, A., Carlin, J. B., Stern, H. S., et al. 2014, *Bayesian Data Analysis* (3rd ed.; Boca Raton, FL: CRC Press)
- Gelman, A., & Rubin, D. B. 1992, *StaSc*, **7**, 457
- Gillon, M., Jehin, E., Magain, P., et al. 2011, *EPJ Web of Conf.*, **11**, 06002
- Gordon, T. A., & Agol, E. 2022, *AJ*, **164**, 111
- Green, G. M., Schlafly, E. F., Finkbeiner, D., et al. 2018, *MNRAS*, **478**, 651
- Greklek-McKeon, M., Knutson, H. A., Vissapragada, S., et al. 2023, *AJ*, **165**, 48
- Hadden, S., & Lithwick, Y. 2014, *ApJ*, **787**, 80
- Hadden, S., & Lithwick, Y. 2017, *AJ*, **154**, 5
- Hamann, A., Montet, B. T., Fabrycky, D. C., Agol, E., & Kruse, E. 2019, *AJ*, **158**, 133
- Han, T., & Brandt, T. D. 2023, *AJ*, **165**, 71
- Hipke, M., David, T. J., Mulders, G. D., & Heller, R. 2019, *AJ*, **158**, 143
- Hoffman, M. D., & Gelman, A. 2014, *JMLR*, **15**, 1593
- Hogg, D. W., & Foreman-Mackey, D. 2018, *ApJS*, **236**, 11
- Holczer, T., Mazeh, T., Nachmani, G., et al. 2016, *ApJS*, **225**, 9
- Horne, K. 1986, *PASP*, **98**, 609
- Huehnerhoff, J., Ketzbeck, W., Bradley, A., et al. 2016, *Proc. SPIE*, **9908**, 99085H
- Ioannidis, P., Huber, K. F., & Schmitt, J. H. M. M. 2016, *A&A*, **585**, A72
- Jehin, E., Gillon, M., Queloz, D., et al. 2011, *Msng*, **145**, 2
- Jensen, E., 2013 *Tapir: A Web Interface for Transit/eclipse Observability*, Astrophysics Source Code Library, ascl:1306.007
- Jones, S. E., Stefansson, G., Masuda, K., et al. 2024, *AJ*, **168**, 93
- Jontof-Hutter, D., Dalba, P. A., & Livingston, J. H. 2022, *AJ*, **164**, 42
- Jontof-Hutter, D., Ford, E. B., Rowe, J. F., et al. 2016, *ApJ*, **820**, 39
- Kipping, D. M. 2010, *MNRAS*, **408**, 1758
- Kipping, D. M. 2013, *MNRAS*, **435**, 2152
- Kokubo, E., & Makino, J. 2004, *PASJ*, **56**, 861
- Kreidberg, L. 2015, *PASP*, **127**, 1161
- Lee, E. J., & Chiang, E. 2016, *ApJ*, **817**, 90
- Libby-Roberts, J. E., Berta-Thompson, Z. K., Désert, J.-M., et al. 2020, *AJ*, **159**, 57
- Lightkurve Collaboration, Cardoso, J. V. d. M., Hedges, C., et al., 2018 *Lightkurve: Kepler and TESS Time Series Analysis in Python*, Astrophysics Source Code Library, ascl:1812.013
- Lindgren, L., Bastian, U., Biermann, M., et al. 2021, *A&A*, **649**, A4
- Lopez, E. D., & Fortney, J. J. 2014, *ApJ*, **792**, 1
- Luger, R., Agol, E., Foreman-Mackey, D., et al. 2019, *AJ*, **157**, 64
- Masuda, K. 2014, *ApJ*, **783**, 53
- Masuda, K. 2022, *ApJ*, **937**, 94
- Masuda, K. 2023, *kemasuda/jaxstar: v0.1.0*, Zenodo, doi:10.5281/zenodo.8272017
- Masuda, K., Winn, J. N., & Kawahara, H. 2020, *AJ*, **159**, 38
- Mazeh, T., Holczer, T., & Shporer, A. 2015, *ApJ*, **800**, 142
- McCully, C., Volgenau, N. H., Harbeck, D.-R., et al. 2018, *Proc. SPIE*, **10707**, 107070K
- McQuillan, A., Mazeh, T., & Aigrain, S. 2014, *ApJS*, **211**, 24
- Millholland, S. 2019, *ApJ*, **886**, 72
- Millholland, S., Wang, S., & Laughlin, G. 2017, *ApJL*, **849**, L33
- Millholland, S. C., He, M. Y., & Zink, J. K. 2022, *AJ*, **164**, 72
- Miralda-Escudé, J. 2002, *ApJ*, **564**, 1019
- Morris, B. 2020, *JOSS*, **5**, 2103
- Narita, N., Fukui, A., Kusakabe, N., et al. 2019, *JATIS*, **5**, 015001
- Narita, N., Fukui, A., Yamamuro, T., et al. 2020, *Proc. SPIE*, **11447**, 29
- Nesvorny, D., Kipping, D. M., Buchhave, L. A., et al. 2012, *Sci*, **336**, 1133
- Nocedal, J., & Wright, S. J. 2006, *Numerical Optimization* (2nd ed.; New York: Springer)
- Ohno, K., & Fortney, J. J. 2022, *ApJ*, **930**, 50
- Ohno, K., & Tanaka, Y. A. 2021, *ApJ*, **920**, 124
- Oshagh, M., Santos, N. C., Boisse, I., et al. 2013, *A&A*, **556**, A19
- Parviainen, H., & Aigrain, S. 2015, *MNRAS*, **453**, 3821
- Paxton, B., Bildsten, L., Dotter, A., et al. 2011, *ApJS*, **192**, 3
- Paxton, B., Cantiello, M., Arras, P., et al. 2013, *ApJS*, **208**, 4
- Paxton, B., Marchant, P., Schwab, J., et al. 2015, *ApJS*, **220**, 15
- Petigura, E. A., Howard, A. W., Marcy, G. W., et al. 2017, *AJ*, **154**, 107
- Petigura, E. A., Rogers, J. G., Isaacson, H., et al. 2022, *AJ*, **163**, 179
- Phan, D., Pradhan, N., & Jankowiak, M. 2019, arXiv:1912.11554
- Piro, A. L., & Vissapragada, S. 2020, *AJ*, **159**, 131
- Pu, B., & Wu, Y. 2015, *ApJ*, **807**, 44
- Rein, H., & Tamayo, D. 2015, *MNRAS*, **452**, 376
- Rustamkulov, Z., Sing, D. K., Liu, R., & Wang, A. 2022, *ApJL*, **928**, L7
- Salvatier, J., Wiecki, T. V., & Fonnesbeck, C. 2016, *PeerJ Comp. Sci.*, **2**, e55
- Schwarz, G. 1978, *AnSta*, **6**, 461
- Shahaf, S., Mazeh, T., Zucker, S., & Fabrycky, D. 2021, *MNRAS*, **505**, 1293
- Skrutskie, M. F., Cutri, R. M., Stiening, R., et al. 2006, *AJ*, **131**, 1163
- Stefansson, G., Mahadevan, S., Hebb, L., et al. 2017, *ApJ*, **848**, 9
- Steffen, J. H., Fabrycky, D. C., Agol, E., et al. 2013, *MNRAS*, **428**, 1077
- Tamayo, D., Cranmer, M., Hadden, S., et al. 2020, *PNAS*, **117**, 18194
- Tayar, J., Claytor, Z. R., Huber, D., & van Saders, J. 2022, *ApJ*, **927**, 31
- Van Eylen, V., & Albrecht, S. 2015, *ApJ*, **808**, 126
- Vissapragada, S., Jontof-Hutter, D., Shporer, A., et al. 2020, *AJ*, **159**, 108
- Walkowicz, L. M., & Basri, G. S. 2013, *MNRAS*, **436**, 1883
- Wang, L., & Dai, F. 2019, *ApJL*, **873**, L1
- Weiss, L. M., Marcy, G. W., Petigura, E. A., et al. 2018, *AJ*, **155**, 48
- Wilson, J. C., Eikenberry, S. S., Henderson, C. P., et al. 2003, *Proc. SPIE*, **4841**, 451
- Winn, J. N. 2011, in *Exoplanets*, ed. S. Seager (Tucson, AZ: Univ. Arizona Press), 55
- Winn, J. N., & Fabrycky, D. C. 2015, *ARA&A*, **53**, 409
- Wisdom, J. 2006, *AJ*, **131**, 2294
- Wisdom, J., & Holman, M. 1991, *AJ*, **102**, 1528
- Zhu, W., Petrovich, C., Wu, Y., Dong, S., & Xie, J. 2018, *ApJ*, **860**, 101
- Zhu, W., & Wu, Y. 2018, *AJ*, **156**, 92